Universiteit
Leiden
The Netherlands

Growth and Transport Properties of [Rare Earth]TiO3/SrTiO3 Interfaces

Lebedev, N.

Citation
Lebedev, N. (2020, December 1). *Growth and Transport Properties of [Rare Earth]TiO3/SrTiO3 Interfaces*. *Casimir PhD Series*. Retrieved from https://hdl.handle.net/1887/138477

Version:	Publisher's Version
License:	Licence agreement concerning inclusion of doctoral thesis in the Institutional Repository of the University of Leiden
Downloaded from:	https://hdl.handle.net/1887/138477

Note: To cite this publication please use the final published version (if applicable).

Cover Page

Universiteit Leiden

The handle http://hdl.handle.net/1887/138477 holds various files of this Leiden University dissertation.

Author: Lebedev, N.
Title: Growth and Transport Properties of [Rare Earth]TiO3/SrTiO3 Interfaces
Issue Date: 2020-12-01

Growth and Transport Properties of [Rare Earth]TiO_3/$SrTiO_3$ Interfaces

Proefschrift

ter verkrijging van
de graad van Doctor aan de Universiteit Leiden,
op gezag van Rector Magnificus prof.mr. C.J.J.M. Stolker,
volgens besluit van het College voor Promoties
te verdedigen op dinsdag 1 december 2020
klokke 10.00 uur

door

Nikita Lebedev
Geboren te Kamensk-Oeralski, Rusland, 1990

Promotor:

Prof. dr. J. Aarts

Promotiecommissie:

Dr. A. Caviglia	Technische Universiteit Delft
Prof. dr. U. Zeitler	Radboud Universiteit Nijmegen
Prof. dr. E. R. Eliel	
Prof. dr. ir. S. J. van der Molen	

Casimir PhD series, Delft-Leiden 2020-28
ISBN 978-90-8593-454-7

An electronic version of this thesis can be found at `https://openaccess.leidenuniv.nl/`.

This work is part of the DESCO research programme of the Foundation for Fundamental Research on Matter (FOM), which is part of the Dutch Research Council (NWO).

About the cover: The cover is an abstract homage to Vasily Vereshchagin's painting, "The Apotheosis of War." The imaginary land, mountains, and sky represent the delta-doped oxide interface. The imaginary trees represent $3d_{xz/yz}$ orbitals, whereas imaginary birds and their nests are $3d_{xy}$ orbitals. The pile consists of graphs, images from this thesis, and colored panels. The shape of the panels is a reference to a triangular quantum well. The De Stijl-like color gamut used is a tribute to Leiden, where most of the work presented in this thesis has been done

Cover design: Nikita Lebedev
Copyright © 2020 Nikita Lebedev

Contents

Introduction **1**

1 Literature Review **5**

1.1 Introduction . . . 6

1.2 Conducting oxide interfaces . . . 6

1.2.1 Formation of the two-dimensional electron liquid at oxide interfaces . . . 6

1.2.2 Superconductivity at oxide interfaces . . . 12

1.2.3 Magnetism in oxide interfaces . . . 13

1.2.4 Kondo-like behavior . . . 14

1.3 The Anomalous Hall Effect in $SrTiO_3$-based heterostructures . . . 16

1.3.1 Mechanisms of the Anomalous Hall Effect and the Ferromagnetic Rashba Model . . . 16

1.3.2 The Anomalous Hall Effect in $SrTiO_3$-based heterostructures . . . 20

1.4 Titanates (RE)TiO_3, where Re=La, Eu and Gd . . . 22

1.4.1 $LaTiO_3$ . . . 22

1.4.2 $GdTiO_3$ . . . 23

1.4.3 $EuTiO_3$ and $Eu_{1-x}La_xTiO_3$ . . . 23

2 Experimental Methods **27**

2.1 Introduction . . . 28

2.2 Sample preparation . . . 28

2.2.1 Termination of $SrTiO_3$ . . . 28

2.2.2 Pulsed Laser Deposition . . . 29

2.2.3 Reflection High-Energy Electron Diffraction . . . 30

2.3 Back gating experiments in the PPMS . . . 32

2.3.1 Insert . . . 32

2.3.2 Van der Pauw measurements . . . 35

2.4 Additional experimental techniques . . . 37

3 Gate-tuned AHE in Intermixed $LaAlO_3/GdTiO_3/SrTiO_3$ 39
3.1 Introduction . . . 40
3.2 Experimental Details . . . 41
3.3 Results . . . 42
3.3.1 TEM characterisation . . . 42
3.3.2 Basic transport properties . . . 44
3.3.3 Effects of gating . . . 46
3.3.4 The question of ferromagnetism . . . 48
3.3.5 Extracting the Anomalous Hall Effect . . . 50
3.4 Discussion . . . 55
3.5 Conclusion . . . 56
3.6 Appendix . . . 58

4 Superconductivity and Magnetoresistance in a-$LaTiO_3/SrTiO_3$ 63
4.1 Introduction . . . 64
4.2 Experimental details . . . 65
4.3 Normal state magnetotransport . . . 66
4.3.1 The origin of conductance . . . 66
4.3.2 Magnetotransport without back gate . . . 68
4.3.3 The effect of gating on the sheet resistance . . . 70
4.3.4 The effect of gating on the magnetotransport . . . 71
4.4 Electronic transport in the superconducting state . . . 73
4.5 Discussion . . . 77
4.6 Conclusions . . . 79
4.7 Appendix . . . 81
4.7.1 Analysis of carrier concentrations and mobilities . . . 81
4.7.2 Magnetotransport properties . . . 81
4.7.3 Superconducting properties . . . 83
4.7.4 Circuit analysis . . . 85

5 On the SIT in disordered oxide interfaces 89
5.1 Introduction . . . 90
5.2 Study of a-LTO/STO . . . 92
5.2.1 Results . . . 92
5.2.2 Discussion . . . 95

5.3 Study of LGAO/GLATO/STO 97
5.3.1 Results 97
5.3.2 Discussion 102
5.4 Summary 104

6 On a possible Kondo effect in $LaAlO_3/Eu_{1-x}La_xTiO_3/SrTiO_3$ 107
6.1 Introduction 108
6.2 Experimental details 109
6.3 Results 112
6.3.1 Metal Insulator Transition and transport properties 112
6.3.2 Magnetotransport properties at zero gate voltage 112
6.3.3 Gate tuning of the Anomalous Hall Effect 116
6.3.4 The Kondo regime in resistance 120
6.4 Discussion 122
6.5 Conclusion 124
6.6 Appendix 126

Bibliography 133

Summary 159

Samenvatting 165

List of Publications 171

Curriculum Vitae 173

Acknowledgements 175

Introduction

The advent of electronics has transformed our society significantly. The principle of electronics is based on the ability to actively control the flow of electrons, which carry charge. The field received a great boost in its development from the study of semiconductor materials, which led to the invention of the transistor, a crucial device for control of the charge flow. There are two main classes of transistors, the bipolar transistor and the field effect transistor. The first is a series of semiconductors with different amount of charge carriers, where the voltage applied to a middle section controls the current through the device. The last type utilizes a semiconducting channel through which the current flows, which can be controlled capacitively by applied a voltage underneath the channel, the so-called gate voltage. In this thesis on the transport properties of a conducting channel at the interface between two oxide insulators, gating will play a prime role.

In the ongoing trend of the further miniaturization of electronic components, one bottleneck has started to occur, which is the dissipation of heat in the device, caused by the current flow. At the same time, as fundamental understanding of magnetic materials had deepened, it has become clear that not only the charge, but also the spin and the angular moment of the electron can be used. By controlling the amount of spin flow, electronic-like devices can be created. This new field is named spintronics similarly to electronics. The easiest materials to use for spintronics are metals with different magnetic states, controlled by magnetic fields. However, spin effects can also be found in semiconductor materials with broken inversion symmetry, because of the presence of (noticeable) spin-orbit coupling. Using semiconductors to create a two-dimensional electron gas is promising for the creation of operational devices because an applied gate voltage can now be used to vary the spin-orbit coupling and thereby the spin and charge currents between two ferromagnetic electrodes. Such a device, first proposed by Datta and Das, is called a spin transistor [1]. A spin-polarized charge current would be injected into the channel through one of the contacts, and applying an electric field via the gate voltage would induce spin precession. The amount of precession over the length of the channel controls how effective the electron can exit through the

magnetic drain contact, leading to a variation in resistance. A low (high) resistance can be considered as an on (off) state.

To actually fabricate such a device is a challenging task which, for best results, requires the combination of a two-dimensional electron gas (a 2DEG; needed for high on/off ratio's) with ferromagnetic electrodes. Here transition metal oxides come into play. In 2004, Ohtomo and Hwang [2] discovered that a 2DEG can form at the interface interface between two insulating transition oxides, in their case between $SrTiO_3$ and $LaAlO_3$. Subsequently, superconductivity [3, 4] tunable spin-orbit coupling [5], and signatures of magnetism and even coexistence of superconductivity and magnetism [6–8] were been reported. Since then, many more of the subtleties of the band structure of the 2DEG and the effects of gating fields have been unraveled. Still, in particular the occurrence of magnetism is not yet well controlled or even understood. Using combinations of oxide insulators as a platform to realize prototypes for spintronics devices still requires more research.

The aim of this thesis is to investigate the possibilities to induce spin-polarization into oxide 2DEGs and their control by electric fields. The original $LaAlO_3/SrTiO_3$ interface contains one atom which can carry magnetism, the Ti atom. In $SrTiO_3$ it occurs in the form of TiO_2 sheets, has a valency 4+ and does not carry a magnetic moment. When oxide vacancies are introduced it can become Ti^{3+} and carry a moment based on one d electron. It is generally assumed that oxide vacancies are at the basis of the magnetism which has been reported at $LaAlO_3$/ $SrTiO_3$ interfaces. There are no magnetic moments on the $LaAlO_3$ side of the interface, and the question which led this research is what the influence on the 2DEG would be when introducing magnetism through that side. In the ABO_3 structure of $LaAlO_3$, this can be done by substituting Ti for Al, but also by substituting the non-magnetic rare earth element Lanthanum by magnetic ones such as Eu or Gd. This is not trivial, since structural issues, valency issues, but also the issue of ferromagnetism versus antiferromagnetism all come into play. The effect of 'δ-doping', meaning the insertion of one or two atomic layers of a different oxide, was also investigated.

For the research, a number of heterostructures was prepared, namely $LaAlO_3/SrTiO_3$, $LaTiO_3/SrTiO_3$, $LaAlO_3/GdTiO_3/SrTiO_3$, $LaAlO_3/EuTiO_3/SrTiO_3$ and $LaAlO_3/Eu_{1-x}La_xTiO_3/SrTiO_3$. They were all prepared using Pulsed Laser Deposition (PLD) at the University of Twente. Transport measurements, especially back gate experiments, were the main tool to investigate the possibly tunable properties of these systems. Special focus with respect to magnetotransport properties was on the behavior of the Anomalous Hall effect, which is often used as a signature for the occurrence of ferromagnetism in the conduction electron system. Chapter 1 introduces the parent system $LaAlO_3/SrTiO_3$ (or LAO / STO) and the

most relevant experimental and theoretical results obtained thus far, the theory of the Anomalous Hall Effect and a review of (RE)TiO_3 (Re=La, Gd, Eu, $Eu_{1-x}La_x$) and called LTO, GTO, ETO and ELTO). Experimental techniques and protocols are described in Chapter 2. Chapter 3 describes the tunable Anomalous Hall Effect in strongly intermixed LAO/GTO/STO and point out a possible link between the enhancement of the Spin-Orbit Interaction and the appearance of the Anomalous Hall Effect. Chapter 4 focuses on signatures of non-uniformities in normal and superconducting state at interface between STO and amorphous LTO (a-LTO) studied by the magnetotransport measurements. Chapter 5 studies the Superconductor-Insulator transition and the magnetoresistance hysteresis in strongly intermixed LAO/GTO/STO and a-LTO/STO. The observed hysteresis is argued to be rather a signature of inhomogeneous superconducting state than a signature of the coexistence of superconductivity and magnetism. Chapter 6 is dedicated to LAO/STO δ-doped with ELTO. Special attention is paid to the AHE mechanism and the Kondo-like regime which is observed. Unlike what is inferred from most of literature, we argue that the Kondo-like regime which arises in back-voltage experiments at low carrier concentration, arises from the properties of $SrTiO_3$, and are not due to magnetic coupling.

1

Literature Review

1

1.1. Introduction

The two-dimensional electron gas, or rather liquid (2DEL), at oxide interfaces and based on $SrTiO_3$ (STO) has a rich phenomenology. A review of all the phenomena in this system is beyond the scope of the present work. This chapter is constrained to the most relevant results for this thesis. Moreover, the careful reader will notice that some parts of this chapter duplicate information presented in other chapters. That has been done intentionally to keep each chapter self-contained. This chapter will start with a description of the STO band structure, the formation of the 2DEL at the oxide interfaces, the role of Spin-Orbit Coupling (SOC), the occurrence of multiband transport at the interface, and the effects of a back gate voltage. Also superconductivity and magnetism occurring in the 2DEL at oxide interfaces will be introduced. Special attention will be given to the Anomalous Hall Effect (AHE) and its observation at oxide interfaces. The end of the chapter will be an overview of bulk and thin film properties of (RE)TiO_3 (Re=La, Gd, Eu, $Eu_{1-x}La_x$), which are the building blocks for the interfaces to come.

1.2. Conducting oxide interfaces

1.2.1. Formation of the two-dimensional electron liquid at oxide interfaces

In a simple picture semiconductors or insulators have one important quality which make them different from metals, namely the presence of a band gap [9]. In direct- and indirect-gap semiconductors, the Fermi level lies above a filled valence band, but below an empty conduction band, and it requires (thermal) excitations of the charge carriers to invoke conduction. However, semiconductors can be doped by atoms with different valence, thereby changing the position of the Fermi level and leading to conductivity. These atoms can be evenly distributed over whole crystal or they can be incorporated in a certain atomically thin sheet. That is called a δ-doping. Unintentional doping can also occur due to vacancies in crystal structures [9]. By combining semiconducting materials with different band gaps, so-called quantum wells (QWs) can be created. Consider the spatial variation of the conduction band edge when a very thin layer of GaAs with a smaller band gap is sandwiched between layers of AlGaAs with a larger band gap, as shown in Fig. 1.1a. Because of the confinement, electron levels are formed which are quantized in the stacking direction (the z-direction), but free in the plane directions. This is why

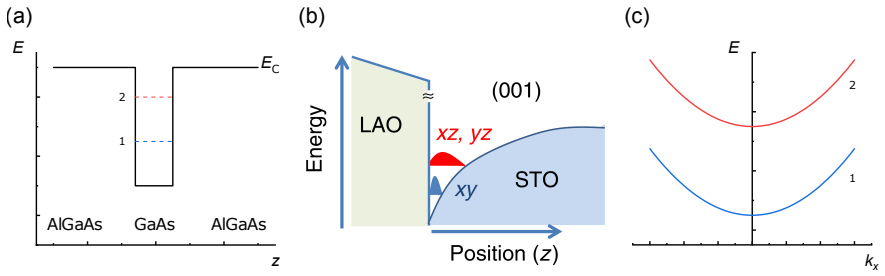

Figure 1.1: (a) The conduction band edge variation of AlGaAs/GaAs/AlGaAs heterostructure forming a quantum well. (b) Quantum well formation at a single (oxide) interface. The figure is adopted from Ref. [12]. Copyright 2015 by Springer Nature. (c) The lowest two parabolic bands in a quantum well heterostructure.

the electron system is two-dimensional. Similar confinement can be created at a single interface, using different degrees of doping and the ensuing phenomenon of band bending. A schematic example is given in Fig. 1.1b. The QW shape is triangular rather than rectangular, but the principle is the same. This is the situation encountered in $LaAlO_3/SrTiO_3$ (LAO/STO). The in-plane energy dispersion of the quantized levels can be described by a set of parabolic bands (Fig. 1.1c) where the first two levels are shown. If the material consists of heavy atoms with a large nuclear charge, there may be non-negligible spin-orbit coupling (SOC), which lifts spin degeneracy of the bands. Moreover, a quantum well heterostructure lacks spatial inversion symmetry and an additional contribution to the SOC arises, which is called the Rashba effect [10, 11]. One point of interest, in particular for the single-heterojunction QW, is that band occupancy and carrier concentration can be tuned by applying an electric field through a metal contact on one of the semiconductors (the gate). This electrode and the 2DEG can then be seen as a parallel plate capacitor, so the carrier concentration can be changed by applying a gate voltage.

Now we turn to the interface between transition oxide insulators, where QWs and a 2DEL form as well. The most studied oxide interface is between the non-magnetic band insulators LAO and STO [2]. LAO has a band gap of about 5.6 eV [13], whereas STO has a band gap around 3.2 eV [14, 15]. Both are perovskites of type ABO_3 and have a pseudocubic crystal structure. LAO shows a small rhombohedral distortion, STO is cubic at room temperature and undergoes a structural transition to tetragonal below 105 K [16, 17]. LAO is a polar material. It consists of a stacking of LaO and AlO_2 layers, which means a stacking of sheets with -1 and +1 electron charges. STO is non-polar and consists of a stacking of SrO and TiO_2, which means a stacking of charge-neutral layers. A charge discontinuity therefore

occurs at the interface, which is often referred to as the polar catastrophe, From simple electrostatics, the discontinuity can be avoided by the transfer of half an electron charge ($e/2$) per unit cell (u.c.) from the LAO surface to the LAO/STO interface. The first proposed explanation for the formation of the 2DEL was based on such simple charge transfer [18, 19]. Supporting this model is the fact that a minimum critical thickness for the LAO layer grown on top of an STO substrate of 4 u.c. is needed before the 2DEL is formed [20]. However, various experiments were at odds with this explanation, and other scenario's were proposed. One is the development of a critical density of oxygen vacancies at the surface of the LAO layer, which leads to a charge transfer of $2e$ per vacancy to the interface [19, 21]. Also, La/Sr intermixing [22] and oxygen vacancies formed in the STO [23, 24] can introduce conductivity at the STO surface, and the last mechanism appears especially important in 2DELs formed at the interface between and STO and amorphous oxides [25, 26]. One important remark should be made here. Almost invariably, a single crystal substrate is used for the STO side of the interface, and only films grown on the TiO_2-terminated surface of STO exhibit an (n-type) conductivity [2, 18]. An interface created by the growth of LAO on a SrO-terminated surface was expected to be a p-type but turned out to be insulating [18]. This has lent more credence to the indications that oxygen vacancies in the top TiO_2 surface, probably even formed during the growth of LAO, are important for the 2DEL formation.

Following up on the bandstructure of the 2DEL, the n-type doping will induce electrons in $3d$ orbitals of the Ti at the interface. In free atom, the Ti orbitals are ten-fold degenerate, but in the bulk STO the six nearest oxygen atoms produce a cubic crystal field, which leads to a t_{2g} triplet (d_{xy}, d_{yz}, d_{xz}) and e_g doublet (d_{z^2}, $d_{x^2-y^2}$) [15, 29]. Since the t_{2g} triplet lies 2 eV lower than the e_g doublet, it forms the conduction band minimum [29–31], and further consideration is limited to these states. The corresponding bulk band structure is shown in the Fig. 1.2a. The SOC in the STO leads to the splitting of the triplet state, which is six times degenerate, into four times and two times degenerate levels with a splitting around ≈ 29 meV as determined from theoretical calculations [27, 28, 32](Fig. 1.2b). Below 105 K STO undergoes a cubic to tetragonal transition [16, 17], which further splits the triplet into two states with splitting $\approx 2-3$ meV and breaks the symmetry along k_x and k_z [15, 27, 33, 34](Fig. 1.2c). However, it is hard to experimentally determine a value of the splitting due to the SOC in the tetragonal phase [30]. At the LAO/STO (001) interface inversion symmetry is broken. This shifts the in-plane d_{xy} orbitals below the out-of-plane $d_{xz/yz}$ ones, corresponding with a splitting between them of 50 meV as determined by X-Ray Linear Dichroism Measurements (XMCD) [33]. The SOC hybridizes the orbitals [28, 34]. The above picture of the interface states essentially represents two bands, one of them with a light effective mass in the in-plane direction and a heavy mass in the out-of-plane direction,

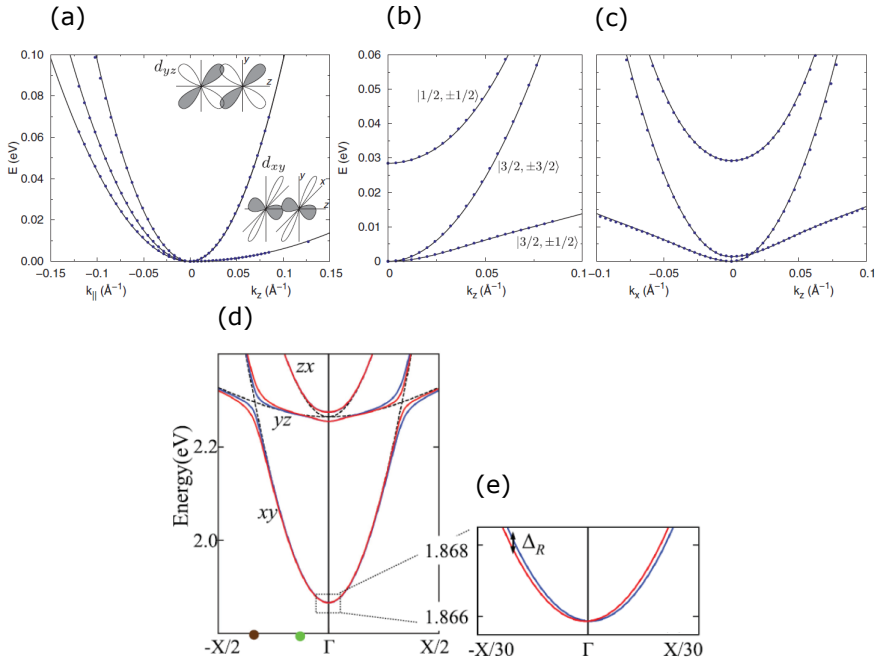

Figure 1.2: The DFT calculation of the STO band structures in (a) cubic crystal lattice without the SOC, (b) cubic crystal lattice with the SOC (the bands are shifted in such way that the bottom correspond to the zero energy) and (c) tetragonal crystal structure with the SOC. The figures a, b, c are reprinted from Ref. [27]. Copyright 2013 by the American Physical Society. (d) The tight binding calculations of the band structure of the LAO/STO interface and (e) zoom at the bottom of the d_{xy} band. The blue and red colors correspond to different spins. The figures d and e are reprinted from Ref. [28]. Copyright 2013 by the American Physical Society.

whereas the second band has a heavier effective mass in-plane than out-of-plane. The different band curvature together with the spitting leads to the formation of avoided band crossing [27, 32] as can be seen on the Fig. 1.2d. Furthermore, the consequence of broken inversion symmetry is Rashba-like spin splitting [5, 32], which produces two characteristic features, namely small spin splitting at the bottom d_{xy} band (Fig. 1.2e) and stronger splitting near the avoided band crossing between the d_{xy} and $d_{xz/yz}$ bands [27, 28, 32, 35] (Fig. 1.2d). Clearly, the Ti-3d-derived band structure of the quantum well states is far from trivial, and leads to many intriguing phenomena. Several will be discussed later, but an important one is that the system can be switched from one-band (the d_{xy} band) to two-band behavior (filling the $d_{xz/yz}$ band) by moving the Fermi energy through the anticrossing point with a gate voltage. Since this also entails a change in Fermi surface topology, this

point (in voltage) is called a Lifshitz point [32, 35, 36]. Crossing the Lifshitz point leads to sometimes subtle changes in transport properties, which requires careful analysis. The most clear transport signature of such a transition is the change from a linear to a non-linear Hall effect [36, 37].

The main signatures of the absence or presence of SOC in magnetotransport experiments, specifically in magnetoresistance (*MR*), are weak localization (WL) and weak antilocalization (WAL). Both phenomena have been extensively studied in semiconducting materials and require special attention since, as mentioned in the introduction, controlling the amount of spin orbit coupling can be useful in devices. WL occurs in a disordered metallic system, both with no or little SOC and gives a negative correction to the conductivity due to quantum interference, which enhances the probability for backscattering [38–40]. WAL arises when the SOC is present, because spin relaxation becomes important in the interference effects. Strong SOC adds an additional phase to the interference, leading to a positive instead of a negative correction [39, 41–43]. Both WL and WAL have been observed experimentally in LAO/STO [5, 44, 45]. Due to the fact that the Rashba coupling constant can be tuned directly by changing electric field by applying the gate voltage [5, 46], or by changing the carrier concentration [46], the *MR* can also show a transition from WAL to WL [4, 5]. Early studies of the gate dependence of the Rashba coupling provided contradicting results. Ref. [5, 12] reported an increase of the Rashba coupling constant with increasing of the gate voltage, but Ref. [47] observed the opposite trend. Later reports found that the Rashba coupling peaks near the Lifshitz point [46, 48], which seems to be in agreement with spin-to-charge conversion experiments [49]. An unresolved subtlety with respect to the effects of SOC is the question of its k-dependence. In bulk materials with inversion symmetry, the k-dependence is linear. Without inversion symmetry, a cubic k-dependence becomes possible, and was reported by in Refs. [48, 50], whereas Ref. [46] argued that the dominant SOC contribution is k-linear.

Next we come to the effects of applying a gate voltage in oxide heterostructures. Because both STO and LAO are insulating, they can be used as a barrier for applying a gate voltage. This allows utilizing various geometries of gate electrodes. In the present work, a back gate geometry has been used, where the STO substrate has been used as the dielectric layer. In spite of the large thickness of STO substrate, this geometry is relatively effective due to large permittivity of STO at low temperatures. The back gate voltage controls not only the carrier concentration, but also the width of the (triangular) quantum well, and therefore strongly affects the amount of disorder sampled [51]. Generally, a decrease of the back gate voltage leads to narrower potential well and lower mobility [52, 53]. One of the most prominent effects of applying a back gate voltage to STO-based heterostructures

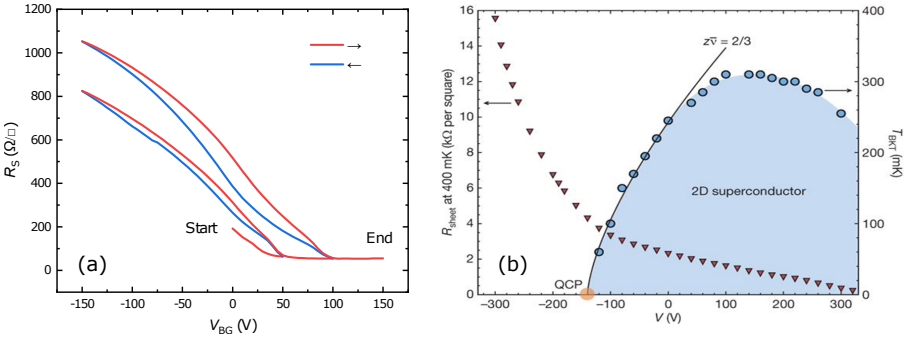

Figure 1.3: (a) The dependence of the sheet resistance R_S on the backgate voltage for a LAO/STO sample. The voltage was swept in the following sequence: from 0 to 50 V, from 50 V to −150 V, from −150 to 100 V, from 100 V to −150 V, from −150 V to 150 V. (b) The dependence of R_S and of the critical temperature T_c on the gate voltage for a LAO/STO sample at 400 mK. The figure is adopted from Ref. [4]. Copyright 2008 by Springer Nature

is hysteresis due to charge trapping [52, 54, 55]. This effect is observed when, at the first time after cooldown, a significant positive voltage is applied to the heterostructures, i.e. a voltage that has not been reached in previous voltage sweeps during that particular cooldown. As an example, Fig. 1.3a shows the dependence of the sheet resistance on the applied back gate voltage for a LAO/STO sample measured at 3 K and prepared for this thesis. The first detailed study of this phenomenon was performed by Biscaras *et al.* [54]. They proposed that at the initial cooldown, the Fermi level lies close to the top of the quantum well, and after filling to a certain threshold, electrons are able to escape irreversibly into the STO substrate, where they are trapped in defects. Recently, Ref. [55] put forward an alternative explanation based on the formation of in-gap trapping states due to clustering of oxygen vacancies. For more details on experimental aspects of back gate experiments see Section 2.3. The strong effect of charge trapping and variation of the disorder together with carrier concentration [52, 53] led to a significant effort to develop top-gating experiments. These experiments utilize the LAO layer as a dielectric insulator and allow to control charge filling with the top gate but do not change the shape of the potential well [37, 53, 56]. The combination of top-and back-gate configurations allows independently, but still simultaneously, to control carrier concentration and disorder [51, 53]. The top gate experiments will not be discussed further.

1.2.2. Superconductivity at oxide interfaces

Gating changes the carrier concentration in the QW, the amount of bands involved, and the strength of SOC, which has consequences for magnetotransport. What has not yet been mentioned is that also cooperative electron phenomena occur at oxide interfaces, in particular superconductivity and magnetism of some kind, plus related effects such as the Kondo effect or the possible coexistence of superconductivity and magnetism. Gate-tunability provides additional control over these phenomena as well. In order to discuss the experiments on superconductivity at the LTO/STO and LAO/GTO/STO interfaces, we first introduce the basic framework of the occurrence of superconductivity at STO-based interfaces.

Being a 2DEL, the LAO/STO interface exhibits a superconducting transition of the so-called Berezinskii-Kosterlitz-Thouless (BKT) type [3, 57]. The BKT transition is a thermodynamic instability in which spontaneoulsy formed vortex-antivortex pairs, bound at low temperatures, dissociate into free vortices at a characteristic temperature, T_{BKT}, which lies below the bulk T_c, and basically only depends on the sheet resistance of the thin fim or 2D metal. The superconducting state is tunable by the gate voltage [4, 52] and has a dome-like critical temperature dependence on the applied voltage (Fig. 1.3b). At the moment, there is no full agreement on the role of the band structure, and in particular the one-band to two-band transition, with respect to the superconducting transition. Ref. [36] reported that the maximum of the dome corresponds to the Lifshitz point, but Refs. [58, 59] argued that superconductivity is triggered by the onset of the occupation of the second band. Ref. [51] found that the dome maximum is correlated with the occupation of the second $3d_{xy}$ subband.

The superconducting state in STO-based structures often exhibits signatures of inhomogeneities such as hysteretic IV curves [60, 61] and multiple steps in the temperature dependence of the resistance close to the transition region [51, 61, 62]. Broadening of the superconducting transition has also been attributed to inhomogeneities [62–64]. Such inhomogeneities can arise due to some phase separation between electron-dense and less dense domains [63, 65]. Another important source of inhomogeneities in STO-based interfaces are the tetragonal domains which appear below the cubic to tetragonal structural transition at 105 K [66–69]. These domains are stable with changing temperature, as long as the sample is not cycled above that temperature [66, 69]. On the other hand, they can be tuned by the back gate voltage [66, 68, 69], and it has also been shown that this domain structure strongly modulates conduction paths [66], and even that the different domains have different transition temperatures [67].

Besides the gate dependence of the critical temperature, Caviglia *et al.* [4] have observed a Superconductor-to-Insulator (SIT) transition near a sheet resistance value of 6.5 kOhm. The physics of this transition is still under debate. There is the 'dirty boson' scenario, which means that the strong disorder causes an electronic phase separation, with isolated superconducting islands in a sea of insulating material even up to localized Cooper pairs [70–72]. There is also a Fermionic scenario, in which Cooper pairs are destroyed by various mechanisms in the insulating phase [71]. A scaling analysis of the behavior of the magnetic field dependence of the sheet resistance around the SI transition in LTO/STO revealed non-universal behavior as function of the gate voltage. A critical exponent product $\nu z = 2/3$ was found in one regime, favoring the Fermionic scenario, but $\nu z = 3/2$ in another, stipulating the dirty boson scenario. At the same time, a similar study on LAO/STO found $\nu z = 7/3$ corresponding to the bosonic scenario [73]. For such critical exponents the insulating phase is in a quantum percolation state, in which Cooper pairs tunnel between localized superconducting islands [72, 73]. Also the complex behavior of *MR* hysteresis across the SIT was interpreted as evidence of such a scenario [74].

1.2.3. Magnetism in oxide interfaces

In spite of the intense investigation of the LAO/STO conducting interface over last 15 years, there is no consensus on the low-temperature magnetic state of the system [19, 75]. Polarized neutron refractometry showed a small number of magnetic moments localized at the interface in multilayer samples [76]. Magnetic torque measurements revealed superparamagnetic behavior of the magnetization in LAO/STO, but were not able to detect a change in low field dependence of the magnetic moment up to 40 K [7] as would have been expected. Scanning SQUID microscopy detected the presence of ferromagnetic patches [6]. Ariando *et al.* [65] have observed diamagnetic, paramagnetic and ferromagnetic contributions in LAO/STO in SQUID magnetometry experiments, which varied with the growth pressure, with both the diamagnetic one and the ferromagnetic one increasing in samples grown at higher pressure. Coey *et al.* [77] investigated a number of STO crystals from different suppliers and found multiple contributions to magnetism: an extrinsic signal related to ferromagnetic impurities from the preparation process and an intrinsic isotropic magnetic signal from the surface. That signal, with saturation behavior and almost absent hysteresis, was observed in a wide range of temperatures. Different possible scenarios have been discussed, but no model was able to provide a full and satisfactory explanation. Moreover, recent scanning SQUID experiments revealed striped magnetic modulation coupled

to the ferroelastic domains in STO based heterostructures [78]. The modulation disappears below 8 K, which was attributed to the establishing of magnetically ordered state.

A number of experiments also indicate coexistence of superconductivity and magnetism in STO-based heterostructures. The magnetic patches detected by the scanning SQUID microscopy [6] and the magnetic order observed by the magnetic torque [7] were found to be present below the superconducting transition. Furthermore, hysteretic *MR* was reported in superconducting LAO/STO [8, 74, 79, 80] and attributed to a signature of coexistence of superconductivity and magnetism. On the other hand, some experiments showed presence of hysteretic *MR* in the milliKelvin range due to magnetocaloric effect [81, 82]. Generally, the picture is one of poor reproducibility [83].

A few theories of magnetism at the LAO/STO interface have been proposed. They can be separated in intrinsic and extrinsic effects [83]. Among the intrinsic mechanisms are localized carriers [84, 85], itinerant ferromagnetism [86, 87] or ferromagnetism arisen from localized electrons and mediated by conduction electrons [88–90]. On the other side, extrinsic mechanisms have been proposed such as Sr vacancies [91], Al vacancies [92], oxygen vacancies [93, 94] and magnetic contamination [77, 83]. On the whole, a systematic study [83] of the LAO/STO interface by various techniques concluded that intrinsic mechanisms for magnetism are unlikely to be the origin of the magnetic effects in LAO/STO.

1.2.4. Kondo-like behavior

One of the first results on LAO/STO signaling the possible presence of magnetic effects in transport was the work by Brinkman *et al.* [95]. Apart from the *MR* hysteresis they found at low temperatures in a particular range of oxygen-growth pressures, in the same range they observed a resistance upturn at low temperatures with saturation at the lowest temperature. They proposed that that can arise due to the Kondo effect, a behavior in agreement with an oxygen vacancy picture of the origin of the magnetism. This Kondo effect is expected to arise due to localized magnetic moments. Ref. [90, 96] argued that the magnetic moments are a small amount of localized Ti $3d_{xy}$ electrons, which can be regarded as impurities. The d_{xy} bands lie in the plane of interface, and mobile $3d_{xy}$ electrons couple antiferromagnetically to magnetic moments. In contrast, the $d_{xz/yz}$ band is perpendicular to the interface plane, and $3d_{xz/yz}$ electrons couple ferromagnetically with the magnetic moments. Therefore, tuning the system through the Lifshitz point should also change a Kondo-like state to a ferromagnetic state. According to the

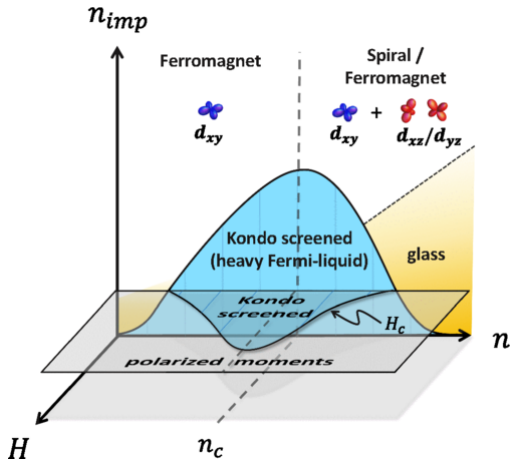

Figure 1.4: (a) The phase diagram for magnetism at the LAO/STO interface proposed by Ruhman *et al.* n is the electron density, n_{imp} is the density of local magnetic moment, H is the in-plane magnetic field, and n_c is the critical density above which the second band is filled. The figure is reprinted from Ref. [90]. Copyright 2014 by American Physical Society.

theory proposed by Ruhman *et al.*, the indirect RKKY exchange interaction will be competing with Kondo screening, and therefore, the dominant behavior would depend not only on the carrier concentration n but also on the concentration of 'impurity' magnetic moments n_{imp}. From this theory, a magnetic phase diagram for these two values will have a dome-like shape with a maximum at the Lifshitz point, as shown in Fig. 1.4. Kondo screening will disappear at very low electron densities deep inside an insulating phase and at very high electron densities deep inside of the two-band regime [90]. Such a model might explain specific features in magnetotransport data, in particular a drop of in-plane magnetoresistance. Below a certain critical in-plane field, the magnetic moments are Kondo-screened, and the unitary scattering leads to high resistance. Above that field, the Kondo singlet breaks up, the moments become polarized, and the resistance decreases [90, 96, 97]. The critical field will also have a-dome like density dependence according to [90] with a maximum around Lifshitz point (see Fig. 1.4).

However, Diez *et al.* [98] found that behavior of the negative in-plane *MR* persists up to 20 K, which does not fit in the framework of the (temperature dependent) Kondo picture. Instead, they described it within single-particle Boltzmann transport theory, showing that the large negative *MR* can be produced by the SOC, the anisotropy of the Fermi surface above the Lifshitz transition and finite-range electrostatic impurity scattering. Moreover, Ref. [99] studied the effect of hydrostatic pressure on the resistance minimum and concluded that it arises from

impurity scattering. The impurities were speculated to be oxygen vacancies. A strong pressure and temperature dependence of the STO dielectric constant combined with thermoactivated charge trapping would lead to the resistance [99] minimum. We will address this point extensively in Chapter 6 on LAO/STO doped with $Eu_{1-x}La_xTiO_3$.

1.3. The Anomalous Hall Effect in $SrTiO_3$-based heterostructures

An often used signature of (ferro)magnetism in STO-based interfaces is the Anomalous Hall Effect (AHE). The AHE is a quite complicated and still not fully understood effect, and before reviewing earlier studies of the AHE in the STO-based heterostructures, a general introduction will be given. For a detailed review see Ref. [100].

1.3.1. Mechanisms of the Anomalous Hall Effect and the Ferromagnetic Rashba Model

The AHE is a long-known phenomenon. In ferromagnetic metals there is, besides the ordinary Hall effect, which is due to the Lorentz force and proportional to the applied perpendicular magnetic field, an additional contribution to the Hall voltage, which is proportional to the magnetization [100]. Pugh and Lippert [101, 102] introduced an empirical formula:

$$\rho_{xy} = \rho_{xy}^{OHE} + \rho_{xy}^{AHE} = R_0 H_z + R_S M_z \tag{1.1}$$

R_0 depends on the carrier concentration (in case of one band transport), whereas R_S depends on many parameters of the system, and especially on the longitudinal resistance.

Historically, three main mechanisms have been proposed: skew scattering [103, 104], side jump [105] and an 'intrinsic contribution' or 'anomalous velocity' contribution, suggested very early on by Karplus and Luttinger [106]. In an electric field, electrons acquire an additional amount of group velocity (the anomalous velocity), which is perpendicular to the applied electric field. In non-magnetic materials the sum of the anomalous velocity over all occupied band states is zero, but at certain conditions that is not true for ferromagnets and the AHE appears. It is intrinsic, for clean metals, and nowadays it would be called a Berry phase effect. A different

picture, involving impurities rather than the clean band structure, was proposed by Smit. He proposed that origin of the AHE is an asymmetric scattering from impurities due to the SOI. This scattering is called skew scattering [103, 104]. Berger, finally, proposed a mechanism called side jump: when an electron travels in a solid in the presence of spin-orbit coupled impurities, it will experience electric fields, which will be opposite for approaching and leaving the impurity. The electric fields will produce an electron velocity deflection in opposite directions. Time integration of the velocity deflection then will be the side jump distance.

In modern literature, linear transport theories gained in popularity to study the AHE , because they allow the treatment of the AHE within the same model. These theories are semiclassical Boltzmann transport theory [107, 108] and microscopic theories based on the Kubo formalism [107, 109] and the Keldysh formalism [110, 111]. They produce similar predictions [100, 107, 108]. In such theories, the classification of contributions to the AHE is based on the dependence of the conductance on the Bloch-state transport lifetime τ [100]. In this classification, the skew-scattering term is defined as a term proportional to τ. The underlying reason for the dependence on τ is the fact that the principle of detailed balance in the semiclassical Boltzmann transport has to be abandoned. The principle states the equality between two transition probabilities $W_{n\to m}$ from the state n to m and the opposite one $W_{m\to n}$ [100]. However, this is not correct in the presence of SOC, because the transition probabilities will be different for right- and left-handed transitions with respect to the magnetization direction [100]. To evaluate this through the Boltzmann equation requires solving it using a collision term with properly defined transition probabilities. The presence of asymmetric scattering rates in the collision term leads to two contributions to the AHE. One of them is proportional to τ, and is the skew scattering contribution. The second term is independent of τ, and sometimes called intrinsic skew scattering [108]. This rather confusing term indicates that, like the skew-scattering term, it originates from the collision term, which would correspond to the historical definition of the skew scattering [100, 103]. Still, unlike the skew scattering in the definition through the Bloch-state transport lifetime it is independent of τ. This term was discarded in early semiclassical studies, although being of the same order of magnitude as a side jump [100].

As two contributions to the AHE are defined through the new classification, other contributions are also needed to be redefined. The intrinsic contribution σ_{xy}^{int} can be defined as the dc limit of the interband Hall conductivity. As we mentioned, it depends on the band structure and arises in ferromagnets when the SOI is present. This mechanism is directly related to an electron Berry's phase curvature [112–114] and proportional to the integral of the Berry curvature of each occupied state over the Fermi sea [100]. The side jump contribution emerges from the

displacement of a Gaussian wave packet with an incident wave vector **k**, when that wave packet is scattered from a spherical impurity in the presence of SOI. The displacement is transverse to **k**.

The intrinsic contribution and the side jump contribution are independent of τ. Together with the intrinsic skew scattering, three terms independent of τ are already introduced. However, the effects due to coordinate shifts during scattering events [107, 108, 115] give rise to one more contribution independent of τ. To understand this contribution, let us consider a quasiparticle experiencing scattering from a side jump in the presence of external electric field. Its potential energy will change, but because the total energy is conserved, it will acquire additional kinetic energy [115]. As a result, there is an additional correction to the momentum distribution function because the equilibrium distribution is not stable anymore and has to be compensated by an additional term [115]. That term is named the anomalous distribution and led to the contribution to the AHE called 'the contribution due to the anomalous distribution' [107, 108, 115]. However, for the sake of simplicity, the side jump is often defined as $\sigma_{xy}^{sj} \equiv \sigma_{xy}^{AHE} - \sigma_{xy}^{skew} - \sigma_{xy}^{int}$. In this definition, other contributions, such as the intrinsic skew scattering and the contribution from the anomalous distribution are included in the side jump term despite their different physical origin [100]. In the microscopic theories all these contributions are usually called ladder-diagram vertex corrections to the conductivity.

One of the main advantages of defining the contributions through τ is the possibility to use a scaling law for the AHE analysis. From an experimental point of view, it means that the analysis of the interdependence of σ_{xy}^{AHE} and σ_{xx} can be used to separate the various contributions because $\sigma_{xx} \sim \tau$. Usually, the longitudinal resistance ρ_{xx} and the Hall resistance due to the AHE ρ_{xy}^{AHE} are used for this, connected through the conductivity tensor, which yields the relation $\rho_{xy}^{AHE} \approx \sigma_{xy}/\sigma_{xx}^2 \approx \sigma_{xy}\rho_{xx}^2$ [100]. For various mechanisms, $\rho_{xy}^{AHE} \sim \rho_{xx}^{\beta}$, where β is determined by the mechanism under consideration [100]. In terms of the conductance σ, the skew scattering contribution to the AHE, σ_{xy}^{skew}, is $\sim \tau$, and the scaling relation becomes $\sigma_{xy}^{AHE} \sim \sigma_{xx}$ ($\rho_{xy}^{AHE} \sim \rho_{xx}$) with $\beta = 1$. The contributions independent of τ give a scaling law $\sigma_{xy}^{AHE} \sim \sigma_{xx}^0$ ($\rho_{xy}^{AHE} \sim \rho_{xx}^2$).

A model which gained in popularity in modern literature to study the AHE, is the ferromagnetic two-dimensional Rashba model [11]. There is extensive literature dedicated to this model, see [110, 111, 116–122]. The Hamiltonian for the ferromagnetic Rashba model can be written in the following form ($\hbar = 1$):

$$\hat{H}(\mathbf{p}) = \frac{\mathbf{p}^2}{2m}\hat{1} + \lambda \mathbf{p} \cdot \hat{\sigma} \times \mathbf{e}^z - \Delta_0 \hat{\sigma}_z + \hat{V}(\mathbf{r})\hat{1} \tag{1.2}$$

where **p** is the in-plane momentum, m is the electron mass, $\hat{1}$ is the unitary ma-

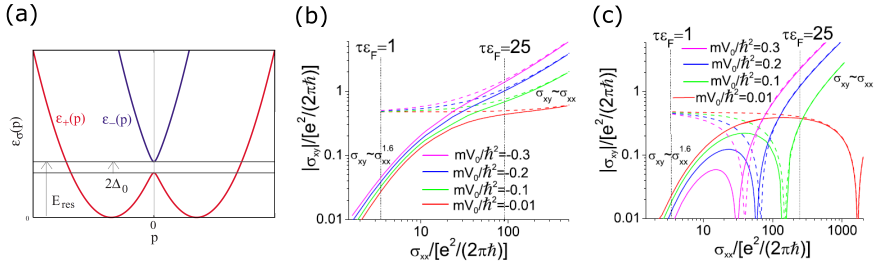

Figure 1.5: (a) The band dispersion described by Eq. 1.3 without the scattering term. The figure is reprinted from Ref. [111]. Copyright 2010 by the American Physical Society. Calculations of the absolute value of the Anomalous Hall conductivity versus the longitudinal conductivity for (b) attractive and (c) repulsive impurity potentials. Note that on the last panel, the AHE changes its sign near the cusps. The figures (b) and (c) are reprinted from Ref. [116]. Copyright 2009 by the American Physical Society

trix, λ is the Rashba SOC constant, $\hat{\sigma} = (\hat{\sigma}^x, \hat{\sigma}^y, \hat{\sigma}^z)$ are Pauli matrices, $\mathbf{e}^z$ is the unit vector in the z direction, δ_0 the mean-field exchange splitting, and $\hat{V}(\mathbf{r}) = V_0 \hat{1} \sum_i \delta(\mathbf{r} - \mathbf{r}_i)$ is a δ-scatter impurity potential, where r_i is the position of impurity i. This simple model captures most of the important features such as the intrinsic and the extrinsic contributions as well as taking into account both the majority and minority spin Fermi surfaces. The band dispersion of the Hamiltonian without the last term will be:

$$\varepsilon(\mathbf{p}) = \frac{\mathbf{p}^2}{2m} - \sigma \Delta_{\mathbf{p}} \tag{1.3}$$

$$\Delta_{\mathbf{p}} = \sqrt{\lambda^2 \mathbf{p}^2 + \Delta_0^2} \tag{1.4}$$

This dispersion is shown in Fig. 1.5a. As can be seen from the figure, there are three clear regions. The first is when only the majority band is occupied; then all mechanisms will contribute [116, 121, 122]. When the Fermi level lies in the gap, the intrinsic contribution is enhanced. The two bands have Berry curvatures with opposite signs near $\mathbf{p} = 0$, therefore a large intrinsic AHE arises only in the gap region [111, 117, 123]. When both bands are occupied, the skew scattering contribution becomes dominant [110, 111, 116, 119, 120].

A minimal model for the AHE in 3D ferromagnet can also be constructed based on the 2D ferromagnetic Rashba model. In the presence of SOI in a 3D ferromagnet, majority and minority spin Fermi surfaces will avoid touching points for a particular projection of Bloch momentum k_x along a magnetization direction. To account for most of the AHE, one can choose such $\mathbf{k}$ point that the energy gap will be minimum and, therefore, intrinsic contribution will be maximum. When expanding a Hamiltonian around the $\mathbf{k}$ point, it may be possible to obtain an effective Hamiltonian similar to Eq. 1.2. Note that in the Rashba model λ is the SOC con-

stant and Δ_0 is the Zeeman splitting, but in the minimal model λ is the Fermi velocity and Δ_0 is the SOI. Therefore, in the minimal model the SOI opens the gap [100, 111]. Moreover, the Hamiltonian of the minimal model for the general case of a 3D ferromagnet should contain Rashba-like and Dresselhaus-like contributions.

Numerical calculations of σ_{xy}^{AH} based on the Rashba model as well as on the minimal model [111, 116, 123] identified three distinct regimes: a skew scattering dominated regime ($\sigma_{xy}^{AH} \sim \sigma_{xx}$) with a crossover to an intrinsic-dominated regime ($\sigma_{xy}^{AH} \sim const$) with further crossover to an incoherent regime ($\sigma_{xy}^{AH} \sim \sigma_{xx}^{1.6}$) (Fig. 1.5b). The last regime is also referred to as a bad metal regime [100] and associated with $\sigma_{xy}^{AH} \sim \sigma_{xx}^{1.8}$ observed in some experiments. The last regime arises due to influence of finite-lifetime disorder broadening on σ_{xy}^{int}, which is quickly diminished by disorder.

All three regimes have been observed in experiments on various systems. The skew scattering has been reported in Fe doped with Co and Si [124, 125]. The bad metal regime has been identified in anastase and rutile phases of $Co_xTi_{1-x}O_{2-\delta}$ [126], Fe [127], and Fe_3O_4 [128]. The intrinsic mechanism has been reported in diluted magnetic semiconductors such as $Ga_{1-x}Mn_xAs$ [129] and metals Fe, Gd, Co, Ni [130]. However, there are some important limitations to an interpretation of experimental data based on this model. Ref. [116] showed that a change of sign of the impurity potential changes the sign of the skew scattering, and data do not collapse anymore, especially near the intrinsic to extrinsic crossover (Fig. 1.5c). Moreover, a recent study [118] found that the scaling $\sigma_{xy}^{AH} \sim const$ can also arise due to skew scattering involving rare impurities pairs, separated by a distance of order or less than the Fermi wave length [131].

1.3.2. The Anomalous Hall Effect in $SrTiO_3$-based heterostructures

For the systems of interest for this thesis, the AHE was reported in LAO/STO [36, 78, 96], in LAO/ETO/STO [132], in NGO/STO [91], in LAO/$La_{7/8}Sr_{1/8}MnO_3$/STO [133] in $LaAl_{1-x}Mn_xO_3$ (LAMO/STO) [134, 135] and in spinel/STO interfaces such as γ-Al_2O_3/STO, $CoAl_2O_4$ and $NiAl_2O_4$ [78, 136]. Interestingly, the AHE is usually observed when the $d_{xz/yz}$ band is being filled. It corresponds to the two-band regime for most heterostructures, except in case of γ-Al_2O_3/STO, where $d_{xz/yz}$ is lying lower than d_{xy} [78, 137]. Gan *et al.* obtained a rather intriguing result. In their work on LAMO/STO, they found that the AHE in the samples with a doping concentration of x=0.25 showed behavior similar to other STO heterostructures, but starting from x=0.3 the AHE is observed in the one-band regime, which corresponds to only the d_{xy} band filling [134, 135]. The AHE in STO-based structures is usually

not accompanied by *MR* hysteresis [36, 78, 91, 96] except for LAO/ETO/STO, which showed a small amount of hysteresis at very low temperatures [132]. Furthermore, Ref. [138] reported an AHE at the interface between LAO and STO doped by Fe, but in that case the AHE signal was vanishingly small, and this work is not considered further here.

The first model proposed for the AHE in LAO/STO was based on the above mentioned coupling between the $3d_{xz/yz}$ electrons and localized magnetic moments. A problem with the model is that the AHE in these systems is observed in a smaller temperature range than the range with the two band behavior. A possible explanation would be that the system should be below the Kondo temperature, but as discussed in Section 1.2.3 this picture has been seriously challenged. In LAO/ETO/STO, which has been shown to be ferromagnetic [132, 139], the situation seems to be simpler. XMCD measurements revealed the presence of a significant orbital moment of the Ti below the Curie temperature of ETO [132]. Above the Lifshitz transition, the interaction of the orbital moment of the $3d_{xz/yz}$ electrons with such localized magnetic moments can then lead to the AHE through the skew scattering mechanism [132]. As a side note, the method used in Refs. [132] to extract the magnitude of R_{xy}^{AHE} is arguable because it does not take into account any functional dependence of the AHE contribution on magnetization or magnetic field.

A more advanced model to capture the actual contribution of the AHE in presence of the 2-band behavior was proposed by Gunkel *et al.* [91]. Here, the AHE contribution was described by a Langevin-like function (essentially describing the change in polarization of the localised moment; for more details see Chapter 3). In this way, they found a linear dependence of the Anomalous Hall resistance on the longitudinal resistance for samples grown at different pressures and attributed this to skew scattering. Such a description could indicate that magnetic impurities are the main mechanism of magnetism in STO-based interfaces. Simply put, an increase of oxygen pressure should decrease the number of oxygen vacancies. In consequence, a smaller concentration of localized Ti^{3+} moments is expected, and in samples grown at higher pressure the concentration of magnetic moments should be lower. However, the authors of Ref. [91] observed *enhancement* of the AHE in samples grown at higher pressures and, therefore, excluded the oxygen vacancies as a source of magnetism. Instead, they attributed it to an indirect effect of Sr vacancies because high growth pressure leads to an enhanced number of such vacancies. The method of Ref. [91] was also used in a study on LAO/$La_{7/8}Sr_{1/8}MnO_3$/STO [133]. The authors proposed a similar picture to LAO/ETO/STO but instead of Eu^{2+} now Mn^{2+} ions play the role of scattering centers. Surprisingly, the scaling law for the AHE in LAMO/STO indicated an intrinsic mechanism as the dominant contribution to the AHE [134]. The study of

γ - Al_2O_3/STO [78] observed correlations between the ferroelastic domains and the AHE. Finally, besides the above mentioned work, [75] proposed an explanation of the AHE based on electron pairing, but (more) experiments need to be done to confirm this theory.

What is clear at the moment, is that there is no dominant view on the origin of the AHE at oxide interfaces, due to complex entanglement of AHE and Kondo-like behavior, sample variation between experiments, data analysis, and non-trivial results, as well as a somewhat over-emphasized interpretation toward skew-scattering as the only mechanism of AHE in STO-based heterostructures.

1.4. Titanates (RE)TiO_3, where Re=La, Eu and Gd

In the present work, interfaces have been studied involving $LaTiO_3$, or delta doping with $GdTiO_3$, $EuTiO_3$ and $Eu_{1-x}La_xTiO_3$. The (magneto)conductance properties of the interfaces will be considered in the corresponding chapters. Here, a brief overview is given of the growth challenges for titanates, and some bulk, thin film and basic interface properties are given.

LTO, GTO, ETO and ELTO are rare earth titanates ((RE)TiO_3) with the perovskite structure. Most of the research on (RE)TiO_3 films has been done using PLD [139–150] or MBE [151–154] as the growth technique. Growth of stoichiometric (RE)TiO_3 films is challenging due to the sensitivity to the growth conditions. In particular, in an oxygen-rich atmosphere the pyrochlore phase ($Re_2Ti_2O_7$) rather than the perovskite phase tends to form [144, 155]. Furthermore, the absence of a capping layer leads to a replacement of Ti^{3+} by Ti^{4+} in the surface layers [142, 143]. Besides, films grown on STO absorb more oxygen from the substrate, and the amount of Ti^{3+} will decrease [142, 143]. This leads to the occurrence of magnetic dead layers at interfaces and surfaces of (RE)TiO_3 films (RTO) [143, 156]. Such dead layers are paramagnetic because of the presence of Re^{3+} ions [143]. Note that in case of $EuTiO_3$ the picture will be more complicated because Eu can either be 3+ or 2+, and the oxidation process due to STO and oxygen atmosphere occurs differently.

1.4.1. $LaTiO_3$

LTO is an antiferromagnetic Mott insulator, due to the single Ti 3d electron in its trivalent state, with the orthorhombic crystal structure [157]. The antiferromagnetic ordering arises from localized Ti^{3+} moments below the Néel temper-

ature around 140 K [157, 158]. At even lower temperatures spin-canting leads to a small ferromagnetic moment [157] of around 0.45-0.57 μ_B per Ti [159–161]. The LTO/STO (001) interface is another one of the most studied conducting oxide interface system [140, 162]. Ref. [140] considered the picture to be similar to LAO/STO. In that picture conductance is arising because LTO is polar along the (001) crystal direction, and, therefore, charge transfer to the interface will occur. However, other scenarios have also been considered. In this case, the polar discontinuity can be also resolved by a variable valence of Ti at the LTO/STO (001) interface [163, 164]. Ref. [141, 162] argued that strain impose by the STO substrate is able to induce a lattice distortion and this mechanism would make the insulating LTO metallic. In addition, LTO is sensitive to chemical off-stoichiometry: La/Sr intermixing [157, 165–167], or oxygen and lanthanum off-stoichiometry [168] can transform LTO into a conducting state. Similar to LAO/STO (001) this system exhibits superconductivity [140, 169], two-band behavior [59] and shows signatures of WAL [170].

1.4.2. $GdTiO_3$

GTO is a ferrimagnetic Mott insulator with Curie temperature of 32 K [157, 171]. The magnetic moment from the seven $4f$ electrons of the Gd atom are coupled antiferromagneticaly to the magnetic moment of the one $3d$ electron of the Ti atom. The saturation magnetization is 6 μ_B per Ti [157], but in films much smaller values have been reported. GTO shows absence of hysteresis in films [144, 154, 156, 172] and bulk [157]. GTO is polar along (001) the direction like LTO and LAO and the interface between GTO and STO hosts a 2DEL [173, 174]. Similar to LTO, other mechanisms than the polar discontinuity can again be a reason for interface conductivity. So far there was no demonstration of the AHE in this system, although hysteretic and anisotropic magnetoresistance indicate the presence of magnetism in the 2DEL [173, 174].

1.4.3. $EuTiO_3$ and $Eu_{1-x}La_xTiO_3$

ETO stands out in the RTO family. Unlike the rest of Re atoms, the most common oxidation state of Eu is Eu^{2+}. Therefore, the Ti atom is in a tetravalent state in ETO and does not contribute to the magnetization. Also, ETO, like STO, is a band insulator. It also is an antiferromagnet with a Néel temperature around 5.4 K [175–181]. ETO is often considered to be cubic down to low temperatures. However, there is a debate about the presence of a cubic to tetragonal transition. Ref. [177, 178, 180,

182, 183] reported such a transition around 282 K, while Ref. [184, 185] observed a lower transition temperatures. On the other hand, the authors of [179] did not confirm the occurrence of a transition. The result was also challenged by further work of Ref. [186], who argued that, due to a small change in the ratio between the in-plane and out-of-plane lattice constants, advanced techniques are required to detect the structural transition in ETO. Another intriguing property of ETO is the coupling between the spin lattice and an infrared-active phonon in ETO [181, 187], which allows transforming the antiferromagnetic and paraelectric state into a ferromagnetic and ferroelectric one by stress [153, 187]. Moreover, the magnetic state in compressively strained ETO can be controlled by electric fields [187, 188].

ETO is not polar along (001) direction. Therefore, it cannot be used to create a 2DEL at the interface with STO by means of the polar catastrophe. Stoichiometric ETO grown on STO should be in the antiferromagnetic state because ETO is almost isostructural with STO [152]. Indeed bulk-like behavior was reported for films grown by MBE [152] and for post-annealed PLD films [147, 148]. At the same time, non-annealed films grown by PLD showed ferromagnetic behavior [147, 148, 189], which was attributed to the formation of oxygen vacancies [147] and a longer out-of-plane lattice constant [148]. Moreover, amorphous ETO also showed ferromagnetism [190]. It is possible to use ETO to delta dope LAO/STO in order to induce magnetism [132, 139]. The ETO magnetic state in these films was identified as ferromagneticaly ordered below 8 K [132, 139]. Kondo-like behavior [132, 139], WAL [191], superconductivity and gate-tunable AHE [132] have all been reported for the films.

$Eu_{1-x}La_xTiO_3$ or ELTO has different properties from ETO. Ref. [192] found that doping of bulk ETO with 10 % La introduces electrons into the conduction band of the $3d$ t_{2g} states and makes ETO a ferromagnetic metal with Curie temperature of 8 K. Further research on thin films confirmed that even 1% of La doping is enough to make ELTO conducting [145]. This compound exhibits negative *MR* indicating the exchange coupling between itinerant electrons of Ti and localized spins of Eu [192]. Note that such mechanism is distinct from GTO, where the Ti electrons are localized [192].

Ferromagnetism has also been reported in the films, but remanent magnetization was absent [145, 151]. Such behavior was explained by a change of the magnetic order from antiferromagnetic in zero field to ferromagnetic in high field [151]. Moreover, the AHE has been observed in the films prepared on LSAT substrate [145, 151]. The AHE exhibits a sign change and a dependence on the carrier concentration [145]. Authors of [145] considered it as indications of the intrinsic origin of the AHE due to the band structure, which also was supported by theoretical calculations. Indeed, correlation between the sign change of the intrinsic AHE and the

band crossing points was declared [145]. These band crossings are crossings between d_{xy} and $d_{xz/yz}$ bands, which are split due to tetragonal distortions in the films grown on LSAT [145, 151]. Intriguingly, in the films grown by MBE and in some films grown by PLD non-monotonic magnetic field dependence of the AHE has been observed [151]. Furthermore, this effect was present in oxygen deficient ETO films [151]. The authors of [193, 194], who studied Sm doped ETO films on LSAT, attributed non-monotonic behavior to an additional contribution of topological AHE. But authors of [151] argued that this behavior is due to a change of Zeeman splitting during a magnetization process.

2

Experimental Methods

2.1. Introduction

This chapter describes the experimental methods used in this work. The first section describes the thin film fabrication process, namely the preparation of a TiO_2-terminated $SrTiO_3$ surface, the growth of the films by Pulsed Laser Deposition and the use of Reflection High Energy Electron Diffraction (RHEED). The second section is dedicated to the back gate experiments performed in the Leiden measurement platform (a PPMS from Quantum Design), and in particular to the insert which was designed and built for these experiments. The last section briefly list the techniques which have been used by our collaborators.

2.2. Sample preparation

2.2.1. Termination of $SrTiO_3$

The $SrTiO_3$ substrates used in this work have a (001) orientation with 0.1-0.3° miscut angles and were purchased from CrysTec GmbH. In order to create a 2DEL at the interface of STO(001) and a polar oxide, TiO_2-termination is required [18]. The method used in this work is the somewhat altered procedure proposed by Koster *et al.* [195]:

1) (Optional) cleaning with lens paper with isopropanol;
2) Sonication for 5 min in acetone;
3) Sonication for 5 min in ethanol;
4) Sonication for 30 min in ultrapure water;
5) Etching for 30 sec in buffered HF;
6) Annealing for 1 hour for a miscut angle >0.2° and 1.5 hour for a miscut angle <0.2° at temperature 950-980 °C in a tube furnace at 100-150 ml/min O_2 flow.

The first three steps are needed to remove surface contaminants on as-received substrates. The fourth is necessary to create $Sr(OH)_2$ [195] in order to ensure removal of SrO. After etching the obtained surface will be TiO_2-terminated, but annealing at 950 °C in oxygen is required to obtain a recrystallized surface [195]. An Atomic Force Microscopy (AFM) scan of the resulting surface is shown in Fig. 2.1a. The characteristic step pattern indicates TiO_2-termination [195, 196]. The

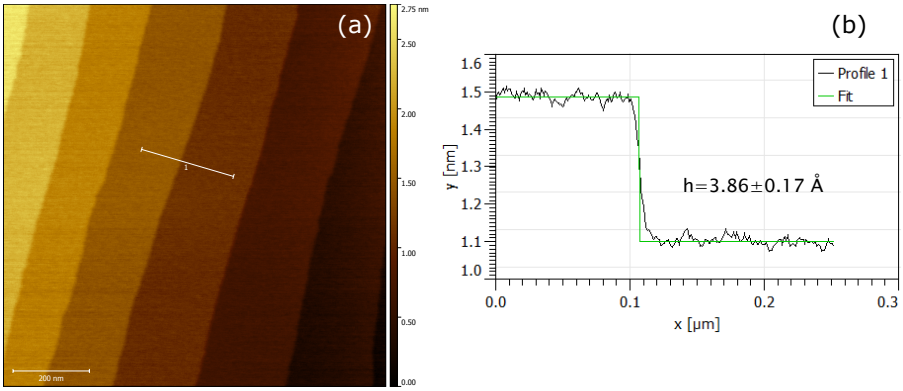

Figure 2.1: (a) AFM image of $SrTiO_3$ (001) surface after going through the single termination process and (b) line profile along the line shown in (a) with the fit to determine the step height.

height of a typical step is obtained from a fitted line profile, presented in Fig. 2.1b. The difference between the obtained value of 3.86 Å and the expected value of 3.90 Å is within the uncertainty of the fit.

2.2.2. Pulsed Laser Deposition

After the substrates were terminated, films were grown by the Pulsed Laser Deposition (PLD) technique, using the PLD-RHEED system at the University of Twente. PLD is a deposition technique which utilized high energy UV laser pulses to produce a plasma from a target material. PLD has some important advantages over other deposition techniques for the presented work such as stoichiometric transfer of material (under optimal conditions), the possibility of reactive deposition in an ambient gas, and a high kinetic energy of ablated species helping to obtain single crystalline films. Among the relevant disadvantages are a nonuniform film thickness distribution and crystallographic defects due to the bombardment of the film by high kinetic energy particles [197, 198].

The PLD-RHEED system is equipped with a UV KrF excimer laser (Laser Plasma Physik LPX Pro 210) producing at wavelength of $\lambda = 248$ nm. A set of mirrors directs the laser through a focusing lens and an optical window into a vacuum chamber to a target. The vacuum chamber has a base pressure of 3×10^{-7} mbar. At a certain position depending on the required fluency and the laser spot parameters a metal

mask (a rectangular one in this work) was mounted to select the most uniform part of the laser spot. To control the fluency, the laser voltage and an optical attenuator were used, as well as masks with different area. An energy meter was used to optimize the energy before and after the lens to ensure the correct fluency. The pulse frequency of the laser was fixed at 1 Hz.

A laser pulse, typically with an energy of a few J/cm^2, leads to rapid heating of the target material, which start to evaporate [197]. The light absorption in the vapor keeps increasing until it breaks down and a plasma forms. Further absorption heats and accelerates the plasma. In the high-density region near the target plasma particles undergo collisions leading to expansion perpendicular to the target surface. During deposition, the laser scans the target in a horizontal direction to ensure uniformity. The deposition can be performed in O_2, Ar or in a mixed atmosphere. In Ar (or any other inert gas) there will be a shock front due to collisions between the plasma and Ar atoms. In O_2 (or any reactive gas), besides the shock front, O_2 will chemically react, leading to formation of oxide molecules (if gas is O_2). The gas pressure range (either Ar or O_2) used in this work is $5 \times 10^{-5} - 1 \times 10^{-3}$ mbar. The plasma plume is directed towards the substrate, which is glued to a heater by Leitsilber 200 silver paint. Before the deposition the heater temperature is ramped up to the deposition temperature (usually in 650-900 °C range), at the deposition pressure [197]. The system does not have the possibility to rotate substrate during film growth, which can lead to a non-uniform film thickness at low pressures. Proper growth can be very sensitive to even small changes in the laser parameters such as fluency and spot size. The parameters for this can be found in the relavant chapters.

2.2.3. Reflection High-Energy Electron Diffraction

The PLD-RHEED system is equipped with a Reflection High-Energy Electron Diffraction (RHEED) setup. An electron beam is directed at a grazing angle ($\geqslant 3°$) with respect to the substrate surface and produces a diffraction pattern on a phosphorous display. A CCD camera collects images of the patterns and measures its intensities [199]. RHEED allows *in-situ* real time characterization of the film growth process. First of all, it gives information of the growth regime by monitoring the intensities of diffracted spots, in particular the specular beam. In case of step-flow growth the intensity does not change significantly because a layer start to grow from edges of the substrate steps and the overall surface morphology is

unchanged. In case of 3D growth, islands are formed, but due to low mobility of deposited particles, they do not form a complete layer before islands on the next layer start to form. The surface becomes rough very quickly, the the intensity decreases, and diffraction spot positions become independent of the angle of incidence. In case of amorphous growth, the intensity also decreases, but now also the diffraction pattern disappears. In case of layer-by-layer growth, 2D islands are formed and merge, so that after one deposited layer or unit cell, the surface is flat again. That growth mode produces (specular beam) intensity oscillations, as for instance shown in Fig. 2.2. They can be used to count the number of deposited unit cells in real time [195].

The RHEED pattern also allows to characterize the quality of the films grown. As an example, the pattern of a single crystal STO substrate at room temperature before deposition is presented in Fig. 2.3a. The pattern above the shadow line corresponds to STO. The diagonal so-called Kikuchi lines are characteristic of high crystallinity also into the depth of the crystal. The bottom spot is from the direct beam. Amorphous film growth, in this case of ELTO (sample #3), resulted in the cloudy pattern shown in Fig. 2.3b. The pattern after growing GTO (sample #12) indicates 2D growth (Fig. 2.3c), while 3D growth with some signatures of amorphization was observed after preparation of ELTO/STO sample #12 (Fig. 2.3d).

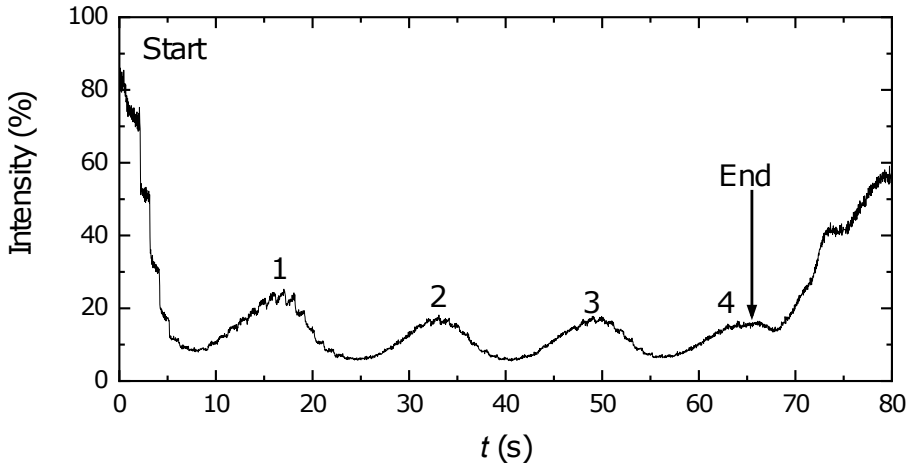

Figure 2.2: The RHEED oscillations of ELTO/STO-13.

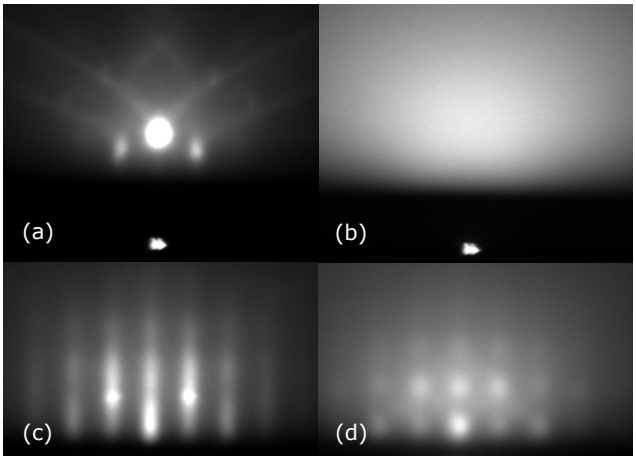

Figure 2.3: The RHEED pattern of (a) $SrTiO_3$ surface at room temperature before deposition and (b) ELTO/STO-3, (c) LGAO/GLTAO/STO-12, (d) ELTO/STO-12 after deposition.

2.3. Back gating experiments in the PPMS

In this section back gating experiments, including measurements in the so-called van der Pauw geometry are described. For a description of the physical mechanism of the back gating see Section 1.

2.3.1. Insert

In order to perform back gate experiments in our measurement platform, a PPMS from Quantum Design, a special back gate insert with proper grounding for the gating experiments was designed and built. It is shown in Fig. 2.4. Because of a tradeoff between reliability, simplicity of use, time costs and required characteristics the temperature range for use of the insert is 350 K to 3 K, instead of the 400 K - 2 K range which can be supported by the PPMS. The insert was based on a 'multifunctional probe for' the PPMS, but significant changes have been made on the original design. A few parts were left from the original probe, in particular:

1) The cylindrical probe head;

2) The O-ring on the top, which provide a vacuum-tight connection when the insert is installed in the PPMS;

3) The stainless steel tube;

4) Radiation baffles outside and inside of the tube (only the outside ones can be seen in Fig. 2.4), to minimize heat radiation between parts at 300 K and 3 K;

5) The mechanical part of the PPMS puck assembly to ensure a fixed position, when installed in the PPMS;

6) The body for mechanical attachment at the bottom of the probe.

The following parts were replaced or added:

1) The factory-made top of the head was replaced by a homemade one with a vacuum Jaeger connector (not shown in Fig. 2.4), which allows direct access to wiring without using the standard PPMS wires;

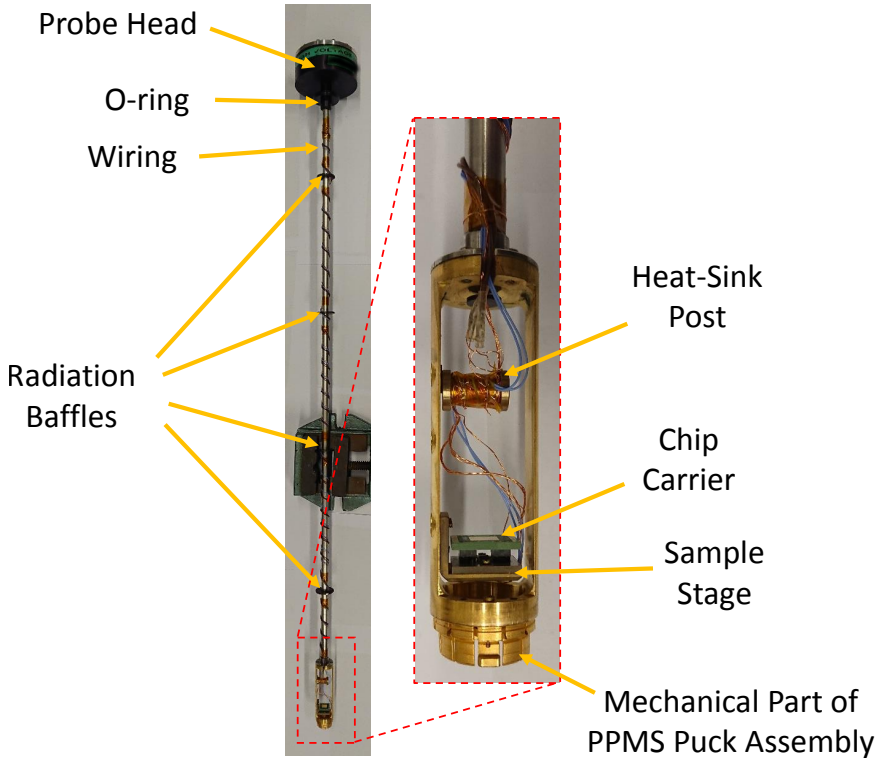

Figure 2.4: The photo of the back gate voltage PPMS insert.

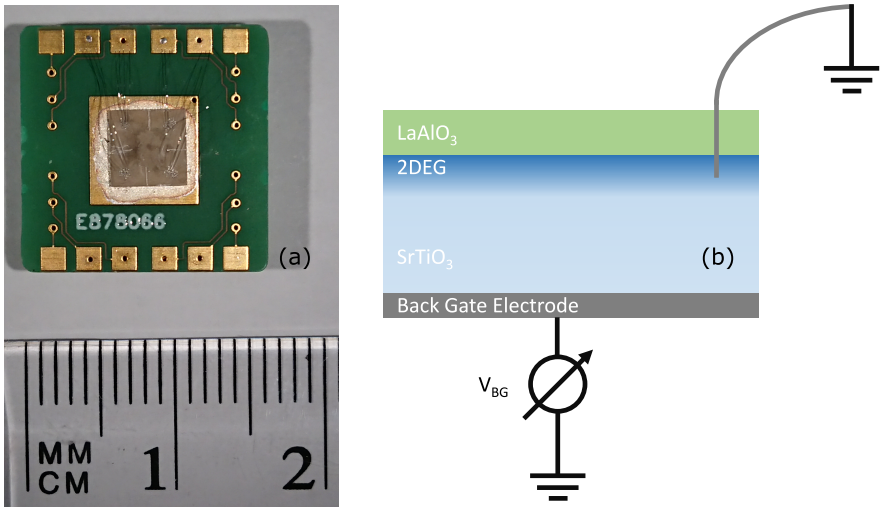

Figure 2.5: (a) Photo of a chip carrier with a mounted sample. (b) The electrical layout of the back gate voltage experiments.

2) Old wiring was removed and replaced by a new set of cables:

   (a) One twisted pair and one twisted quad of copper wires for measurements;

   (b) Two stainless steel coaxial cables with Teflon insulation for a thermometer;

   (c) One twisted pair of copper wires with Teflon insulation for back gate and ground connections;

3) A heat-sink post to thermally anchor the wiring;

4) A sample stage, which can be oriented parallel and perpendicular to the magnetic field direction;

5) The chip carriers, which have plug-in connectors for the sample stage;

6) The thermometer clamped under the chip carrier to the sample stage.

The chip carrier was also designed in-house. In Fig. 2.5a the chip carrier with a mounted sample is shown. The sample is glued by Leitsilber 200 silver paint to the central back gate electrode and connected by wires which were wirebonded from the sample to the contact pads. In Fig. 2.5b the electrical layout of the back gate experiment is presented. Most of the measurements were performed with an

AC current of about $0.1-1$ μA at frequencies $15-150$ Hz using a lock-in amplifier SR-830. To increase the lock-in input impedance, a pre-amplifier SR-550 was used. Zener (diode) clamps were connected to the lock-in inputs for protection from voltage overload. Special software in Python was written to control the measurement equipment and the MultiVu program which controls the PPMS.

2.3.2. Van der Pauw measurements

Most of results obtained in this thesis are on samples measured in the van der Pauw (VDP) geometry [200, 201]. In this geometry, four contacts are placed along the perimeter of a sample. This is not always convenient in case of oxide structures, because low pressure deposition conditions can lead to a non-uniform distribution of the material. Moreover, in order to avoid leakage currents, the sample edges have to be polished to remove silver paint remnants after PLD. This process may lead to damaged edges. To ensure measurements through the central and presumably homogeneous part of the sample, in some of them scratches were made by a diamond knife in the middle of the center of each edge, in order to block currents along the sides and only probe the central part. To measure the sheet resistance, voltage probes were always connected to the edge opposite to the edge with current leads. For the Hall resistance, the voltage probes were connected to one diagonal and the current probes to another one. Switching between the different combinations was made with a programmable relay box.

Below, the calculation of the sheet resistance and the Hall resistance from the measured set of resistances will be explained, but first some definitions need to be introduced. For the contacts named as in Fig. 2.6, $R_{ij,kl}$ is defined as follows:

$$R_{ij,kl} = \frac{V_{kl}}{I_{ij}}, \tag{2.1}$$

where V_{kl} is the voltage measured between contacts l and k, with contact l connected to $V+$ and k to $V-$; I_{ij} is the current between contacts i, connected to $I+$, and j, connected to $I-$. Two resistance-type quantities can be calculated by the following equations:

$$R^{Ho}(B) = \frac{R_{AB,CD} + R_{BA,DC} + R_{DC,BA} + R_{CD,AB}}{4}, \tag{2.2}$$

$$R^{Ve}(B) = \frac{R_{AD,CB} + R_{DA,BC} + R_{CB,AD} + R_{BC,DA}}{4}, \tag{2.3}$$

where $R^{Ho}(B)$ and $R^{Ve}(B)$ are resistances corresponding to horizontal and vertical voltages at the applied magnetic field B. Then the van der Pauw equation has to be

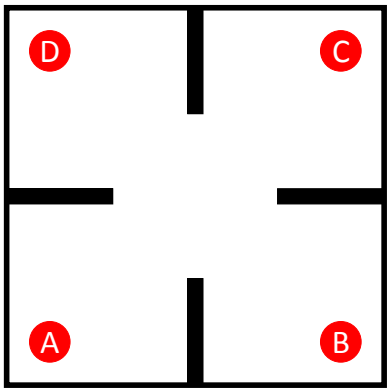

Figure 2.6: The scheme of Van der Pauw geometry. Black lines indicate scratches made to probe the central part of the sample. Letters denote the contacts.

solved:

$$\exp\left(-\pi R^{Ve}/R_S^{meas}\right) + \exp\left(-\pi R^{Ho}/R_S^{meas}\right) = 1, \tag{2.4}$$

where R_S^{meas} is the sought-for sheet resistance. Although this equation cannot be solved analytically, it can be solved numerically, for example by a Newton-Raphson method, which was used in this work. The Hall resistance can be obtained from the following formula:

$$R_{xy}^{meas}(B) = \frac{R_{AC,DB} + R_{CA,BD} + R_{BD,AC} + R_{DB,CA}}{4}. \tag{2.5}$$

After that, the data still need to be (anti-)symmetrized:

$$R_S(B) = \frac{R_S^{meas}(B) + R_S^{meas}(-B)}{2}, \tag{2.6}$$

$$R_{xy}(B) = \frac{R_{xy}^{meas}(B) - R_{xy}^{meas}(-B)}{2}, \tag{2.7}$$

This implicitly means that the measurement needs to be done both for positive and negative field directions. However, to reduce measurement time and to avoid complex electrostatic behavior in not highly conducting samples due to the switch of ground contacts for a next measurement configuration, the number of measured resistances can be limited to two, $R^{Ho}(B) = R_{BA,DC}$ and $R^{Ve}(B) = R_{DA,BC}$, for the sheet resistance, which is later used to solve the VDP equation, and one for the Hall effect measurement $R_{xy}^{meas}(B) = R_{CA,BD}$.

2.4. Additional experimental techniques

This work would not be possible without data obtained by collaborators using their own specialized techniques. Most of PLD targets used for this project were commercially purchased, but the $EuTiO_3$ and $Eu_{0.9}La_{0.1}TiO_3$ targets were pressed and sintered at the University of Amsterdam. The crystal structure of the samples was analyzed by Scanning Transmission Electron Microscopy (STEM), and Electron Energy Loss Spectroscopy (EELS) were used to obtain information about chemical composition. These STEM and EELS experiments were performed at the University of Antwerp. Scanning SQUID microscopy at the University of Twente was used to obtain information about the magnetic state of some films. Low temperature measurements, below 1 K, were performed in a Triton^{TM} dilution fridge from Oxford instruments, also at the University of Twente.

3

Gate-tuned Anomalous Hall Effect Driven by Rashba Splitting in Intermixed $LaAlO_3/GdTiO_3/SrTiO_3$

The Anomalous Hall Effect (AHE) is an important quantity in determining the properties and understanding the behavior of the two-dimensional electron system forming at the interface of $SrTiO_3$-based oxide heterostructures. The occurrence of AHE is often interpreted as a signature of ferromagnetism, but it is becoming more and more clear that also paramagnets may contribute to AHE. We studied the influence of magnetic ions by measuring intermixed $LaAlO_3/GdTiO_3/SrTiO_3$ at temperatures below 10 K. We find that, as function of gate voltage, the system undergoes a Lifshitz transition, while at the same time an onset of AHE is observed. However, we do not observe clear signs of ferromagnetism. We argue the AHE to be due to the change in Rashba spin-orbit coupling at the Lifshitz transition and conclude that also paramagnetic moments, which are easily polarizable at low temperatures and high magnetic fields, lead to the presence of AHE, which needs to be taken into account when extracting carrier densities and mobilities.

The pre-print version of this chapter has been published as N. Lebedev, M. Stehno, A. Rana, P. Reith, N. Gauquelin, J. Verbeeck, H. Hilgenkamp, A. Brinkman, and J. Aarts, *arXiv:2002.11408*.

3.1. Introduction

The two-dimensional electron system (2DES) which is present at $SrTiO_3$-based oxide interfaces is of interest as a model system for the physics of band formation and electrical transport in a quantum well where $3d$ electrons are the carriers. Moreover, the system has built-in electrical tunability, since the high permittivity of the $SrTiO_3$ substrate allows it to be used as a back gate, thereby varying the shape of the well, the number of carriers, and the population of the various $3d$ subbands. One of the still outstanding questions is whether and how the 2DES can be used as a platform for spintronics, meaning that the electron system can be (tunably) magnetically polarized and furnish not only charge current but also spin currents. The occurrence of Rashba-type spin-orbit coupling (SOC) at the interface is of obvious importance here, and it should be noted that the effect of back-gating does not only change the carrier concentration at the interface, but also changes the strength of the SOC [5, 47]. This is a somewhat subtle band structure effect in which the system switches from one- to two-carrier transport at the so-called Lifshitz point [36]. That leads to a strong increase in SOC, and to a change in coupling between itinerant electrons and localised moments. Recently, this effect was utilized for spin-to-charge conversion by injecting spin-polarized carriers [49, 202].

At the archetypical interface $LaAlO_3/SrTiO_3$ (LAO/STO), the occurrence of magnetism is still a much-debated subject, mainly because the nominal ions at the interface (including Ti^{4+}) are non-magnetic and defect physics appears to be at its origin. Using magnetic ions seems a more controlled route. Magnetic $4f$ ions can easily be substituted for La, while using titanates rather than $LaAlO_3$ yields (magnetic) Ti^{3+} ions. In this spirit, delta doping was lately used as a tool to enhance the amount of magnetic ions at the interface. In different studies, ultrathin layers of $EuTiO_3$ (ETO) [132] and (La,Sr)MnO_3 (LSMO) [133] were sandwiched between STO and LAO. Alternatively, La(Al,Mn)O_3 (LAMO; up to 30% Mn) was grown on STO in order to bring magnetic ions closer to the interface [135]. In all cases, occurrence of ferromagnetism was reported, as well as tunability of the effect with a gate voltage.

The details of the observations strongly differ, however, in particular with respect to the mechanisms behind the tunability. In ETO and LSMO, spin polarization was inferred through the occurrence of the Anomalous Hall Effect (AHE) caused by the gradual increase of the 'fast' carriers in the two-band model [132, 133]. In LAMO, a two-band model did not describe the data in samples with a high concentration of Mn, and a single band with tunable carrier concentration was used to describe the behavior of the AHE and the magnetism [135]. In our work we concentrate on two questions. One is the question of the mechanism for tunability.

We will show in particular that crossing the Lifshitz point by gating can lead to the onset of the AHE. The other is whether the observation of the AHE can be used to infer the presence of magnetic Long Range Order (LRO). Guided by observations in a very different 2DEG, MgZnO/MgO [203], we conclude that the presence of highly polarizable moments without LRO already leads to an AHE.

For our study we use delta doping by $GdTiO_3$ (GTO) which is a ferrimagnetic Mott insulator [158]. In stoichiometric GTO the oxidation state of Ti is Ti^{3+}. Therefore, GTO is polar, and the 2DEL will be formed at the GTO/STO interface. Interface conductance was indeed found in this system when grown by molecular beam epitaxy [173, 174]. The research also demonstrated signatures of magnetism such as hysteretic behaviour of the magnetoresistance and anisotropic magnetoresistance [173, 174]. AHE was not detected, probably due to the relatively low magnetic fields [173].

Films of GTO are not as easy to grow as LAO, and in the spirit of delta-doping we decided to grow heterostructure with ultrathin GTO layers, in particular LAO(8)/GTO(2)/STO, with the numeral denoting the number of unit cells. The capping layer is essential to prevent over oxidation of the surface of rare earth titanates, uncapped samples tend to form magnetic dead layers with a higher content of Ti^{4+} instead of Ti^{3+} [142, 143, 156]. Characterization by electron microscopy showed intermixing of La and Gd, leading to a structure $La_{1-x}Gd_xAlO_3/Gd_{1-y}La_yTi_{1-z}Al_zO_3$/STO (LGAO/GLTAO/STO). Still, this serves our purpose, as it constitutes a system where magnetic ions are placed at, or close to, the conducting interface. In that sense, our current work is more similar to the work on LAMO cited above. Although our structures did not show ferromagnetism, we are going to show that 2DES in this system exhibit gate-tunable AHE, but only at low temperatures, where Rashba spin-splitting is essential. In particular, we find that the AHE at 3 K develops around a positive gate voltage of about 50 V, where the system passes through the Lifshitz transition.

3.2. Experimental Details

Most of the previous studies on GTO heterostructures were performed on the films grown by Molecular Beam Epitaxy (see for example Ref. [154, 172, 204]) and only few by Pulsed Laser Deposition (PLD) [144, 205]. In this work we grow samples on TiO_2-terminated STO by PLD from an oxygen rich target $GdTiO_{3+x}$ at 850 °C at 1×10^{-4} mbar O_2 nominal pressure. The repetition rate and laser

fluency were set at 1 Hz and 1.3 J/cm^2, respectively. The samples were cooled down to room temperature at the growth pressure. The growth of the films was monitored by Reflection High-Energy Electron Diffraction (RHEED), which also yielded an estimate for the film thickness. Nominal layer thicknesses were chosen as 8 unit cell (u.c.) for LAO and 2-2.5 u.c. for GTO. As will be shown later the real thicknesses and compositions of layers were different, due to strong intermixing. Also, the growth of a GTO layer with a reliable thickness turned out to be a challenging task due to the sensitivity to the growth conditions. In particular, rare earth titanates have a tendency to form a pyrochlore phase $Re_2Ti_2O_7$ in an oxygen-rich environment [142, 172]. RHEED oscillations were hardly pronounced at the pressure we used, although the RHEED patterns did exhibit 2D growth (See Fig. 3.9 in the Appendix). At the same time, lowering of the O_2 pressure would lead to enhancement of oxygen vacancies in STO and, therefore, to the bulk conductance in STO [24].

Magnetotransport properties were measured using an automated measurement platform (a PPMS from Quantum Design) with a home built electrical insert to be able to gate the samples. They were measured in the van der Pauw geometry [200, 201] at temperatures down to 3 K and magnetic fields up to 9 T. All measured field dependencies were (anti-)symmetrised. To study magnetism, scanning SQUID microscopy measurements[1] were performed at 4.2 K without external magnetic field. A control sample showed the same qualitative behaviour as the results reported here. A second control sample was cut in two, with one part being used for analysis of the structure and chemical composition by Scanning Transmission Electron Microscopy (STEM) and Electron Energy Loss Spectroscopy (EELS)[2]. The other part was used for transport measurements and showed results which were consistent with the earlier two samples.

3.3. Results

3.3.1. TEM characterisation

Analysis by STEM revealed that the films are crystalline (Fig. 3.1a). At the same time EELS analysis indicated a severe intermixing in the sample (Fig. 3.1b). In par-

[1] The scanning SQUID microscopy experiments were performed by Dr. Pim Reith at the University of Twente

[2] The STEM and EELS experiments were performed by Dr. Nicolas Gauquelin at the University of Antwerp

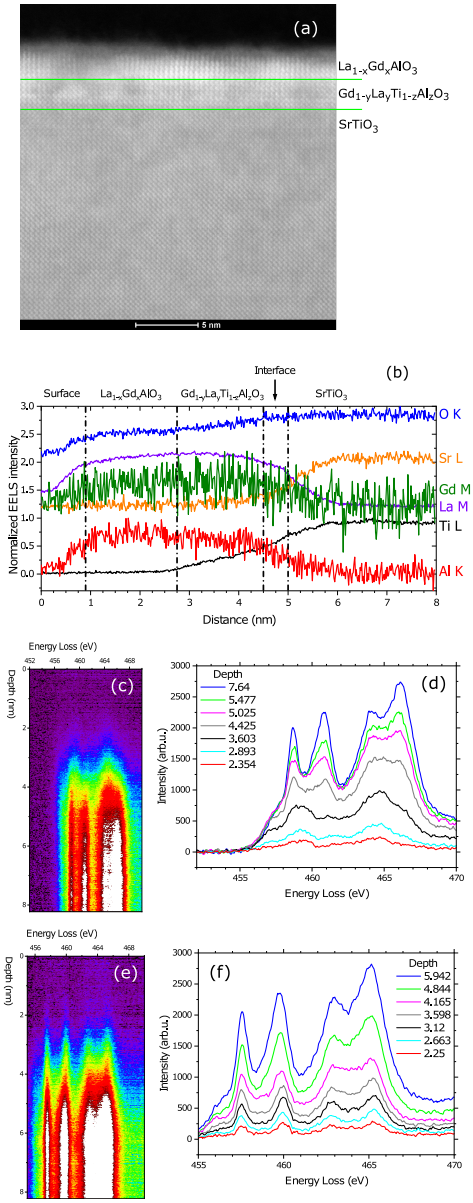

Figure 3.1: (a) TEM image of the crystal structure at and close to the interface. The green lines show the position of the interface with STO, mainly from the Sr EELS data; and the presumed interface between GTO and LAO, taken from the Ti EELS data. (b) EELS analysis of spatial distribution of the various elements. (c) Ti L edge and (d) corresponding spectra in region with presence of Ti^{3+} in GLTAO layer. (e) Ti L edge and (f) corresponding spectra in region without of Ti^{3+} in GLTAO layer.

ticular strong interdiffusion of Gd, La and Al is present over the whole thickness of the deposited layers, turning them into $La_{1-x}Gd_xAlO_3$ and $Gd_{1-y}La_yTi_{1-z}Al_zO_3$ instead of LAO and GTO respectively. Sr diffuses about 1 nm into the film whereas Ti diffuses further (around 2 nm)(Fig. 3.1b) yielding a thickness of GLTAO layer of about 5 u.c. Further investigation of the structure of the $Gd_{1-y}La_yTi_{1-z}Al_zO_3$ layer showed a varying amount of Ti^{3+} and Ti^{4+} along the film, as revealed by the study of the fine structure of the Ti L edges shown in figures 3.1c-f. In the first 'GLTAO' region shown in Fig. 3.1c,d, Ti is purely in the Ti^{3+} state (black, light blue and red spectra in Fig. 3.1d), whereas in the second 'GLTAO' region in Fig. 3.1e,f the most of Ti is Ti^{4+}. Data on the O K edge are shown in the Appendix 3.6. Clearly, in spite of the capping with LAO, which should enhance the concentration of Ti^{3+}, the growth of films in O_2 atmosphere as well as the choice of STO as a substrate increases the concentration of Ti^{4+} in the (RE)TiO_3 layer [142, 143]. Although the stoichiometric gradient in our films was not intentional, we stress again that transport properties presented in the rest of the Results section are reproducible in the control sample. Such robustness is understanable because the conducting media is a single crystal STO substrate, which properties govern most of the heterostructure physics.

3.3.2. Basic transport properties

LGAO/GLTAO/STO is conducting and exhibit temperature dependence of sheet resistance(R_S), which is comparable to LAO/STO [95] (Fig. 3.2a). Also the magnetoresistance *MR* and the Hall resistance R_{xy} were measured during cooldown. The magnetoresistance (*MR*) was calculated as:

$$MR = \frac{R_S(B) - R_S(0)}{R_S(0)} \cdot 100\%. \tag{3.1}$$

As shown in Fig. 3.2b, the *MR* changes shape from almost flat to parabolic with decreasing temperature. At 3 K we note a different shape with a rather sharp dip around zero field, which indicates the appearance of Weak Anti-localization (WAL), similar to what was shown earlier for LAO/ETO/STO [191] and LAO/STO [5, 44]. The Hall coefficient R_H was extracted by dividing the Hall resistance by the applied field, $R_H = R_{xy}/(\mu_0 H_a)$. As shown in Fig. 3.2c, R_H starts to deviate from flat behavior (meaning a Hall resistance linear in the applied field) below 70 K. Such non-linear behaviour signals the presence of highly mobile $3d_{xz/yz}$ carriers [36, 37]. At 3 K, a second non-linearity occurs at lower fields, in which the slightly parabolic shape around zero field becomes inverted. Such behavior has already been observed in other STO-based heterostructures and was identified as a signature of AHE [36, 91, 132]. All in all, the basic transport characteristics show a behavior which is quite typical for that of the LAO/STO family.

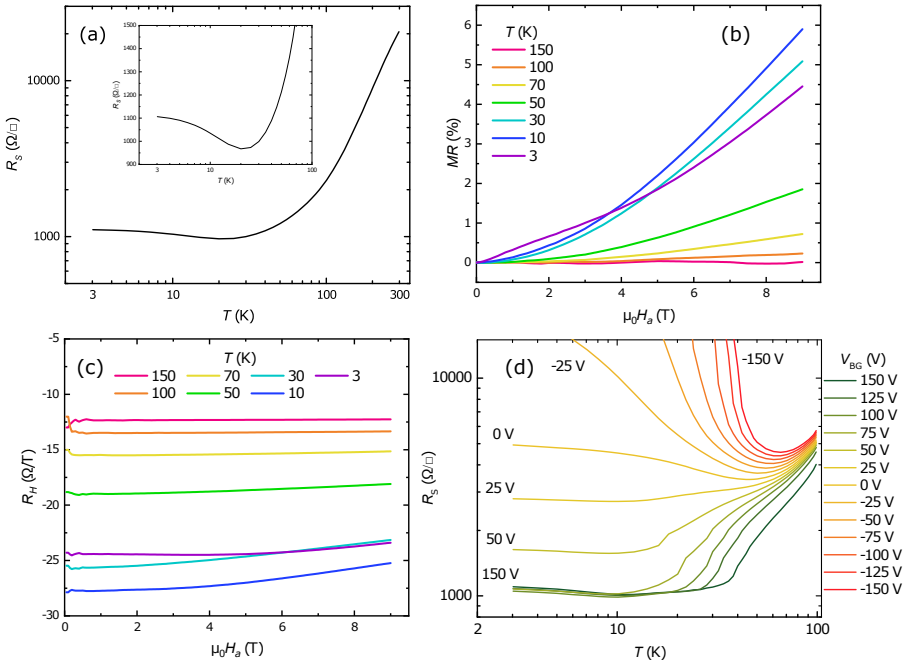

Figure 3.2: (a) Temperature dependence of the sheet resistance R_S of the LGAO/GLTAO/STO sample during cool down. The inset shows the same data with linear Sheet resistance scale in lower temperature region. (b) Field dependence of the magnetoresistance MR and (c) field dependence of the Hall coefficient R_H. (d) Sheet resistance R_S versus temperature at different back gate voltages V_{BG} in the range from 150 V to -150 V as indicated.

3.3.3. Effects of gating

Next, we studied the behavior of the LGAO/GLTAO/STO sample upon applying a back gate voltage V_{BG}. Gating results in a tunable Metal-Insulator Transition (MIT), as shown in Fig. 3.2d. The $R_S(T)$ curves were measured by cooling down from 100 K at constant applied gate voltage. The change of the gate voltage, going down from 150 V, was always performed at 3 K. Below -25 V, the system becomes insulating at low temperatures. We do not observe saturation of R_S in our samples, similar to delta-doped samples with $SrTi_{1-x}Mn_xO_3$ [206] but in contrast to such materials as ETO and $LaCrO_3$, where a Kondo-like effect with saturation at low temperatures [139, 207] was observed. Furthermore, the system shows incipient Weak Localization (WL) behavior (see below), which also has been observed in LAO/STO [5, 44, 208]. In the range from -25 V to 0, a pronounced minimum appears as function of temperature. For positive gate voltages, a small upturn in R_S can be observed. Ref. [91] indicated a correlation of a similar upturn and the emergence of AHE in a similar 2DES system, $NdGaO_3$/STO (NGO/STO). At the same time, the *MR* changes shape from incipient WL to WAL, which disappears at high positive V_{BG}. All data confirm that the behaviour of LGAO/GLTAO/STO follows the scenario well known for LAO/STO, with the presence of a localised phase at negative V_{BG}, and a cross-over to a conducting phase at positive V_{BG}, ascribed to a strong change in (Rashba) spin-orbit interaction by Caviglia *et al.* [5].

To better understand the transport behaviour at low temperatures, and in particular at the lowest temperature of 3 K, we studied the evolution of the magnetotransport properties as function of back gate voltage more closely at three different temperatures, 40 K, 15 K and 3 K. All gate voltage sweeps were made by sweeping from 150 V to downward, ending at 0 V for 15 K and 3 K because of the MI transition. Comparing the results shows significant changes occurring when going to the lowest temperature. At 40 K the *MR* is small and has a parabolic shape in the whole range of gate voltages (Fig. 3.3a). At 15 K (Fig. 3.3b) and 3 K (Fig. 3.3c) the shape, in particular at low V_{BG} diverges from parabolic, and a negative *MR* appears in high field. The (negative) Hall resistance at 40 K decreases with decreasing gate voltage, but increases at 15 K and 3 K (Fig. 3.3d-f). The Hall coefficient R_H shows that the Hall effect is non-linear in the whole range of voltages at 40 K (Fig. 3.3g). At 15 K it becomes non-linear above 25 V and at 3 K above 50 V (Fig. 3.3h,i). As was mentioned above, this non-linearity of the Hall effect in high fields indicates the presence of $3d_{xz/yz}$ carriers, and their appearance signals that the system passes through the Lifshitz point. This is of obvious importance for the extraction of carrier concentrations and mobilities [36, 37].

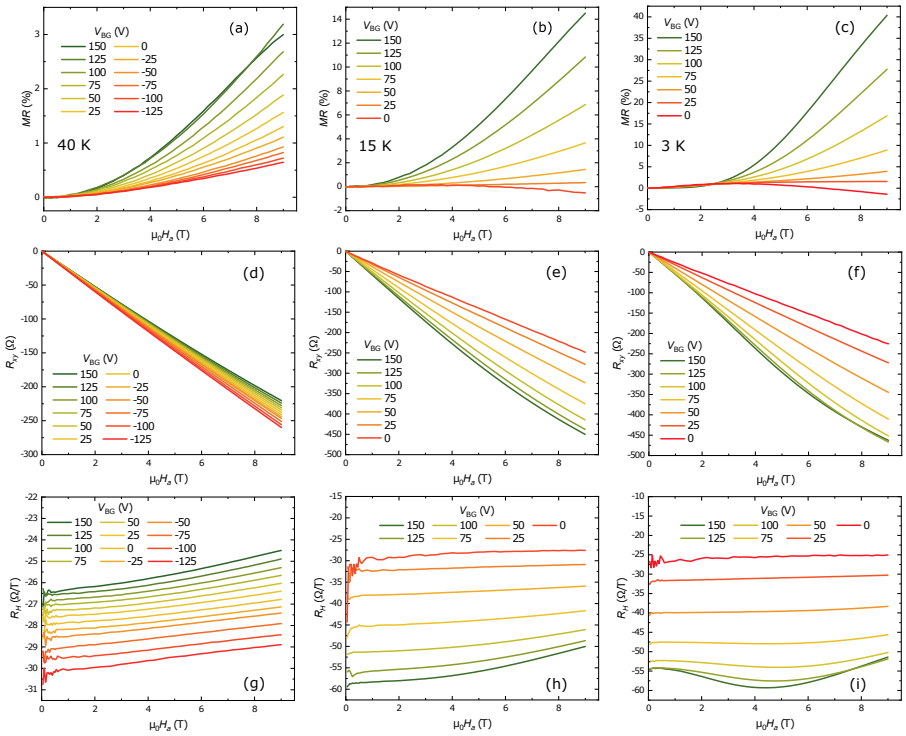

Figure 3.3: Magnetoresistance *MR*, Hall resistance R_{xy} and Hall coefficient R_H of the LGAO/GLTAO/STO sample for different positive back gate voltages V_{BG} as indicated at the temperatures of 40 K (a, d, g), 15 K (b, e, h) and 3 K (c, f, i).

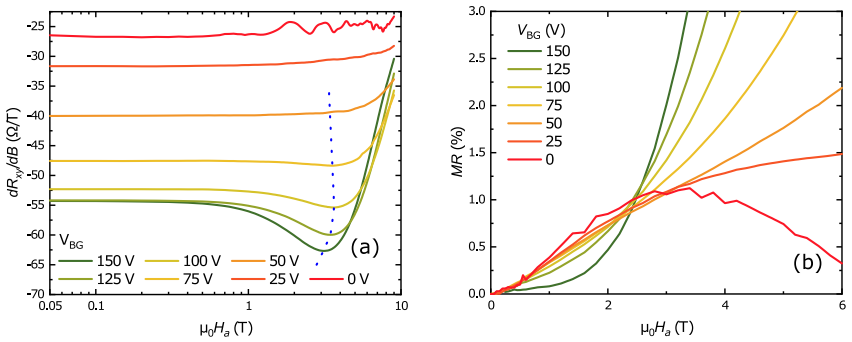

Figure 3.4: (a) The derivative of the Hall resistance R_H with respect to applied magnetic field H_a (logarithmic scale), $dR_{xy}/d(\mu_0 H_a)$, at different positive gate voltages V_{BG}, for the LGAO/GLTAO/STO sample. The dotted line is to guide the eye. (b) Magnetoresistance MR for different V_{BG} at 3 K. The data are the same as in Fig. 3.3c, zoomed-in around the axes origin.

3.3.4. The question of ferromagnetism

In the previous section we found, below 70 K and above the gate-induced Lifshitz transition, a characteristic dip structure in the field dependence of R_H (Fig. 3.3i), which indicates the presence of the AHE. Appearance of this dip above 50 V can be better seen in dR_{xy}/dB field dependence plotted in Fig. 3.4a. The observation confirms the crucial role of $3d_{xz/yz}$ carriers in the AHE and is in agreement with previous results on LAO/ETO/STO [132]. However, we did not observe AHE at 15 K and 40 K in spite of the clear presence of the second type of carriers (Fig. 3.3g,h). At these temperatures signatures of WAL were completely absent, indicating a possible important role for SOC in observation of AHE. Although the onset and increase of the AHE with increasing gate voltages is accompanied by the disappearance of WAL (Fig. 3.4b), Stornaiuolo and co-workers argued that the appearing of AHE may mask spin-orbit coupling rather than suppress it [191]. Moreover, with increasing gate voltage the carrier concentration is also increasing, leading to a stronger contribution of orbital effects in out of plane MR.

The occurrence of AHE is often taken as a signature of ferromagnetism, but we were not able to detect any hysteresis in our magnetotransport measurements down to 3 K. The same behaviour was reported for an interface between paramagnetic NGO and STO [91]. The occurrence of AHE was explained with the polarization of magnetic moments, more specifically by the rotation of moments around the out-of-plane hard axis in a magnetic field perpendicular to the sample surface [7]. In order to investigate this further, we performed measurements

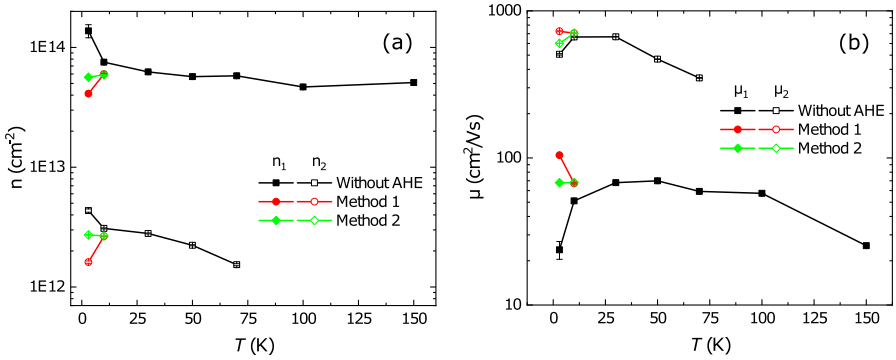

Figure 3.5: (a) Carrier concentration n and (b) mobility μ versus temperature for the LGAO/GLTAO/STO sample.

with a scanning SQUID microscope [209] on non-gated samples and samples gated at 150 V, 0 V and -150 V. The resulting scans did not show any signatures of ferromagnetic domains at 4.2 K, nor did they show ferromagnetic patches such as observed by scanning SQUID in LAO/STO structures [6, 210, 211]. This could be due to the fact that domains are smaller than our resolution. At the same time, however, EELS data indicated the presence of regions with Ti^{3+} and regions without it, and such a distribution of Ti^{3+} can lead to superparamagnetic behaviour. The measurement setup did not allow to apply a magnetic field and gate voltage simultaneously so we cannot completely exclude a scenario of superparamagnetic rather than paramagnetic behaviour, in which larger ferromagnetic domains form in an external magnetic field. Also, the absence of a change in the ferromagnetic landscape when applying a gate voltage is consistent with study on LAO/STO [210]. The premise for the remainder of the chapter therefore is that the magnetic Ti- and Gd-moments which are present, are polarizable but not ordered. The question to be answered is whether a meaningful AHE contribution can be extracted from the data, and then how to extract meaningful numbers for the carrier concentrations and mobilities, using Hall effect measurements in which AHE are present.

3.3.5. Extracting the Anomalous Hall Effect

Firstly, we calculate the longitudinal G_{xx} and transverse G_{xy} conductance from the relationship between resistance and conductance.

$$G_{xx}(B) = \frac{R_S(B)}{R_S^2(B) + R_{xy}^2(B)}, \tag{3.2}$$

$$G_{xy}(B) = \frac{-R_{xy}(B)}{R_S^2(B) + R_{xy}^2(B)}, \tag{3.3}$$

Then, to extract carrier concentrations and mobilities, we fit both of them using a two-band model.

$$G_{xx}(B) = \frac{en_1\mu_1}{1+\mu_1^2B^2} + \frac{en_2\mu_2}{1+\mu_2^2B^2}, \tag{3.4}$$

$$G_{xy}(B) = \frac{en_1\mu_1^2B}{1+\mu_1^2B^2} + \frac{en_2\mu_2^2B}{1+\mu_2^2B^2}, \tag{3.5}$$

where e is the elementary charge. The temperature dependencies of both quantities is shown in Fig. 3.5 and yields the usual picture. We find a high-mobility band with low carrier concentration (of order 3×10^{12} cm^{-2}) and a low-mobility band with high carrier concentration (of order 8×10^{13} cm^{-2}). The data at 3 K show sharp changes in all values, however, because the model does not capture the 'magnetic' contribution of the AHE to the Hall data which we will call R^{AN} . Gunkel *et al.* [91] showed that this additional contribution can be described as the behaviour of a superparmagnet, which essentially is the Langevin function for the paramagnetic behavior of a cluster of magnetic moments :

$$R^{AN}(B) = R_{xy}^{AHE} tanh\left(\frac{B}{B_c}\right). \tag{3.6}$$

Here R_{xy}^{AHE} is the Anomalous Hall coefficient and B_c is another fitting parameter which takes over the role of temperature in the original Langevin description in setting the energy scale for the field.

In a different approach, Maryenko *et al.* [203] used a Brillouin function to describe the non-hysteretic Anomalous Hall effect in a non-magnetic 2DEG based on the very different system MgZnO/ZnO :

$$B_J(x) = \frac{J+1}{2J} coth\left(\frac{J+1}{2J}x\right) - \frac{1}{2J} coth\left(\frac{1}{2J}x\right), \tag{3.7}$$

where

$$x = \frac{gM_{eff}\mu_B JB}{k_B T}, \tag{3.8}$$

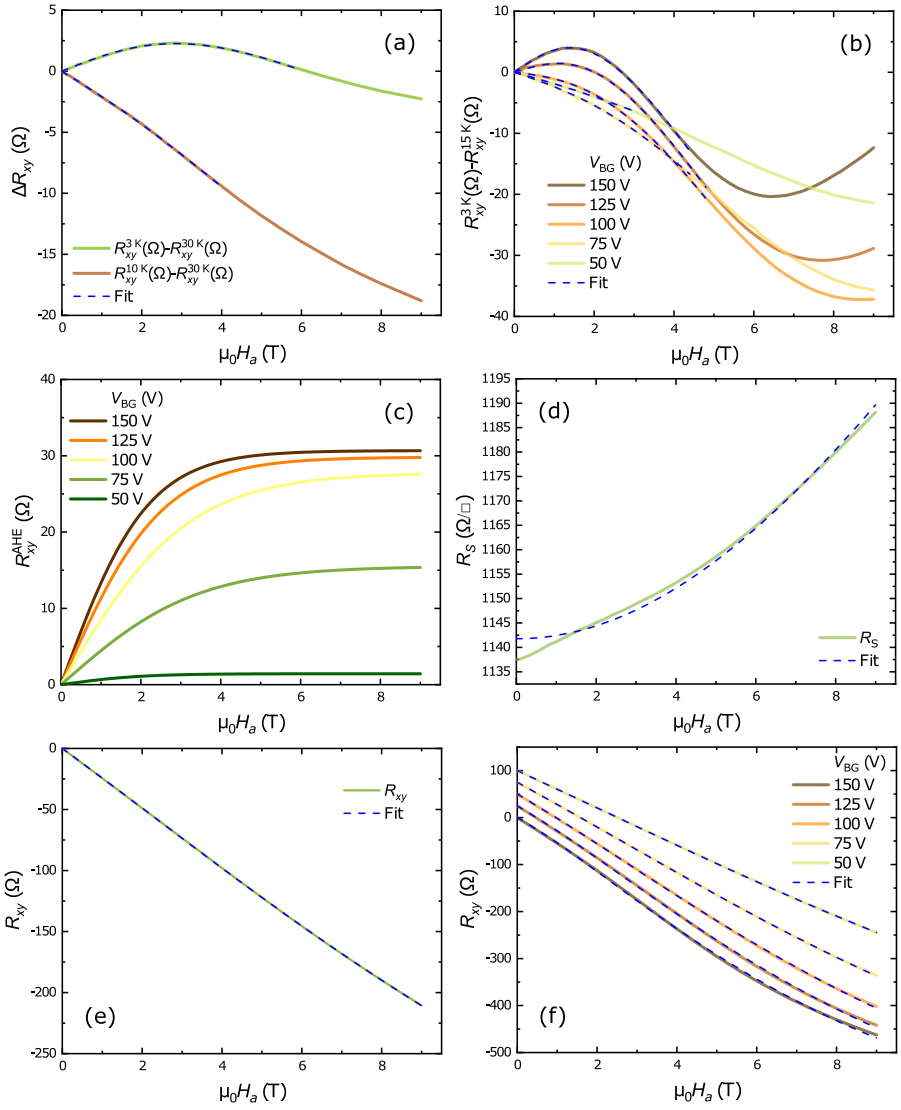

Figure 3.6: (a) Result of the subtraction of the Hall resistance R_{xy}^{10K} measured at 10 K from the curve measured at 3 K before applying a back gate voltage V_{BG}. (b) Subtraction of the curves measured at 15 K and V_{BG} from curves measured at 3 K (solid lines) and fit with Eq. 3.10 (dotted lines). (c) Resulting AHE field dependence obtained from the fit by Method 1 (see text). Fit of (d) sheet resistance R_S and (e) Hall resistance R_{xy} by Method 2 at 3 K before applying the gate voltage. (f) Fit of R_{xy} at different V_{BG}. An offset of 25 Ω between curves was added for clarity.

g is the g-factor, J is the total orbital angular momentum, and M_{eff} is the effective magnetic moment averaged over the whole sample in units of the Bohr magneton (μ_B). In the case of $g = 2$ and $J = 1/2$ eq. 3.7 reverts to Eq. 3.6 :

$$R^{AN}(B) = R_{xy}^{AHE} tanh\left(\frac{M_{eff}\mu_B B}{k_B T}\right), \tag{3.9}$$

with M_{eff} and R_{xy}^{AHE} both fitting parameters.

Based on this last function we implemented two ways to extract the carrier concentrations at 3 K. The first one is a "subtraction" method or method 1 later in the text. The idea is simply that in a small range of temperatures the mobilities and concentrations would not change abruptly or too much, and it will be possible to find the AHE by subtracting the Hall resistance curve at higher temperature without AHE from the Hall resistance curve with AHE at lower temperature. Fig. 3.6a shows the result of subtracting R_{xy}(30 K) from R_{xy}(3 K) and R_{xy}(10 K) before applying a back gate voltage. As can be seen from Fig. 3.6a the AHE contribution at 3 K is clearly visible as a Brillouin-like function. At 10K the contribution is much smaller. Also, the slope of the residual linear contribution is negative for the 10 K - 30 K subtraction, as a consequence of the behavior of R_H shown in Fig. 3.2c where the 10 K curve is shifted upward with respect to the 30 K curve. The AHE contribution at 3 K can be fitted quite well with Eq. 3.9 when we add a linear residual low field ordinary Hall resistance :

$$\Delta R(B) = R_{xy}^{AHE} tanh(\frac{M_{eff}\mu_B B}{k_B T}) + a\, B, \tag{3.10}$$

where a is the slope of residual Ordinary Hall Resistance in low field and one of the fitting parameters, along with R_{xy}^{AHE} and M_{eff}. The fit yields R_{xy}^{AHE}=9.3 Ω and M_{eff}=1.33 for 3 K and R_{xy}^{AHE}=1.78 Ω and M_{eff}=6.03 for 10 K. Fitting the Brillouin function (Eq. 3.7) with higher J does not improve the fit. In a similar way we subtracted curves at 15 K from 3 K measured at different gate voltages (Fig. 3.6b). In this case the residual linear contribution is negative because of the increase in carrier concentration, especially of the high mobility type, after passing through the Lifshitz transition. Fig. 3.11 in the Appendix 3.6 shows the result of subtraction of curves at 40 and 15 K at different gate voltages. In that case only a high field nonlinearity is present. Fig. 3.6c shows the curves as they came out from fitting Eq. 3.9. These curves were then subtracted from R_{xy} in order to be able to use Eq. 3.4 and Eq. 3.5 and obtain carrier concentrations and mobilities.

The second method (method 2) is based on directly fitting R_S and R_{xy}, using a

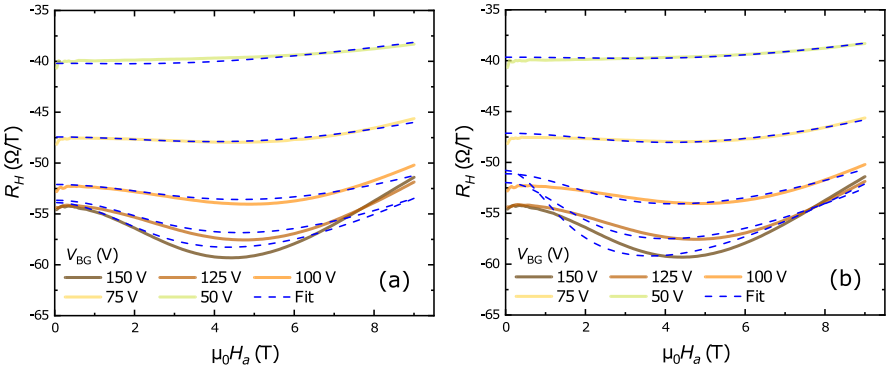

Figure 3.7: Hall coefficient R_H at 3 K and different gate voltages V_{BG} (solid lines) and fit by (a) Method 1 and (b) Method 2 (dotted lines).

model similar to the one used by Gunkel *et al.* [91]:

$$R_S(B) = \frac{G_{xx}(B)}{G_{xx}^2(B) + G_{xy}^2(B)}, \tag{3.11}$$

$$R_{xy}(B) = \frac{-G_{xy}(B)}{G_{xx}^2(B) + G_{xy}^2(B)} + R^{AN}(B), \tag{3.12}$$

where $R^{AN}(B)$ is in form of Eq. 3.9. To make the fit converge, the mobility of the low mobility carriers was fixed at the value obtained from the fit at 15 K. Fitting of the curves before applying the gate voltage gives a result quite close to that of Method 1: R_{xy}^{AHE}=4.36 Ω and M_{eff}=1.78 for 3 K and R_{xy}^{AHE}=3.13 Ω and M_{eff}=4.41 for 10 K. The fitted curves for the initial cool down are shown for R_S in Fig. 3.6d and for R_{xy} in Fig. 3.6e. The fit of the sheet resistance is not able to catch the WAL behavior at low field (Fig. 3.6d), but otherwise it works well. The resulting fits for the Hall resistance are displayed in Fig. 3.6f.

Both methods remove the sharp increase of carrier concentrations and decrease of mobilities at 3 K (Fig. 3.5). However, a closer look at the Hall coefficient (Fig. 3.7), which is a more sensitive parameter than R_{xy} itself, reveals that the first method describes the low field dependence better, while the second one is better for the high field dependence. The non-ideal fits probably arise because both Method 1 and Method 2 use empirical functions proposed by Gunkel *et al.* [91] whereas, in the presence of two bands, analysis of the conductance is the more proper way to do it. However, in the absence of a theory for AHE, it is hard to find appropriate form of the AHE term in conductance representation. The resulting fitting parameters n, μ, R_{xy}^{AHE} and M_{eff} for both methods are presented in Fig. 3.8,

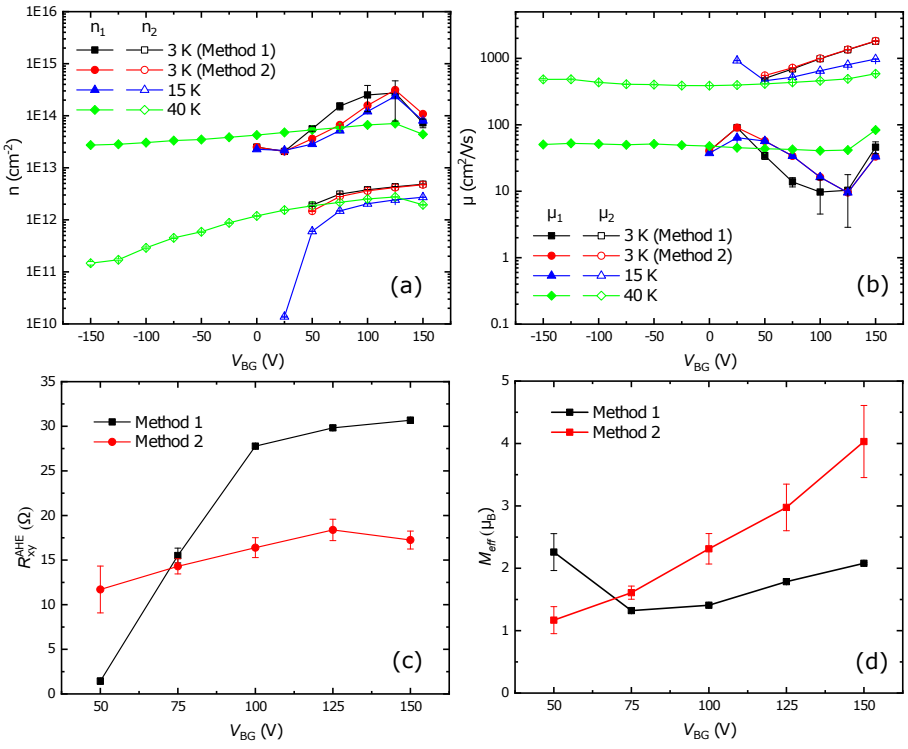

Figure 3.8: (a) Carrier concentration, and (b) mobility as function of gate voltage for different temperatures. (c) Anomalous Hall coefficient and (d) magnetic moment versus backgate voltages at 3 K.

which can be considered as one of the main results of the chapter.

We can note a few things. At 40 K a value for the carrier concentration of the second band is found for all gate voltages (Fig. 3.8a). For 15 K and 3 K, those carriers are only found for positive gate voltage. Carriers from the first band show a significant increase in concentration and a significant decrease in mobility upon gating at 15 and 3 K (Fig. 3.8a,b). Generally, the results of both methods to extract carrier concentration and mobility in the presence of AHE do not show significant differences, especially for the high mobility carriers. R_{xy}^{AHE} extracted by method 1 shows more increase, whereas the results obtained by method 2 are less clear due to larger error bars(Fig. 3.8c). The results of method one show saturation behavior, similar to what was found for LAO/ETO/STO [132]. The magnetic moment (M_{eff}) shows an increase with increasing gate voltage(Fig. 3.8d), which is possibly linked to the increasing carrier concentration of the low mobility band.

3.4. Discussion

We have shown in the previous sections that, in particular at 3 K, a non-hysteretic AHE contribution to the Hall resistance can be found above a certain gate voltage. Here we discuss its possible origins. Naively, the answer could be that ferromagnetism is induced by the insertion of ferrimagnetic GTO and gate-doping enough carriers to have sufficient exchange interaction. However, we were not able to detect ferromagnetic regions by scanning SQUID microscopy. Taking together the results of EELS and scanning SQUID, we conclude that our GLTAO layer is rather in a paramagnetic or superparamagnetic state than ferrimagnetic, due to strong intermixing. Strictly speaking, AHE need not be signature of ferromagnetic order. A growing number of reports, both theoretical and experimental, shows that it can be seen in other systems, for example in paramagnets [117, 212–215], including the already mentioned system MgZnO/MgO [203], in superparamagnets [216–218], in antiferromagnets [219, 220] and recently in $LaAlO_3/SrTiO_3$ through magnetism at ferroelastic domain walls in the STO [78].

In our case, the AHE increases with gate voltage and therefore appears to be connected to the transition through the Lifshitz point and the onset of conductance through a second band. This allows for two new mechanisms to appear. One has to do with the magnetic interactions. The d_{xy} band is circular, lies in the plane of interface, and $3d_{xy}$ electrons are coupled antiferromagnetically to magnetic moments [90, 96]. The $d_{xz/yz}$ bands, on the other hand, have highly elliptical Fermi

surfaces directed along crystal axes and the $3d_{xz/yz}$ electrons are thought to couple ferromagnetically to the local Ti^{3+} magnetic moments [90, 96]. Ferromagnetic interactions therefore may appear beyond the Lifshitz point. The other and probably more important mechanism is the enhanced Rashba spin splitting occurring near the band crossing between the light and heavy bands [35, 221], which leads to amplified spin-orbit coupling [98, 222]. Specifically, it has been shown that the characteristic spin-orbit fields can increase almost an order of magnitude with increasing gate voltage [5, 47, 48]. Against this picture pleads that AHE in our system has been observed only at temperatures around or below 10 K, whereas the two band behaviour is generally observed in a much wider temperature range. First, it should be remembered that, if the system is (super)paramagentic, the magnetization will decrease quickly with increasing temperature. Moreover, the physics here is more complicated than in the case of semiconductors. Diez *et al.* [98], for instance, showed that, around the Lifshitz point, the density of states increases steeply with band energy which leads to a strong lowering of the chemical potential between about 5 K and 20 K, and a different distribution between filled and empty states available for scattering. Such effects should also affect the strength of SOC and the generation of the AHE. All in all, there are ample indications that the gate-induced onset of AHE at the lowest temperatures is due to the physics of the Lifshitz-point, while the disappearance of AHE at higher temperature, notwithstanding the presence of two bands, could be explained by the same physics. The proposed mechanism can also give a new insight in the AHE dependence on oxygen pressure reported by Ref. [91]. In that work, the authors proposed that magnetism is controlled (indirectly) by Sr vacancies and not by oxygen vacancies. High growth pressure leads to enhancement of the amount of Sr vacancies, and of AHE, but to a smaller number of oxygen vacancies, and consequentially to a smaller concentration of localized Ti^{3+} moments. At the same time, oxygen vacancies do not just control magnetism, they determine the electrostatic boundary conditions of the quantum well [223] and thus the band filling and the strength of the SOC, which is essential for the AHE as has been discussed earlier in the text.

3.5. Conclusion

In conclusion, we have observed the occurrence of the Anomalous Hall Effect in intermixed layers of LGAO/GLTAO on STO upon applying a positive back gate voltage at low temperatures, and without observing signs of ferromagnetism. We implemented an alternative method to the one of Ref. [91] in order extract the AHE coefficient, as well the carrier concentrations and mobilities in the two band electron system. We pointed out that the onset of AHE is found at low temperatures when

the system undergoes a Lifshitz Transition and Rashba spin splitting is enhanced. The physics we observe appears to be quite robust, and relatively independent of the 2DES system being researched.

3.6. Appendix

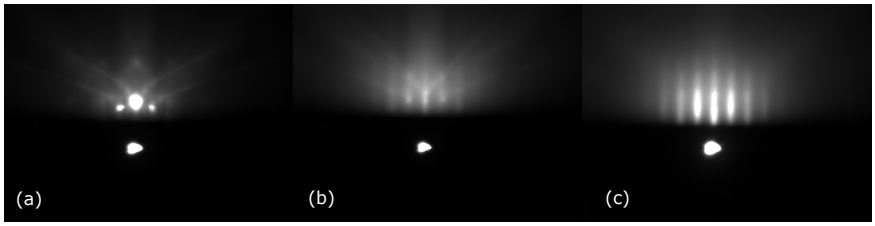

Figure 3.9: RHEED patterns (a) before deposition at room temperature, (b) after deposition of $GdTiO_3$ and (c) after deposition of $LaAlO_3$ at 850°C.

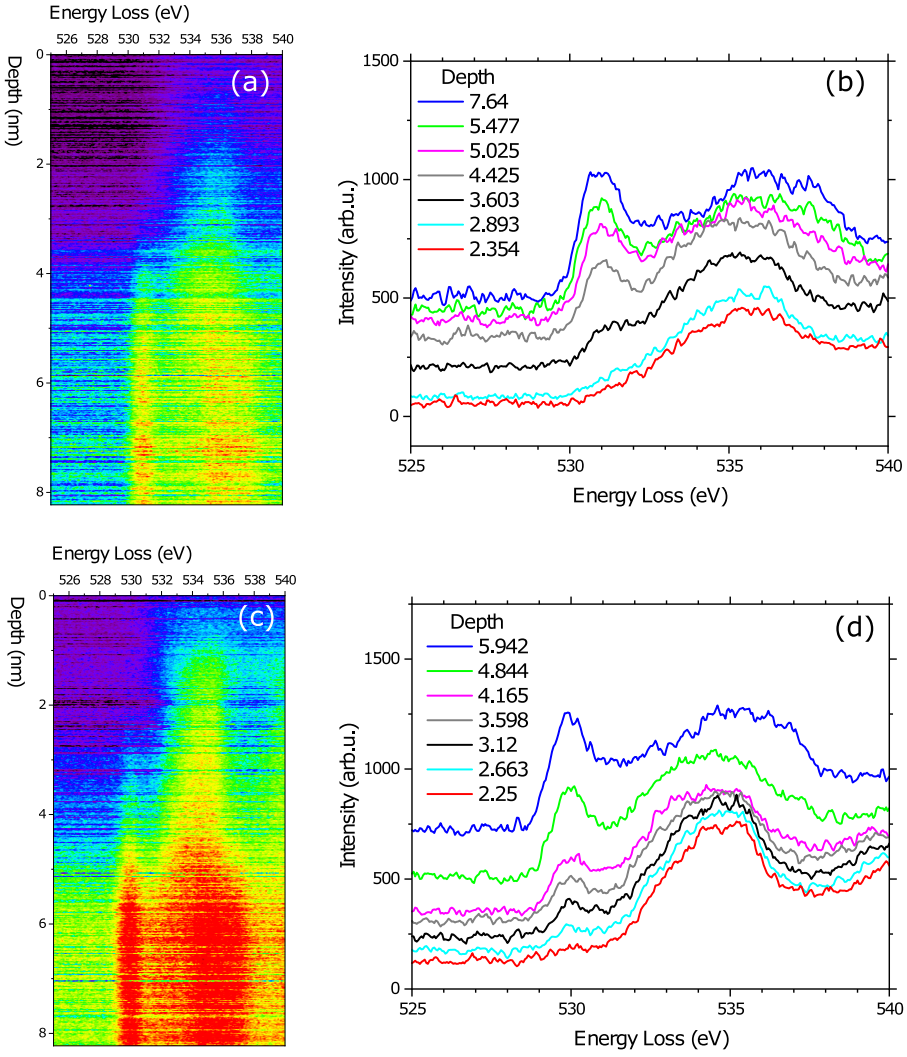

Figure 3.10: EELS data; (a) O K edge signal as function of distance from the interface in a region where Ti^{3+} is present in the GLTAO layer and (b) corresponding spectra in that region. (c) O K edge in a region where Ti^{3+} is absent in the GLTAO layer and (d) corresponding spectra in that region.

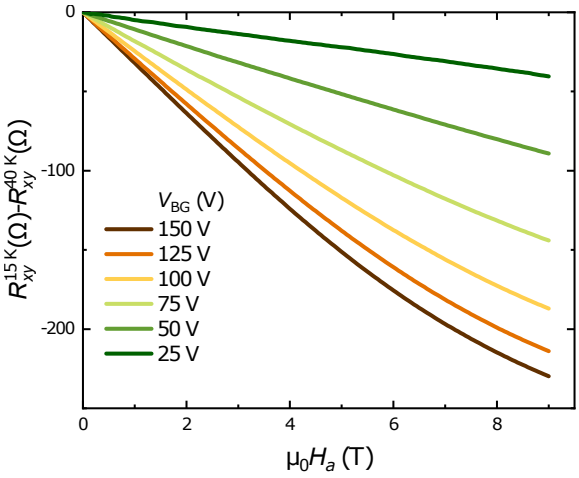

Figure 3.11: The result of subtraction of Hall resistances R_{xy}^{40K} measured at 40 K from curves measured at 15 K, at different gate voltages as indicated.

4

Inhomogeneous superconductivity and quasilinear magnetoresistance in amorphous $LaTiO_3/SrTiO_3$ interfaces

We have studied the transport properties of $LaTiO_3/SrTiO_3$ (LTO/STO) heterostructures. In spite of 2D growth observed in reflection high energy electron diffraction, transmission electron microscopy images revealed that the samples tend to amorphize. Still, we observe that the structures are conducting, and some of them exhibit high conductance and/or superconductivity. We established that conductivity arises mainly on the STO side of the interface, and shows all the signs of the 2-dimensional electron gas usually observed at interfaces between STO and LTO or $LaAlO_3$, including the presence of two electron bands and tunability with a gate voltage. Analysis of magnetoresistance (MR) and superconductivity indicates the presence of spatial fluctuations of the electronic properties in our samples. That can explain the observed quasilinear out-of-plane MR, as well as various features of the in-plane MR and the observed superconductivity.

The pre-print version of this chapter has been published as N. Lebedev, M. Stehno, A. Rana, N. Gauquelin, J. Verbeeck, A. Brinkman, and J. Aarts, *arXiv:2008.03224*, and accepted by Journal of Physics: Condensed Matter. The first two authors contributed equally

4.1. Introduction

Since the discovery of conductivity [2] at the interface between the two nonmagnetic band insulators $LaAlO_3$ (LAO) and $SrTiO_3$ (STO), oxide interfaces have been under intense investigation. The dominant view in the literature on the origin of conductivity at the (001) LAO/STO interface is the so-called polar catastrophe scenario [18, 19], based on the difference between the stacking of neutral layers in STO, but 1-electron-charged layers in LAO. To avoid the discontinuity at the interface, half an electron per unit cell has to transfer from the LAO surface down to interface, leading to a formation of two-dimensional electron liquid (2DEL). Besides that, also La/Sr intermixing [22] and oxygen vacancies formed in the STO [23, 24] can lead to the creation of the conducting layer. Moreover, it was proposed recently that the development of a critical density of oxygen vacancies at the surface of the LAO layer plays a vital role in avoiding polar discontinuity [19, 21].

Along with LAO/STO, also the interface between the antiferromagnetic Mott insulator $LaTiO_3$ (LTO) and STO has been under intensive investigation. LTO is polar along (001) crystal direction, so a charge transfer similar to LAO/STO may be expected. At the LTO/STO interface, the polar discontinuity can be resolved by the variable valence of Ti [163, 164]. Indeed, Biscaras *et al.* [140] argued that conductance at this interface is on the STO side, similar to LAO/STO. On the other hand, Wong *et al.* [162] proposed that the LTO layer is metallic when grown on STO, due to a lattice distortion induced by stress. La/Sr intermixing [157, 165–167], and oxygen and lanthanum off-stoichiometry [168] can also lead to conductivity in LTO.

A recurring problem in the growth of LTO is that it easily suffers from strong overoxidation, both due to migration of oxygen from STO and to oxidation in air of uncapped films[142]. Such overoxidation leads to defective or even amorphous films[142, 155, 224]. Interfaces between STO and amorphous oxides were shown to be conducting due to oxygen vacancies formed on the surface of STO [25, 26, 225], and, similar to the stoichiometric crystalline interfaces[3, 4], the amorphous interfaces are also superconducting[61, 226].

In this chapter, we have studied LTO/STO interfaces grown by Pulsed Laser Deposition (PLD), and found that in spite of layer-by-layer growth signatures, the LTO layer tends to amorphize. Still, the conductivity in the system is basically due to a 2DEL formed on the STO side of the interface. The 2DEL properties are not much different from those of other STO-based oxide interfaces. In particular, Hall data show two-band behavior with standard values for the carrier concentrations and back-gating shows the presence of a Lifshitz point. Less normal is a quasilinear

Magnetoresistance (*MR*), and non-uniform superconductivity. We argue that the possible origin of these phenomena is the non-uniform distribution of oxygen vacancies on the STO surface due to the uncontrolled oxidation process in the LTO layer, which lead to spatial inhomogeneities. This inhomogeneity is clearly seen in the superconducting state, but not easily discernible in the normal state, which is an important part of the message.

4.2. Experimental details

LTO layers were grown by Pulsed Laser Deposition on a TiO_2-terminated surface of STO(001) single crystal substrates. The growth temperature was 750 °C. Growth was in an O_2 atmosphere utilizing two nominal pressures: 1×10^{-4} and 5×10^{-4} mbar. The thickness of the samples was determined by observing the intensity oscillations using Reflection High Energy Electron Diffraction (RHEED) and fixed at 10 u.c. (see Fig. 4.1a). The RHEED pattern showed characteristic stripes indicating 2D growth (Fig. 4.1b,c). Magnetotransport measurements in the range 3-300 K were performed with a physical properties measurement system (a PPMS) from Quantum Design, and below 1 K in an Oxford Instruments Triton dilution refrigerator[1]. Samples were wirebonded with Al wire for magnetotransport measurements, and measured with a standard lock-in technique. Scratches were made on the samples by a diamond knife in the center of each edge to ensure the current path through the sample center, as shown schematically in the inset Fig. 4.1d, together with a denumeration of the contacts. Notwithstanding the observation of RHEED oscillations, results of Scanning Transmission Electron Microscopy (STEM) reveal that the LTO layer in our samples is amorphous (see Fig.4.1f). This is probably due to a relatively high oxygen growth pressure, which, as mentioned, leads to overoxidation and defective or even amorphous films[142, 155, 224]. Indeed we observe a decaying intensity of RHEED oscillations (Fig.4.1a) and cloudiness in the RHEED pattern besides the stripes, which already indicates on some amorphization process. Since the necessary oxygen for overoxidation, at least in part, comes from the substrate, it appears that the amorphisation process takes place during deposition of initially crystalline layers.

Most of the measurements were performed in the van der Pauw (VDP) geometry. To determine the sheet resistance, two resistances were measured, one called R_H with the current applied over one edge (contacts A,B) and the voltage measured along the opposite edge (contacts C,D), and one called R_V using the other pair of

[1]The transport measurements below 1 K were performed by Dr. Martin Stehno at the University of Twente

edges (current through A,D, voltage over B,C). The sheet resistance R_S was then calculated by by solving the VDP equation for R_S by the Newton-Raphson method :

$$e^{-\pi R_V/R_S} + e^{-\pi R_H/R_S} = 1 \tag{4.1}$$

The magnetoresistance was determined in the same way, by either applying in-plane or out-of-plane fields. Hall data were obtained by injecting the current along one diagonal and measure the voltage across the other one, using an out-of-plane field. The out-of-plane magnetotransport data were (anti-)symmetrized. The in-plane data were not. Instead, the two measured voltages in the in-plane geometry were used to obtain *MR* with the current parallel and perpendicular to the current direction. The experimental data obtained at temperatures below 1 K were smoothed to remove noise except for the measurements in magnetic field. The geometry for the measurements of the superconducting transition in the Triton is described in Section 4.4. An extra sample was prepared for study by scanning transmission electron microscope (STEM)[2], using an oxygen pressure of 5×10^{-4} mbar. The conductivity of the LTO layer was checked by using additional gold wires, which were glued by silver paint to the surface of the sample, and resistance was measured by a source meter with an applied current of 1 μA in a two-probe geometry.

4.3. Normal state magnetotransport

4.3.1. The origin of conductance

The different samples have shown a variation in conducting properties. Some exhibit higher conductance and/or superconductivity. We did not observe a correlation between high conductance or superconductivity and the oxygen pressure during growth. The transport data reported here is on a sample which shows high conductivity, a decrease of the sheet resistance upon lowering the temperature (Fig. 4.1d) with a large residual resistivity ratio RRR = $R_S(300K)/R_S(10K) = 261$, and superconductivity below 300 mK. This sample has been grown at 5×10^{-4} mbar akin to the sample used for the STEM study.

As mentioned above, the conductance in these heterostructures can arise not

[2]The STEM experiments were performed by Dr. Nicolas Gauquelin at the University of Antwerp

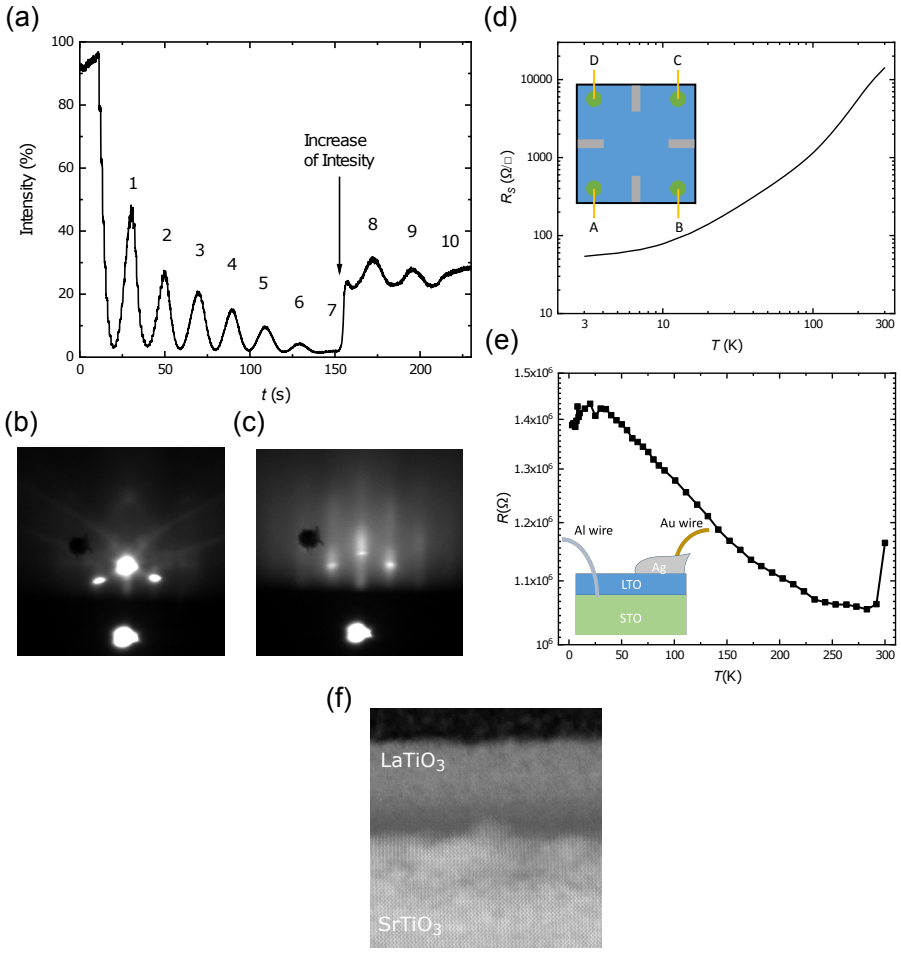

Figure 4.1: (a) RHEED intensity monitoring during grown 10 u.c. of LTO. RHEED patterns (b) before and (c) after deposition. (d) Temperature dependence of Sheet resistance. Insert: Sketch of van der Pauw measurements. (e) Temperature dependence of the two-probe measured resistance of the LTO layer. Schematics of two-probe measurement is shown on the insert. (f) STEM scan of the LTO/STO interface.

only from a 2DEL forming at the LTO/STO interface but also in the LTO itself. To distinguish between these two possibilities, after performing the transport measurements presented below, we investigated the conductivity of the LTO layer in the following manner. A Au wire was glued by the silver paint to the LTO surface as is shown schematically in the inset in Fig. 4.1e. Resistance measurements as function of temperature between the Al wire contact and the Au wire contact, shown in Fig. 4.1e, demonstrated that although the LTO layer is slightly conducting, it exhibits insulating behavior going to lower temperatures. That conductance could arise due to the formation of pinholes in the LTO film under the surface of silver paint [227]. Moreover, results of Scanning Transmission Electron Microscopy (STEM) (see Fig. 4.1f) reveal that the LTO layer in our samples is amorphous, in agreement with the results of Scheiderer *et al.* [142]. Because the LTO layer is (almost) insulating and amorphous, we conclude that the conductivity in our samples arise from oxygen vacancies on the surface of STO similar to the previously reported conducting interfaces between amorphous oxide and STO [25, 26, 225]. This can explain the high RRR but also the variation of conducting properties observed from sample to sample.

4.3.2. Magnetotransport without back gate

Broadly speaking, the magnetotransport properties are similar to previously reported results on oxide heterostructures. In particular the Hall resistance becomes non-linear below 100 K, marking the appearance of two-band behavior, with two types of carriers: of high concentration and low mobility, and vice versa. The Hall data and details of the Hall analysis are given in the Appendix 4.7.1, extracted carrier concentrations and mobilities in Fig. 4.2a-b. The out of plane MR is anomalous. It is almost flat at high temperatures, and in low fields gradually becomes parabolic with lower temperature. So far, such behaviour is similar to most of the results on STO-based interfaces. However, below 70 K, a quasilinear MR in high fields starts to develop (Fig. 4.2c), with values much higher than reported previously in LTO/STO [207]. To describe this behavior, we fitted the MR in the field range form 5 T to 9 T with the following equation:

$$MR = A + \beta B^{\gamma}, \tag{4.2}$$

where A, β, γ are fitting parameters. The results of the fit are shown in Fig. 4.2f. At high temperature where the MR is small, the parameters A and β are almost zero. At low temperatures, γ is smaller than 2, indicating that linear contribution to MR becomes dominant. Note that for this analysis, we limited the lowest boundary for γ to 1 in order to avoid unphysical behaviour of A.

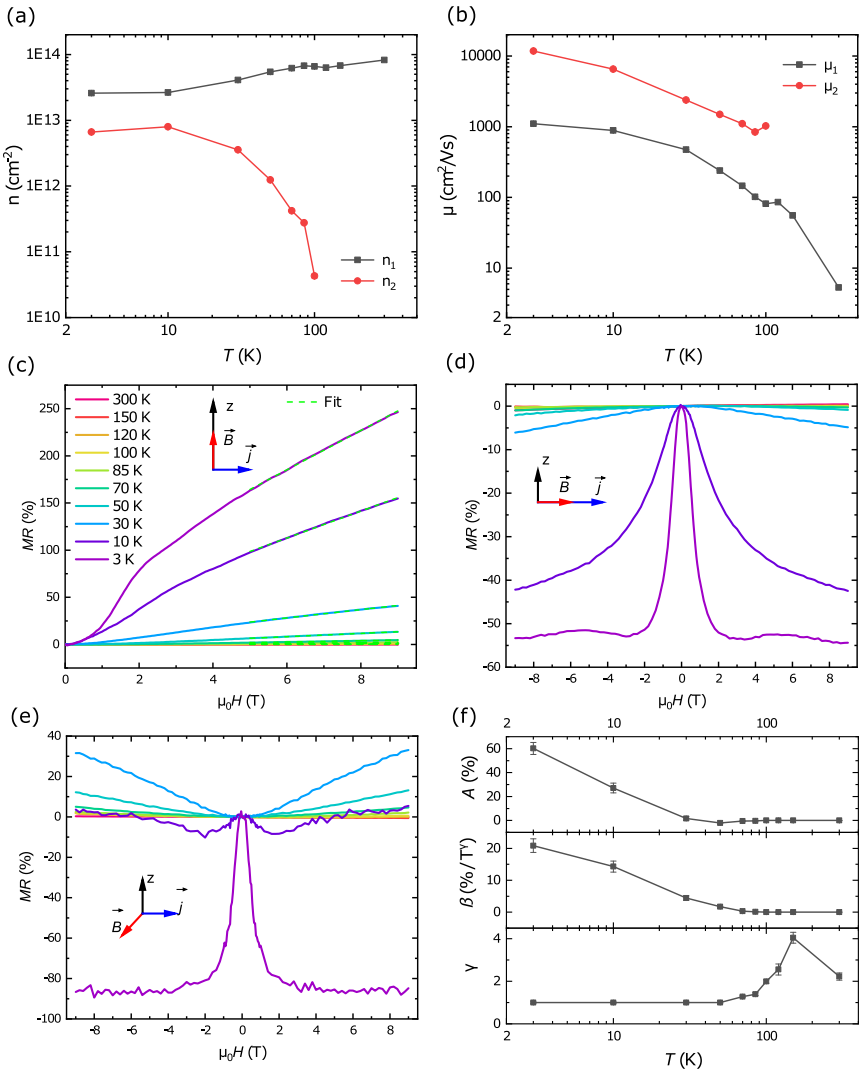

Figure 4.2: (a) Carrier concentration and (b) mobility versus temperature obtained from a two-band analysis of Hall resistance measurements (given in the Appendix 4.7.2). (c-e) The magnetoresistance *MR* with magnetic field oriented (c) perpendicular to the sample plane, (d) in-plane parallel to the current direction, and (e) in-plane perpendicular to the current direction. (f) Temperature dependence of the parameters to describe the non-linear out-of-plane *MR* by fitting Eq. 4.2.

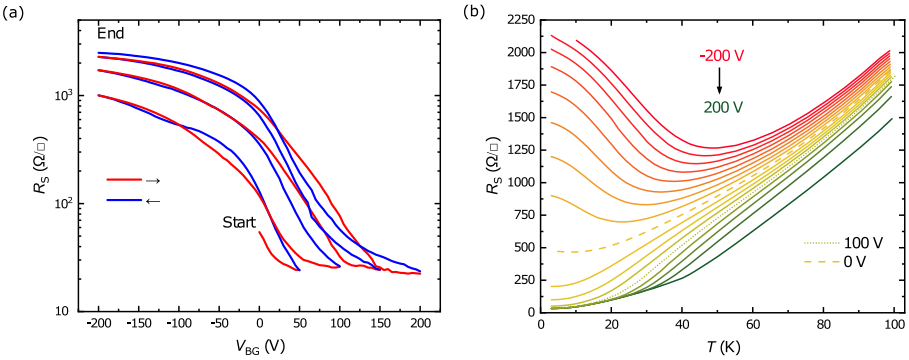

Figure 4.3: (a) Dependence of the sheet resistance R_S on the back gate voltage. (b) Temperature dependence of R_S for gate voltages from 200 to −200 V with steps of 25 V.

The in-plane *MR* is negligible at high temperatures (Fig. 4.2d,e). At low temperatures, the parallel-to-current configuration shows a negative *MR*, which increases at temperatures below 30 K and undergoes a transition from parabolic to bell shape. The perpendicular-to-current configuration exhibits first an increase of the positive *MR* down to 70 K, shows the onset of negatives lobes below 30 K and finally transforms also to a bell shape with saturation at 3 K. Note that the VDP configuration does not allow to reliably exclude contributions to the *MR* of currents perpendicular to the magnetic field in the parallel in-plane geometry and currents parallel to the field in the perpendicular in-plane geometry.

4.3.3. The effect of gating on the sheet resistance

To further study the magnetotransport properties, we applied a back gate voltage V_{BG} to the sample. First we investigate the effect of a gate voltage on R_S. The "training" of the sample at 3 K, meaning successive up-down sweeps of the voltage, (Fig. 4.3a) showed an increase of R_S in the backsweeps, which is usually explained as the trapping of charges escaping from the quantum well [54, 55]. We observe some hysteric effects between the up sweep and the subsequent down sweep which are not always present; moreover, we do not find the interface to become insulating in the backsweep at low or negative V_{BG}. This was found for highly conducting (crystalline) interfaces [4, 208], but not for less conducting ones [54, 55]. Fig. 4.3b shows the temperature dependence of R_S, measured from 200 V down to -200 V. Coming from negative V_{BG}, the R_S shows an upturn to low temperatures which disappears at 0 V. Also, the change in R_S at low temperatures is largest between 0 V and 100 V, similar to what is seen in the training sweeps shown in

Fig. 4.3a. We will come back to this behavior in the discussion.

4.3.4. The effect of gating on the magnetotransport

Starting again with the Hall resistance, we find it becomes nonlinear between −25 and 0 V (Appendix Fig. 4.8b), signaling the well-known Lifshitz transition [36, 37]. The gate dependence of the carrier concentrations and mobilities, found after standard analysis, is given in Fig. 4.4a,b. In the proximity of the transition, between −20 and 40 V, the two-band model gives an anomalous increase of carrier concentration and a dip in the mobility of the majority carriers, with high error bars. This is the case at 3 K, as well as at 0.5 K, with the measurements performed in a different cryostat. This anomaly probably arises due to a fast decrease in the second type of carriers, which the fit is not able to correctly describe; and to the fact that the mobility values in this regime are close, which complicates the fitting procedure. To avoid such problems, we limited the lowest possible mobility value of majority carriers in this region by the value extracted from one band analysis at the closest point to the transition. Such a limit resulted in a plateau of the mobility of majority carriers versus V_{BG} near the Lifshitz transition. Note also that the carrier concentrations of the two bands become almost equal above 100 V.

Turning to the *MR* at 3 K, the out-of-plane *MR*, shown in Fig. 4.4c (See Appendix Fig. 4.8a for a zoom-in around low fields and *MR* values), is small and negative in high fields at high negative gate voltages. In this range of V_{BG}, the parameters A and β are almost zero (Fig. 4.4f), and Eq. 4.2 is not always adequate to describe the high field *MR*; also γ shows inconsistent behavior. However, with an increase of the gate voltage, *MR* becomes positive, and above 50 V, the quasilinear *MR* at 3 K (Fig. 4.4c) starts to develop with the value of γ about 1 (Fig. 4.4f). At 0.5 K, Eq. 4.2 gives poorer fit with higher error bars and less clear gate dependence. That can be due to more noise in the data obtained in our low temperature cryostat due to low current used and smaller available field range ($[-8T, 8T]$). However, if we fix $\gamma = 1$ starting from 70 V, then the fit results are consistent (purple curves in Fig. 4.4f). Linear high field *MR* has been seen before in STO-based heterostructures [36, 47, 228].

The in-plane *MR* parallel to the current shows a transition from positive to negative at 0 V, whereas the in-plane *MR* perpendicular to the current stays negative (Fig. 4.4d,e and Appendix Fig. 4.8c,d). Above 0 V, both in-plane configurations showed substantial enhancement of the negative *MR* and developed the bell shape field dependence (Fig. 4.4d,e). They exhibit saturation in high fields above 100 V, and the amplitude starts to decrease, especially in the configuration field parallel to the current.

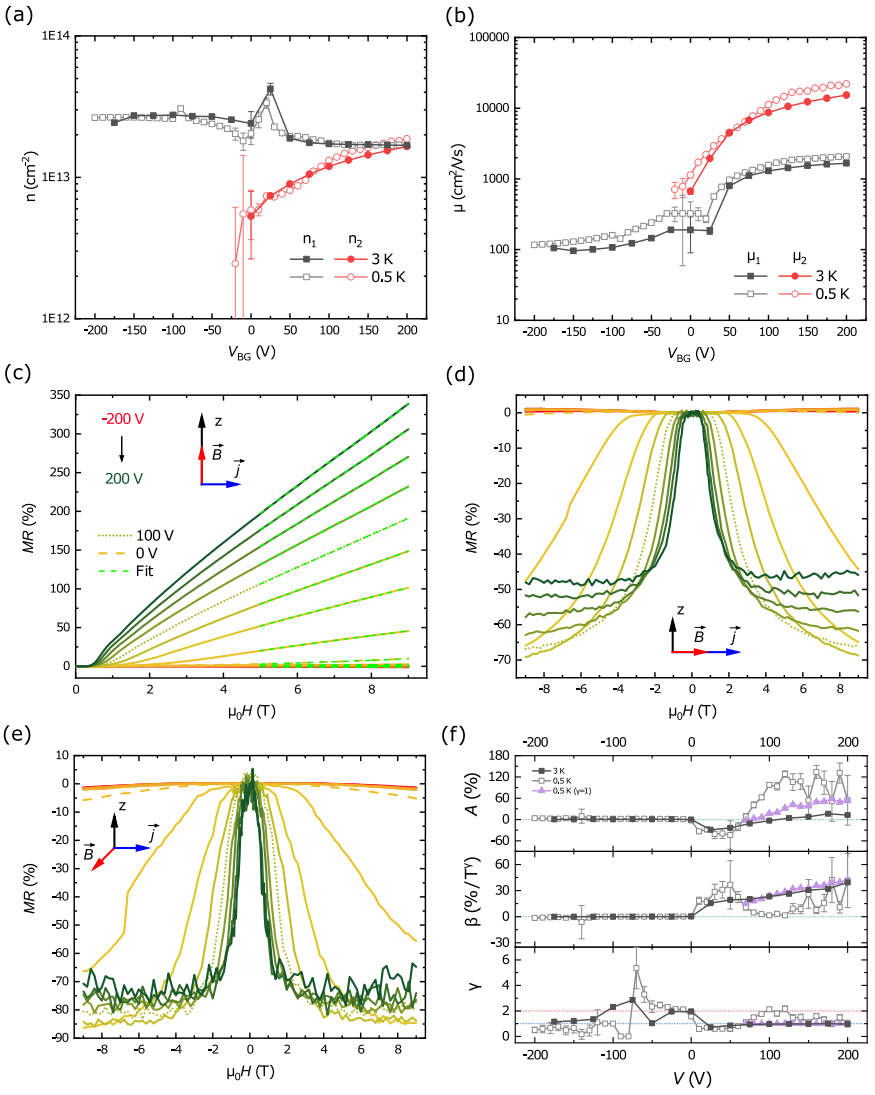

Figure 4.4: (a) Carrier concentration and (b) mobility versus gate voltage at the temperatures 3 K and 0.5 K as indicated, obtained from a two-band analysis of Hall resistance measurements. (c-e) The magnetoresistance *MR* at 3 K with magnetic field oriented (c) perpendicular to the sample plane, (d) in-plane parallel to the current direction, and (e) in-plane perpendicular to the current direction. Note that −200 V is not shown for out-of-plane magnetic field measurements. (f) Temperature dependence of the parameters to describe the non-linear out-of-plane *MR* by fitting Eq. 4.2. Note that near transition from negative to positive high field *MR* in the range [−110, −80] parameter γ and, for some values, β were fixed.

Summarizing this part, the normal state properties show all the characteristics of the oxide 2DEL, with a high conductance due to a high carrier concentration, and a Lifshitz point around zero gate voltage. The *MR* is clearly sensitive to the Lifshitz point and in particular in the out-of-plane configuration shows quasi-linear behavior which needs to be discussed.

4.4. Electronic transport in the superconducting state

We studied the superconducting properties of the sample in the VDP geometry, using either the 'horizontal' or the 'vertical' sides, and for the whole range of gate voltages V_{BG}. We also measured in a two-probe configuration (current and voltage contacts on the same side). Those data are given in the Appendix, Fig. 4.9. We find dissimilar behavior in the two VDP measurements, so we did not calculate a sheet resistance R_S by solving the VDP equation. Instead, we multiplied the measured resistance by the VDP constant $c_{VDP} = \frac{\pi}{\ln 2}$. In Fig. 4.5, we represent the data in two different ways. Fig. 4.5c,d show $R_S(T)$ for gate voltage between -200 V and 200 V. Fig. 4.5e,f shows R_S in a colorscale, as function of V_{BG} and T. In the vertical configuration, the resistive transition is more or less monotonous, as can be expected. T_c increases when V_{BG} is increased from -200 V, reaches a maximum around 0 V, and then decrease again. At the same time, R_S decreases continuously. The behavior of T_c at high V_{BG} can therefore be better followed in the colorscale plot, where it is shown as a dashed line marking a 50% drop from the resistance at 600 mK. In the horizontal configuration, the resistance around T_c is non-monotonous. For all V_{BG}, the resistance first rises before going down to 0. Comparing the color plots, both measurements show a dome shaped T_c behavior similar to reported previously [4, 36], with a maximum around 0 V, but the maximum T_c is much lower in the horizontal configuration.

Anisotropy in STO-based structures has been reported before [59, 226]. It can arise, for instance, due to the formation of regions with different conducting properties, which strongly affects measurements in the VDP geometry. In a recent report on the effect of STO domain walls on the normal state resistance of mesoscopic LAO/STO devices, the authors of [229] proposed a scenario where a high resistance region develops in the center of the sample in order to explain the anisotropic behavior they observed. In our case, the behaviour of $R(T)$ dependencies above 0.3 K does not differ significantly for both geometries, although some variation of the resistance is present. In the transition, however, the sample may well become inhomogeneous. The two-probe resistance behavior

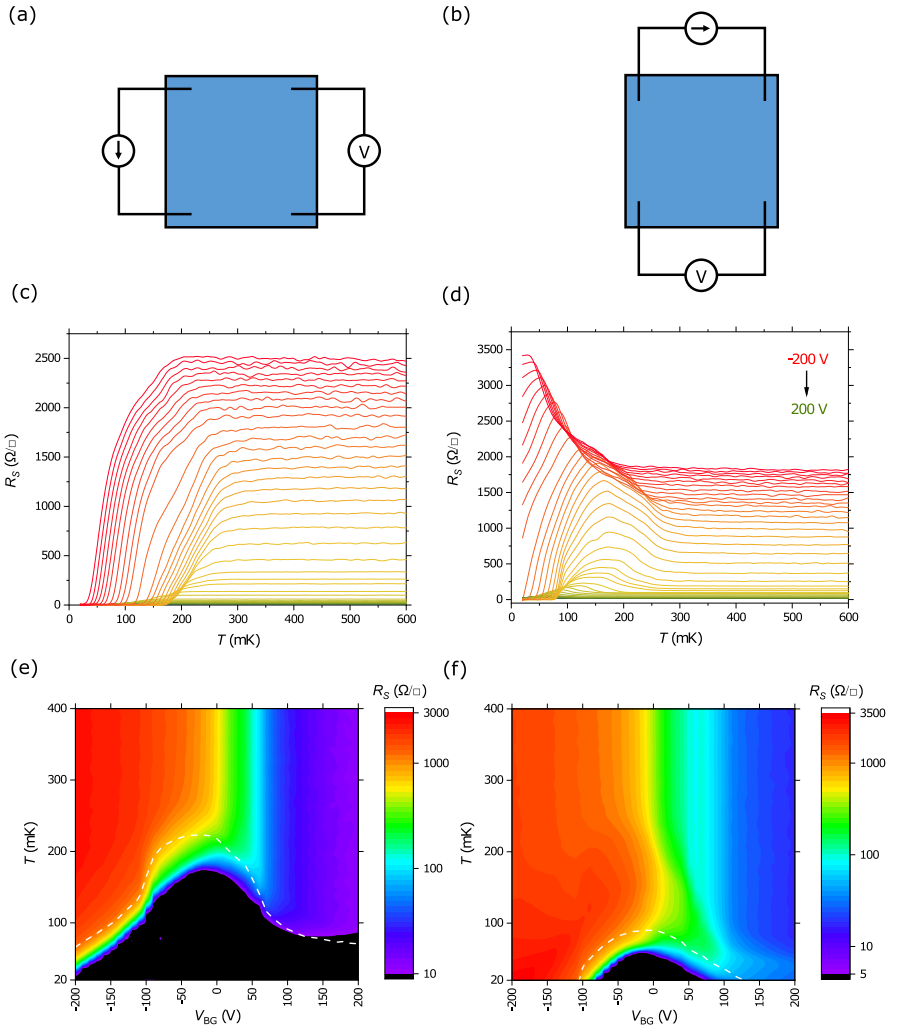

Figure 4.5: Behavior of the sheet resistance R_S as function of temperature T and back gate voltage V_{BG} for two van der Pauw contact geometries called (a) 'vertical' and (b) 'horizontal'. $R(T)$ curves at different gate voltage with step of 10 V for (c) vertical and (d) horizontal configurations. The same data visualized in colour map form for (e) vertical and (f) horizontal configurations.

in the Appendix 4.7.3 shows indications of a percolative transition, and features we observe can be understood using a resistor model for an inhomogeneous superconductor adapted from Ref. [230]. The original model was precisely used to explain the peak in $R_S(T)$ for films measured in the VDP geometry [230]. A sketch of the equivalent electric circuit for the modified model, where all resistances have different transition temperatures, is shown in Fig. 4.6b. The sample corners in Fig. 4.5a-b and 4.9a-b are designated as in the insert of Fig. 4.1d. The algorithm to solve the equations is described in the Appendix 4.7.4.

The normalized resistances at 0 V for the different measurement configurations, including the 2-probe measurements, are plotted in Fig. 4.6a. They can be divided into five regions. In region I, the temperature is above T_c for all percolation paths, and all resistances are in the normal state. R^{ver}_{VDP} decreases in region II and becomes zero in region III, while R^{hor}_{VDP} reduces to zero in region III. In region IV, both two probe resistances become equal to each other and reach zero at the start of region V. Of course, multiple combinations of transition temperatures of R_i can yield this behavior. The temperature dependencies of R_i that lead to a very good fit of the data are shown in Fig. 4.6c. The fits themselves are shown in Fig. 4.6d. The table 4.1 with fit parameters is included in the the Appendix 4.7.4.

In region II, R_2 goes to zero and, therefore, R^{ver}_{VDP} goes to zero too. Also, the denominator decreases faster than the numerator in Eq. S6 and consequently, R^{hor}_{VDP} now increases. The opposite trend is observed for R^{hor}_{2probe}, whereas R^{ver}_{2probe} changes insignificantly. In region III, R_5 and R_7 reduce to zero, and thereby R^{hor}_{VDP} reduces to zero. In region IV, $R_2 = 0$, $R_5 = 0$ and $R_7 = 0$, as well as the measured resistances R^{hor}_{VDP} and R^{ver}_{VDP}, and therefore R^{hor}_{2probe} and R^{ver}_{2probe} become equal:

$$R^{hor}_{2probe} = R^{ver}_{2probe} = \frac{R_1 R_3 R_4 R_6 R_8}{R_1 R_6 (R_3 R_4 + R_3 R_8 + R_4 R_8)}, \tag{4.3}$$

The resistances R_1 and R_6, occurring as a product in both numerator and denominator, have to remain finite in the measured range, for Eq. 4.3 to be determinate. In region V, one of resistances R_3, R_4 or R_8 is zero because the resistances in the two-probe are zero. In our case, it is R_8, whereas R_1, R_3, R_4, and R_6 are assumed not to undergo a superconducting transition in the measured range of temperatures to stabilize the fit.

The behavior on both sides of the resistance dome around zero gate voltage, for our different measurement configurations, can be understood from this model, assuming the T_c's of all percolation paths on both sides of the dome are suppressed by the gate voltage. For the VDP vertical configuration, because R_2 has the higher

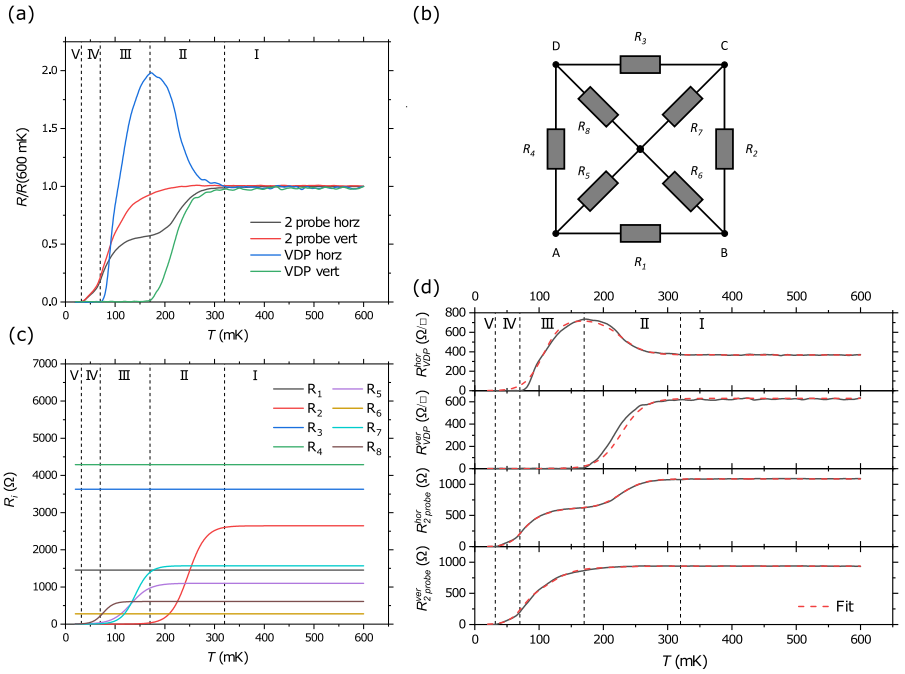

Figure 4.6: (a) The temperature dependent resistance for the different measurement configurations at 0 V, normalized to the normal state value just above the transition. (b) Temperature dependence of the different model resistors R_i (see text). (c) Resistance in different measured configurations and fit using Eq. 4.9-4.14.

T_c, the resistance stays zero in the whole range of gate voltages. In the other configurations, since R_5, R_7 and R_8 stay finite, T_c is (more) quickly suppressed, both in the VDP horizontal and in the two-probe configurations.

The proposed model also provides insight into the large critical currents observed in our sample, shown in Appendix Fig. 4.10g,h. The percolation paths for critical currents corresponding to R_2, R_5 and R_7 have higher T_c. Therefore, a much higher induced current is required to drive those regions, which constitute the percolation paths, to the normal state in VDP configuration. T_c of the percolation path corresponding to R_8 is smaller, and a lower current to drive it in the resistive state is required in two-probe configuration.

4.5. Discussion

Results of the back gate experiments on our a-LTO/STO samples can be easily separated in three regions: i) negative gate voltages, ii) voltages between -20 V and +75 V, and iii) above +75 V. In the first region, transport is is governed by a one-band regime. Note that we do not observe an insulating state in the negative gate voltage range. This can be a sign of nonuniform conductivity. The behavior under voltage sweeps in the positive quadrant is another. We are apparently not able to fully trap the carriers and induce an insulating state as can occur in (crystalline) LAO/STO and LTO/STO interfaces [54, 55]. Instead, we suggest that due to a significant non-uniformity of conducting properties, the trapping of electrons, which is seen in the hysteretic behavior, rearranges the current flow in the sample.

In the second regime the transport has changed to two band behavior. In this region, the *MR* exhibits the enhancement of out-of-plane and in-plane *MR* in agreement with previous works. Anisotropic in-plane *MR* has been reported in LAO/STO heterostructures [65, 97, 231]. This behavior has been attributed to the magnetic ordering [97, 231]. Simultaneously, our observation of a bell shape of the in-plane *MR* at different gate voltage is similar to the results obtained by Diez *et al.* [98]. They argued (see also Ref. [222]) that the decease in resistance, observed when the field is applied parallel to the plane and perpendicular to the current, can be described by a single particle Boltzmann equation. They showed that, when the second band is occupied, both interband scattering and spin-orbit coupling (SOC) are enhanced, which leads to the observed large negative in-plane *MR*. The *MR* is strongly modified in the gate region with the strongest SOC tunability, which would correspond to the region between 0 V and 75 V in our data. However, we also see an unexpected enhancement in the geometry with current parallel to

the field. We cannot exclude contribution of currents perpendicular to the field in this geometry, as mentioned in Sec. 4.3.2, but another contribution may well arise from (spatial) mobility and carrier density fluctuations in our sample. In this region, T_c and I_c of superconducting state reach their maximum.

The high positive gate voltage range above 75 V is the range where the positive quasilinear *MR* develops which we believe is another signature of inhomogeneous transport in our films. In fact, such a crossover is observed in various different systems where spatial inhomogeneities can be invoked [232–236]. Generally, to observe the crossover at low fields requires relatively high mobilities. In our system these are available through high mobility carriers above the Lifshitz point.

Earlier, Ref. [65] argued that the large positive *MR* supports an electronic phase separation scenario. However, there is a significant difference for our films compared to the ones studied in Ref. [65, 231]. Our system does not (for gate voltages of 0 V and above) exhibit an upturn of sheet resistance at low temperatures. Even more below 30 K, the *MR* for field-perpendicular-current is always negative. The main reason for this is that the results reported in Ref. [65] were on crystalline LAO/STO samples grown at the high pressure of 10^{-2} mbar O_2. Lower pressures leads to a decrease in the maximum magnetization according to results of Ref. [65], thus, making scenario of the phase separation between normal and magnetic region implausible as the main driving mechanism for the observed quasilinear *MR*.

At higher carrier densities (above 75 V), the in-plane *MR* showed a decrease, indicating an additional contribution which saturates in high fields. A connection between a non-trivial negative in-plane *MR* and a linear out-of-plane *MR* was actually observed in work on thin films of the Dirac semimetal Cd_3As_2 [237], and in electron doped GaAs quantum wells [238]. In both cases, the macroscopic disorder is argued to be the origin of such behavior of *MR*. Additional support for this scenario in our samples is that the quasilinear *MR* develops in the region where high and low-mobility carriers have very similar carrier concentration as shown in Fig. 4.4a, and even appear to cross. So far, such crossing in STO-heterostructures has been only observed in experiments with top gate [37]. In Cd_3As_2 an increase of negative *MR* was observed in the temperature range where two electron-type carriers have a crossover. However, in our case, a negative *MR* in current-perpendicular-field is also expected to arise from SOC effects and inter-band scattering. Spatial fluctuations in the conductivity can result in the current paths perpendicular to the magnetic field in in-plane geometry with the current parallel to the field [234, 237]. Together with the imperfection of the geometry used in the sample, it can lead to the non-trivial *MR* for this configuration. Finally, also, the low temperature data point to the development of regions that do not

become superconducting above 100 V and again indicate spatial fluctuations of conductivity.

Coming back to the superconductivity, extensive research already indicated the existence of inhomogeneous superconductivity in STO-based oxide heterostructures [61, 62, 169, 239–241]. As we discussed the behaviour of both $R(T)$ and $I(V)$ in our sample indicates the presence of strong spatial variations. The simple model we use to describe the inhomogeneous superconductor [230] can describe some of the main features of the superconducting transition and critical current behaviour in our samples, although it is obviously too simple to be able to explain all the details of the real system, and in particular features arising due to a weak coupling between regions.

The final point to discuss is the possible origin of inhomogeneous electronic structure of the interface. This is the more important since it is often assumed that amorphous layers per se need not yield significantly different physics than crystalline layers. Previously, inhomogeneities in the conductance have been shown to arise from ferroelastic domains [66–69, 242], which strongly affect superconducting properties [67, 243]. At the same time, as was mentioned, the quasilinear *MR* in our samples is much higher than in the crystalline LAO/STO system, indicating an additional significant source of inhomogeneities. A prime candidate is (oxygen) stoichiometry variations, most likely created during the growth. The amorphicity of the LTO layer itself may be an issue, but also the process of amorphization of LTO is not controlled in our samples, which can in particular be seen from the fact that RHEED oscillations were observed during growth. With respect to the amorphicity, it is instructive to note that also the deposition of amorphous LAO on STO led to a superconducting state which was described as a random array of Josephson-coupled superconducting domains [61].

4.6. Conclusions

We have grown and studied heterostructures of $LaTiO_3/SrTiO_3$. In spite of clear two-dimensional growth, our samples were found to be amorphous, which may be due to the absence of a capping layer. The samples showed the salient characteristics of the electron gas at oxide interfaces, in particular two-band behavior with normal values for the carrier concentrations and mobilities, as well as the existence of a Lifshitz point upon applying a gate voltage. The conductance was found to be

high and inhomogeneous, signaled in particular by a large quasilinear *MR* and a percolative superconducting transition. By measuring in different configurations, both van der Pauw and two-probe, and using a simple model for a non-uniform superconductor [230], we were able explain prominent features of the superconducting transition in our sample. We propose that the non-uniformities arise from oxygen stoichiometry variations in our samples.

4.7. Appendix

4.7.1. Analysis of carrier concentrations and mobilities

To extract carrier concentration and mobility, we used the following equation in the two-band region:

$$R_{xy}(B) = -\frac{B}{e}\frac{n_1\mu_1^2 + n_2\mu_2^2 + (n_1+n_2)\mu_1^2\mu_2^2B^2}{(n_1\mu_1 + n_2\mu_2)^2 + (n_1+n_2)^2\mu_1^2\mu_2^2B^2}, \tag{4.4}$$

where e is the elementary charge, n_i and μ_i are carrier concentration and mobility of i type carriers correspondingly. For fitting the constraint $R_S(0) = 1/e(n_1\mu_1 + n_2\mu_2)$ was used. In the one-band region, we used high field Hall resistance value and zero field sheet resistance.

4.7.2. Magnetotransport properties

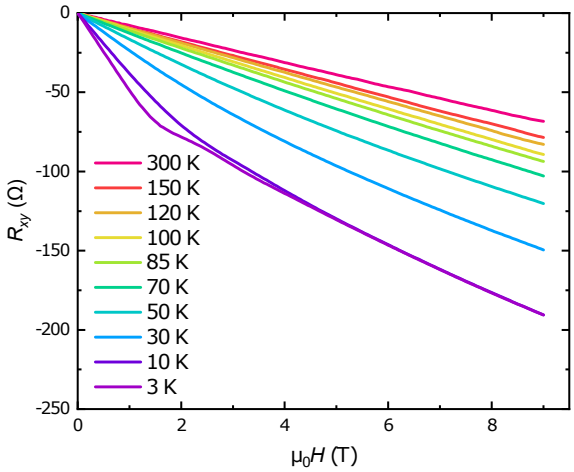

Figure 4.7: Hall resistance at different temperatures.

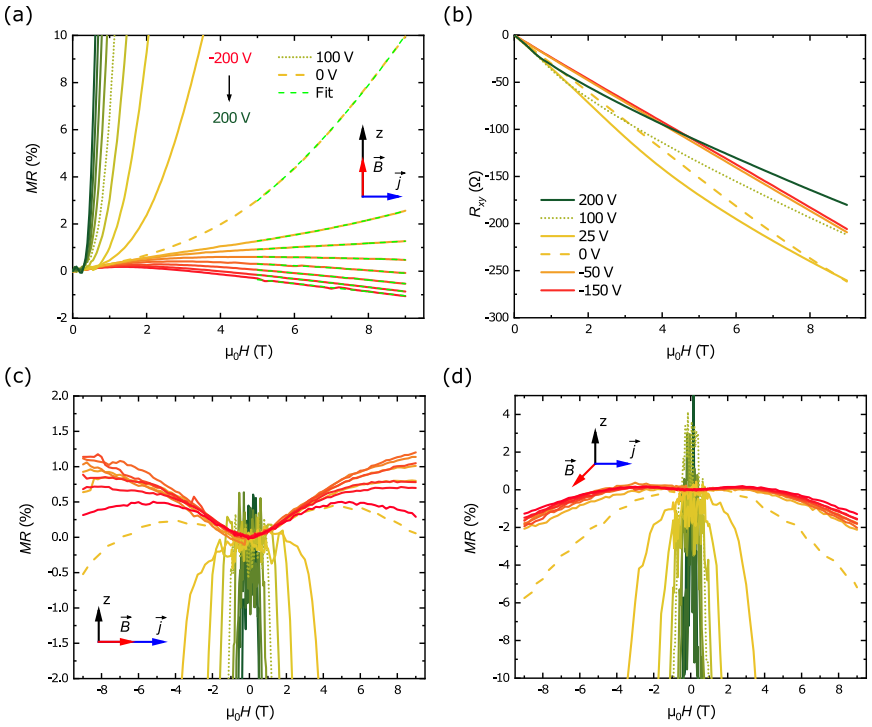

Figure 4.8: (a) A zoomed-in part of the *MR* at 3 K with the magnetic field perpendicular to the sample plane. (b) Hall resistance at 3 K for selected gate voltage values. (c) A zoomed-in part of the *MR* at 3 K with the magnetic field in-plane and parallel to the current direction and (d) in-plane perpendicular to the current direction.

4.7.3. Superconducting properties

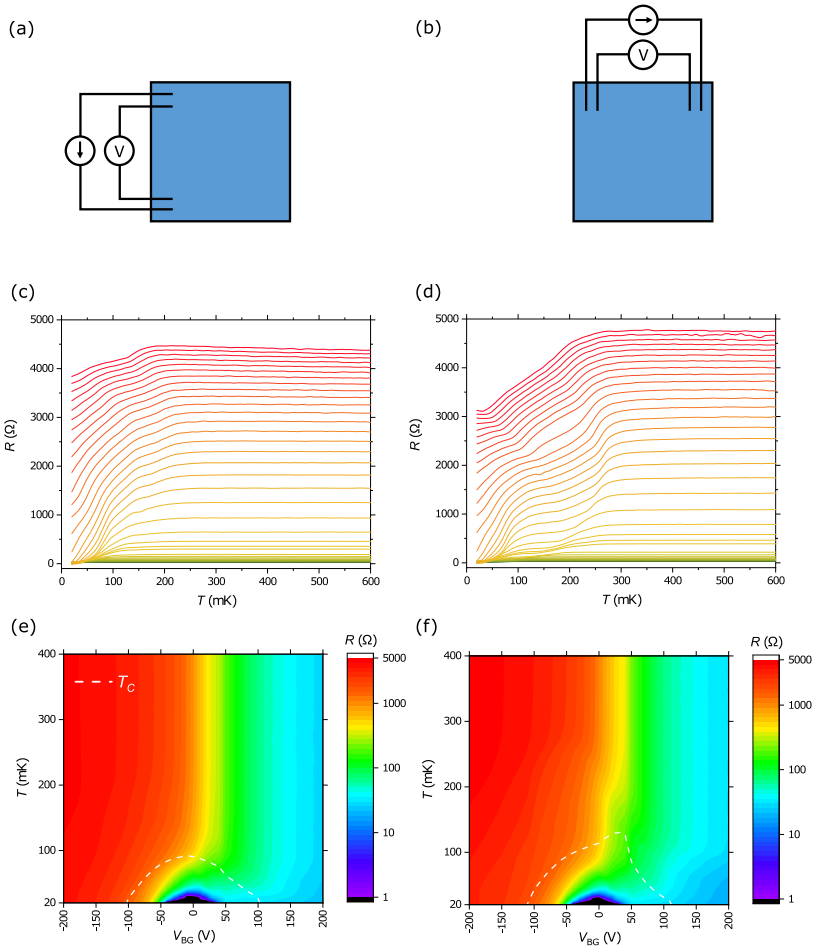

Figure 4.9: Behavior of the resistance as function of temperature T and back gate voltage V_{BG} for two two-probe contact geometries called (a) 'vertical' and (b) 'horizontal'. $R(T)$ curves at different gate voltage with step of 10 V for (c) vertical and (d) horizontal configurations. The same data visualized in colour map form for (e) vertical and (f) horizontal configurations.

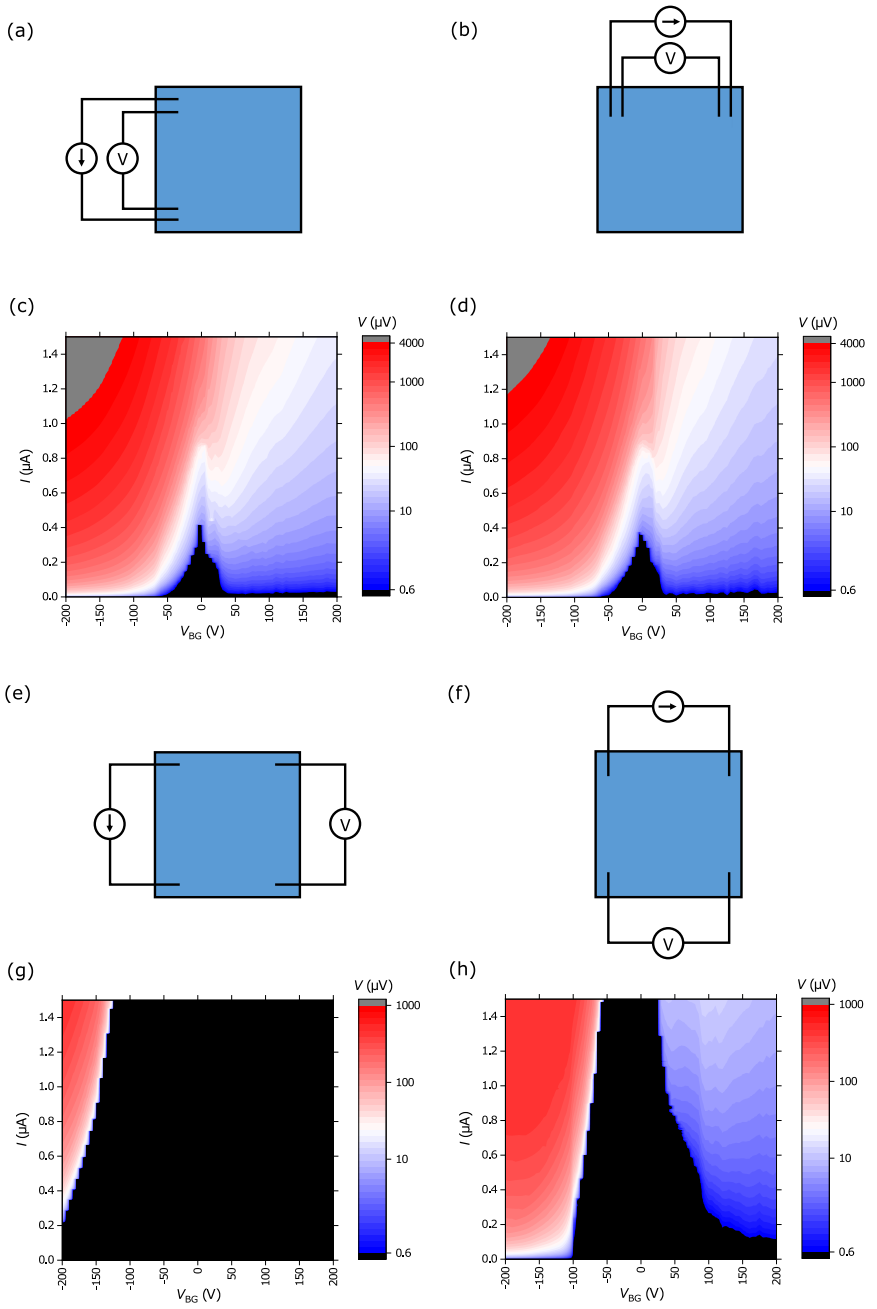

Figure 4.10: (a)-(b) and (e)-(f) Schematics of measurements geometry. (c)-(d) and (g)-(h) $I(V)$ curves at the different gate voltages at 20 mK.

4.7.4. Circuit analysis

The measured resistances can be expressed through a set of resistances of the model in the following way. First, using a Y-Δ network transform, it is possible to simplify the model circuit into two simple ones for the vertical and horizontal direction. The circuits obtained in this way are shown in Fig. 4.11. The newly introduced set of resistances are expressed as:

$$R_A = \frac{R_1 R_5}{R_1+R_5+R_6}, R_B = \frac{R_1 R_6}{R_1+R_5+R_6}, R_C = \frac{R_5 R_6}{R_1+R_5+R_6}, \tag{4.5}$$

$$R_D = \frac{R_7 R_8}{R_3+R_7+R_8}, R_E = \frac{R_3 R_8}{R_3+R_7+R_8}, R_F = \frac{R_3 R_7}{R_3+R_7+R_8}, \tag{4.6}$$

$$R_G = \frac{R_4 R_5}{R_4+R_5+R_8}, R_H = \frac{R_4 R_8}{R_4+R_5+R_8}, R_I = \frac{R_5 R_8}{R_4+R_5+R_8}, \tag{4.7}$$

$$R_J = \frac{R_6 R_7}{R_2+R_6+R_7}, R_K = \frac{R_2 R_7}{R_2+R_6+R_7}, R_L = \frac{R_2 R_6}{R_2+R_6+R_7}, \tag{4.8}$$

These circuits can be solved by the mesh current method. After some lengthy but straightforward arithmetic calculations, the resistances in the different measurement configurations can be expressed as follow:

$$R^{hor}_{VDP} = \frac{\pi}{\ln 2} R_{CD,BA} = \frac{\pi}{\ln 2}\frac{V_{BA}}{I_{CD}} = \frac{\pi}{\ln 2}\frac{R_1 R_3 (R_2 R_5 R_8 + R_4 R_6 R_7 + Y)}{Z}, \tag{4.9}$$

$$R^{ver}_{VDP} = \frac{\pi}{\ln 2} R_{AD,BC} = \frac{\pi}{\ln 2}\frac{V_{BC}}{I_{AD}} = \frac{\pi}{\ln 2}\frac{R_2 R_4 (R_1 R_7 R_8 + R_3 R_5 R_6 + Y)}{Z}, \tag{4.10}$$

$$R^{hor}_{2probe} = R_{CD,CD} = \frac{V_{CD}}{I_{CD}} = \frac{R_3(U + (R_1+R_2+R_4)Y + R_4 W + X)}{Z} \tag{4.11}$$

$$R^{ver}_{2probe} = R_{AD,AD} = \frac{V_{AD}}{I_{AD}} = \frac{R_4(V + (R_1+R_2+R_3)Y + R_3 W + X)}{Z}, \tag{4.12}$$

$$\begin{aligned} W &= R_8(R_2(R_1+R_5+R_6) + R_1(R_6+R_7)), \\ X &= R_1 R_2 (R_5 R_7 + R_8(R_5+R_7)), \\ Y &= R_5 R_7 (R_6+R_8) + R_6 R_8 (R_5+R_7), \\ U &= R_4 R_7 (R_2(R_1+R_5+R_6) + R_1 R_6), \\ V &= R_3 R_5 (R_1(R_2+R_6+R_7) + R_2 R_6), \\ Z &= (R_1+R_2+R_3+R_4)Y + X + (R_3+R_4)W + U + V + \\ &\quad R_3 R_4((R_1+R_5+R_6)(R_2+R_7) + R_6(R_1+R_5)), \end{aligned} \tag{4.13}$$

where $V_{ij} = V_i - V_j$, and I_{ij} is the current injected in contact i and taken out from contact j. R_i is assumed to follow a simple stepwise function for an inhomogeneous phase transition [244]:

$$R_i = \frac{R_{norm_i}}{(1+e^{(T_{c_i}-T)/w_i})}, \tag{4.14}$$

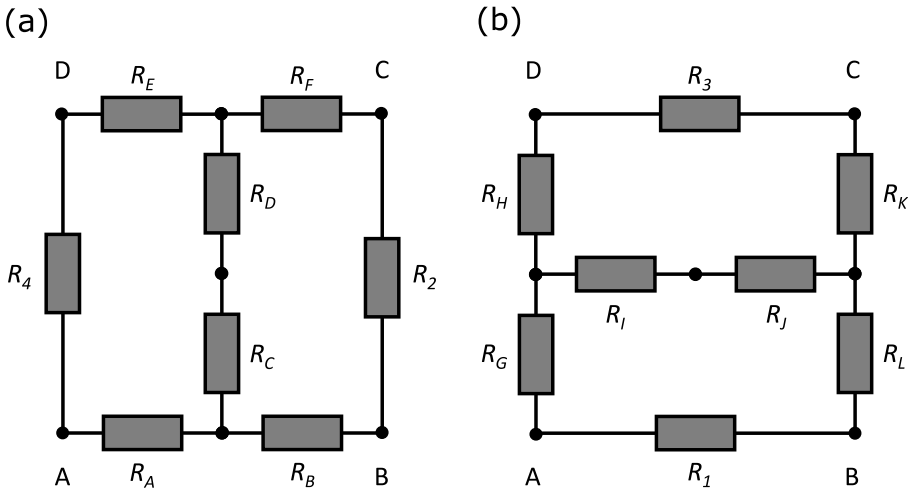

Figure 4.11: (a) An alternative representation of the model circuit from the main text for (a) vertical and (b) horizontal configurations.

where R_{norm_i} is resistance in normal state, T_{c_i} is the critical temperature, which corresponds to the resistance with $R_{norm_i}/2$ and w_i determines the broadening of the superconducting transition. The result of the fitting is present in Table 4.1. Note that parameters have been limited according to the picture described in the main text, and some of them have been fixed in such a way that the resistance stays constant in the measured range.

R_i	R_{norm} (Ω)	T_i (K)	w_i (K)
R_1[a]	1453.3 ± 310.7	0.001	0.0001
R_2	2644.8 ± 813.3	0.247 ± 0.005	0.0178 ± 0.0002
R_3[1]	3626.8 ± 623.2	0.001	0.0001
R_4[1]	4289.0 ± 1377.5	0.001	0.0001
R_5	1098.4 ± 360.9	0.13 ± 0.005	0.019 ± 0.0003
R_6[1]	277.3 ± 7.1	0.001	0.0001
R_7	1569.3 ± 497.0	0.14 ± 0.003	0.014 ± 0.0003
R_8	608.4 ± 16.8	0.08 ± 0.0004	0.01 ± 0.0001

Table 4.1: The parameters obtained from fits of R^{horz}_{VDP}, R^{vert}_{VDP}, R^{horz}_{2probe} and R^{vert}_{2probe} measured at 0 V with Eq. 4.9-4.13.

[a] T_i and w_i are fixed.

5

On the superconducting-insulator transition in disordered oxide interfaces

The Superconductor-Insulator transition (SIT) in the two-dimensional electron gas at the $LaAlO_3/SrTiO_3$ interface has attracted attention due to the possibility to tune it with both gate voltage and magnetic field. Moreover, it has been argued that magnetic ordering coexists with superconductivity in this system, and in particular the observation of hysteretic magnetoresistance has been interpreted to be one of the manifestations of that phenomenon. In this work, we have studied two different disordered oxide interfaces, namely amorphous $LaTiO_3/SrTiO_3$ and intermixed $LaAlO_3/GdTiO_3/SrTiO_3$. We observed that both systems show the behavior of granular superconductors and also a gate-tunable SIT. Moreover, both systems show hysteretic magnetoresistance. However, we will argue that such hysteresis arises from the granular superconducting state, and not from magnetic order.

5.1. Introduction

The occurrence of superconductivity in the two-dimensional electron gas at the interface between $SrTiO_3$(STO) and another oxide with a crystalline [3, 4, 57, 140] or amorphous [226] structure is a well-established fact. The superconducting state can be driven into a weakly localized metallic state by applying a gate voltage [4] or a magnetic field [73, 169]. This is usually called a Superconductor-Insulator transition (SIT) since the weakly localised state is often referred to as insulating. The first study of the nature of the SIT with gate voltage in $LaAlO_3$/STO (LAO/STO) [4] considered the behavior of the critical temperature (actually the Berezinskii-Kosterlitz-Thouless temperature T_{BKT}) as function of back gate voltage, using the concept of a quantum critical point. A scaling theory analysis gave a product of the critical exponents $\nu z = 2/3$, indicating a fermionic scenario, while at the same time the critical resistance at the transition was close to 6.5 kOhm, which is expected for a dirty boson scenario [70–72]. The difference between two scenarios is the behavior of Cooper pairs across the transition. In the fermionic scenario, Cooper pairs are destroyed on the nonsuperconducting side [71]; in the dirty boson scenario, they survive in mesoscopic puddles [70–72]. Subsequent work by Biscaras *et al.* [169] on the magnetic-field-driven SIT in $LaTiO_3$/STO (LTO/STO) showed multiple quantum critical points, but basically concluded for a bosonic scenario. That scenario was also supported by a study of the magnetic-field-driven SIT in LAO/STO, but the product of the critical exponents was $\nu z = 7/3$, which corresponds to quantum percolation in insulating state [73], *i.e.*, Cooper pairs tunnel between localized superconducting islands [72]. On the whole, a dirty-boson scenario involving a (dirty boson) inhomogeneous superconducting state is an accepted picture for the SIT at oxide interfaces.

Another and somewhat puzzling aspect comes from the issue of the possible existence of magnetism. Signatures of magnetism in the superconducting state were found by SQUID microscopy [6] and magnetic torque experiments [7]. At the same time, the transport measurements demonstrated hysteretic magnetoresistance in superconducting LAO/STO [8, 74, 79, 80], which then also were interpreted as evidence of the coexistence of superconductivity and magnetism. Moreover, superconductivity and hysteresis also were observed in the LAO/STO interface delta-doped by ferromagnetic $EuTiO_3$ (ETO) [132]. The hysteresis was found at gate voltages where also an Anomalous Hall Effect (AHE) was observed, as a hallmark for magnetism. Neither hysteresis nor AHE was present at gate voltages which invoked the insulating Kondo-like state, either above or below T_c.

In this work we present a study of SIT in two disordered oxide interface

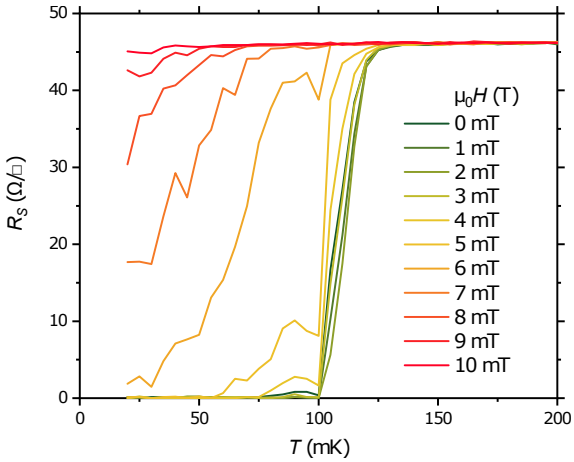

Figure 5.1: Sheet resistance R_S as function of temperature T at different magnetic fields applied out of the sample plane, as indicated. The sample is a-LTO/STO.

systems, namely amorphous LTO/STO (a-LTO/STO) and intermixed crystalline $LaAlO_3/GdTiO_3/SrTiO_3$. Details of sample growth, in both cases, have been described in the Chapters 3 and 4. Previously, we found for a-LTO/STO, that the LTO layer tends to amorphize, and these heterostructures show gate tunable superconductivity in wide voltage range with strong indications of large spatial non-uniformities(see Chapter 4). The second system suffered from strong intermixing, and layers are rather $La_{1-x}Gd_xAlO_3/Gd_{1-y}La_yTi_{1-z}Al_zO_3$/STO (LGAO/GLTAO/STO). This system exhibits an Anomalous Hall effect (AHE) at 3 K without hysteresis and, as we found, without becoming ferromagnetic. The point to make here is that in both cases a gate-tunable SIT is present, and hysteresis is found, but this appears to be due to the granular superconducting state of the system and not to any magnetism. In a-LTO/STO, to be presented first, we find a re-entrant superconducting transition due to large scale inhomogeneities. In LGAO/GLTAO/STO we find a temperature dependence on the insulating side that usually observed in other systems with disordered SIT, but so far has not been reported in LAO/STO.

The samples were measured in a Van der Pauw geometry using a dilution refrigerator (a Triton from Oxford Instruments)[1]. The gate voltage was always swept from positive to negative, with a starting point at 100 V.

[1]The transport measurements were performed by Dr. Martin Stehno at the University of Twente

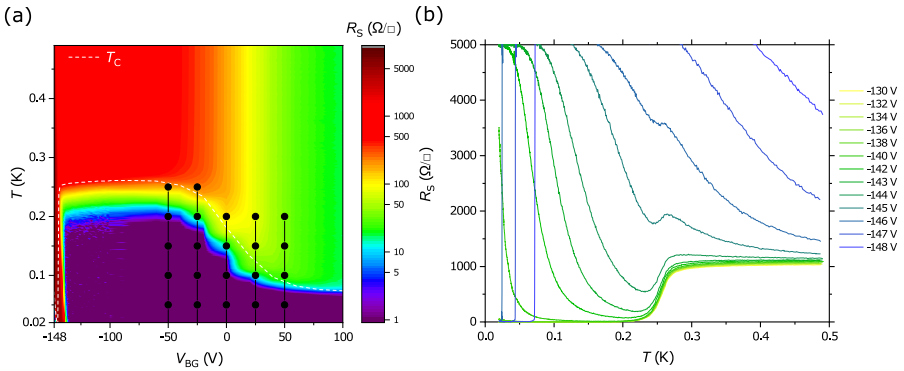

Figure 5.2: (a) Resistance map of a-LTO/STO with the color scale indicating the magnitude of the sheet resistance R_S. Black dots represent points where the field dependence of the *MR* was measured (see Fig. 5.3). Black vertical lines are guides to the eye. The white dashed line represents T_c determined as the temperature at 50% drop of the sheet resistance. (b) $R_S(T)$ at different gate voltages for LTO/STO near the Superconductor-Insulator transition (SIT).

5

5.2. Study of a-LTO/STO

5.2.1. Results

We start with the temperature dependence of the sheet resistance in different fields (Fig. 5.1) oriented in the out-of-plane direction. Compared to previous measurements on LAO/STO [3, 57], much smaller fields are required to suppress the superconductivity in a-LTO/STO. At low fields (< 5 mT), the sample shows a steplike drop in resistance at high temperatures and a shoulder feature at low temperatures. The initial drop is almost unaffected by the applied field in contrast to the shoulder. This behavior, and the low fields involved, make clear that we do not observe a conventional critical field H_{c2}. The response rather resembles that of granular cuprate superconductors [245–247], granular NbN films [248] and proximity coupled superconducting arrays [249, 250]. The drop corresponds to developing superconductivity in granules, and the shoulder is due to transitions in the weak links between granules.

To investigate the superconductivity further, we applied a back gate voltage V_{BG}. Fig. 5.2a shows the color-coded sheet resistance R_S as function of V_{BG} and temperature. Superconductivity with a low T_c persists up to 100 V, but the values usually found in these systems, around 200 mK, are found for negative V_{BG}. The step-like features in Fig. 5.2a are an artifact due to large (20 V) spacing used to measure

curves above -60 V. The shows a sharp SIT at large negative gate voltages. Although usually less sharp [4, 59], some groups have observed such a sharp transition [60]. In Fig. 5.2b we show the temperature dependence of R_S for different V_{BG} at the onset of the SIT. In the region intermediate between superconducting transitions and a monotonous resistance rise, we find that R_S goes through a minimum. A further decrease of the gate voltage appears to lead to re-entrance, which may be due to a very inhomogeneous superconducting state in a-LTO/STO as we observed it previously (see Chapter 4); or, more likely, to an artefact when the sample resistance becomes larger than the amplifier impedance.

Besides the SIT, we observe hysteresis in the magnetic field dependence of R_S below T_c (with the field again pointing out of the plane). Fig. 5.3 shows that such hysteresis becomes significant below the 50% resistance decrease line in the superconducting transition, indicating the correlation with the superconducting state. The sweep rate for this measurement was 0.833 mT/s. The butterfly shape of the hysteresis is similar to the earlier reports in LAO/STO [8, 74]. This shape is peculiar because the hysteretic loops open up before field passes zero during the reverse sweep. Such behavior is not at all typical for ferromagnet, where the opposite would be expected, but often can be seen in granular HTC materials due to flux dynamics and trapping [246, 247, 251–257]. The fields of the dip features do not change significantly with temperature.

Following up on the thought of flux dynamics, we next consider the sweep-rate dependence of hysteretic magnetoresistance (*MR*) in more detail. The *MR* at V_{BG} = 30 V and T = 25 mK at different sweep rates between roughly 0.8 mT/s and 0.03 mT/s are presented in Fig. 5.4a for both directions of the field sweep, and, for clarity, in Fig. 5.4b for a single (negative to positive) direction. We see various dips develop. In the down sweep, an increasingly large dip (with increasing sweep rate) develops on the positive field side before crossing zero field, followed by a smaller dip in the negative quadrant, while in the sweep up, the situation is reversed. Note that dip on decreasing sweep has not been observed by Mehta *et al.* [74]. Moreover, we found that the sweep rate dependence of the magnitude of big and small dips are different. To describe the behavior we use the ratio of the dip resistance R^{dip} normalized by its highest value $R^{dip}_{0.8}$, at the fastest sweep rate of 0.83 mT/s. We find that the ratio can be fitted by a power law.

$$R^{dip}/R^{dip}_{0.8} = A(\mu_0 \dot{H})^p, \tag{5.1}$$

where $\mu_0 \dot{H}$ is sweep rate, and A and p are fitting parameters. The first forward dip is better fitted with equation

$$R^{dip}/R^{dip}_{0.8} = 1 + Ce^{-\mu_0 \dot{H}/R}, \tag{5.2}$$

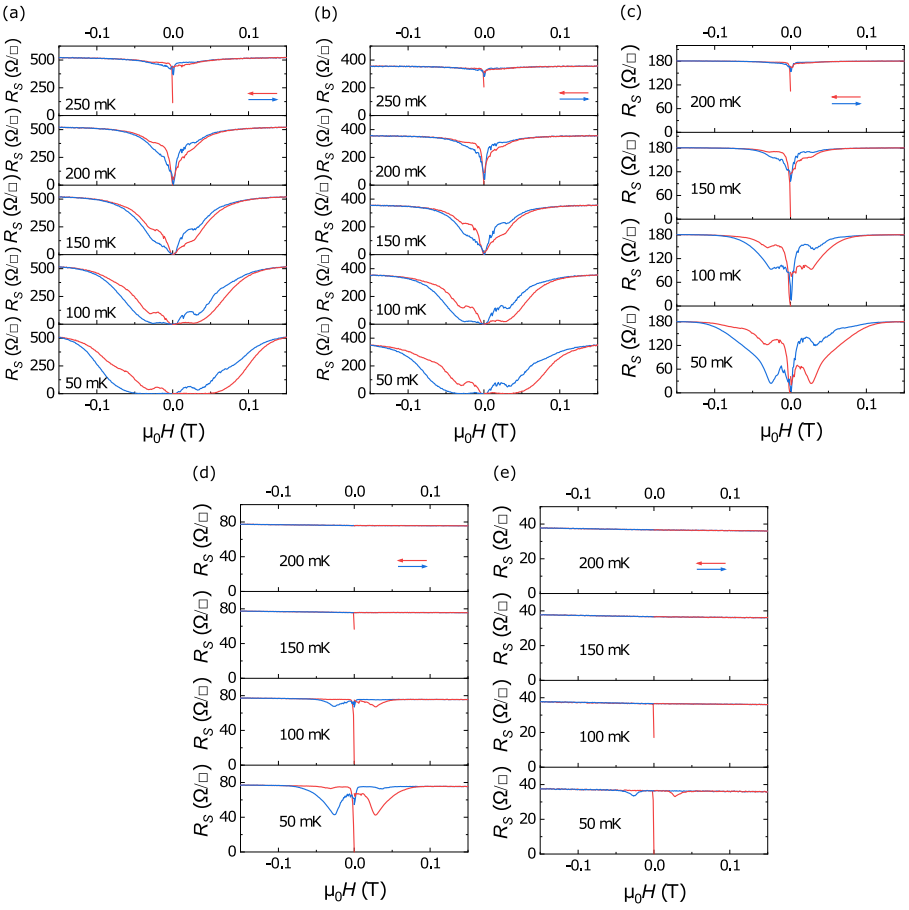

Figure 5.3: Magnetoresistance hysteresis in a-LTO/STO at various temperatures and at the following back gate voltage: (a) -50, (b) -25, (c) 0, (d) 25 and (e) 50 V.

where C and R are fitting parameters. The fit of the data with Eq. 5.1 and 5.2 is shown in Fig. 5.4c.

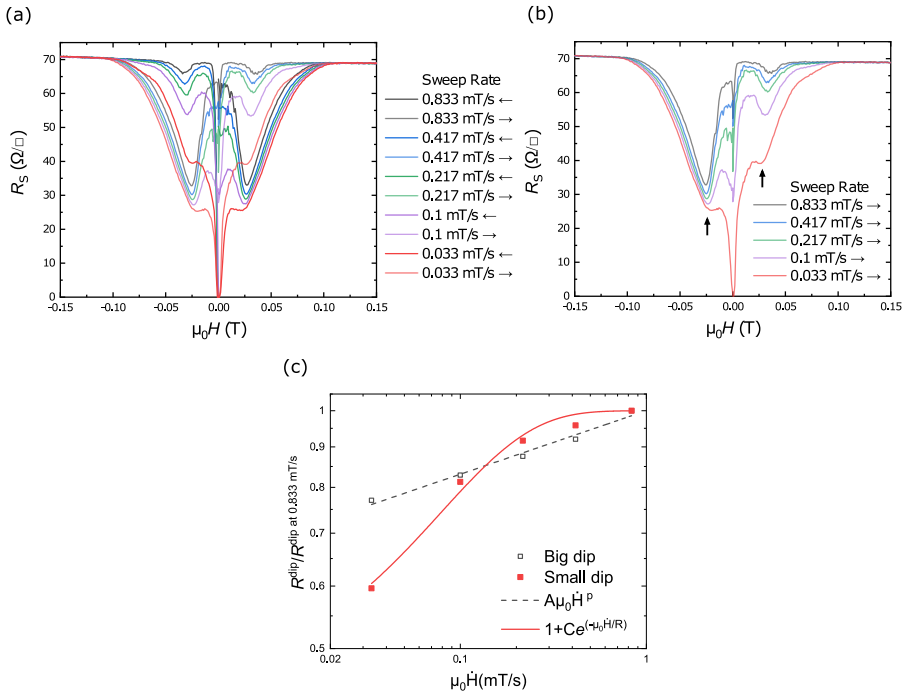

Figure 5.4: (a) Magnetoresistance in a-LTO/STO at different magnetic field sweep rates for a gate voltage of 30 V at 25 mK. (b) The same data, but only one sweep direction is shown. The left-hand arrow shows the position of the big dip, the right-hand arrow that of the small dip. (c) Sweep rate dependence of normalized dips in a-LTO/STO and corresponding fits. Note the log scale on the horizontal axis.

5.2.2. Discussion

Hysteretic *MR* was studied in various STO-based structures, and to draw conclusions with respect to the effects of superconductivity and, possibly, magnetism, it is important to consider the temperature where the hysteresis disappears, and the dependence on sweep rate. In LAO/STO nanowires [80], hysteris disappears well above T_c and is sweep rate independent; similarly, in LAO/$EuTiO_3$/STO [132] hysteresis is observed above T_c. Also in GTO/STO, GTO/STO/GTO [174], and in La:STO [174] structures, hysteresis was found above T_c, but presence or absence of sweep rate dependence was not reported. In these systems, magnetism probably plays a role, although effects of heating while sweeping the field, and subsequent

hysteresis, cannot be always ruled out [81, 82, 258]. In LAO/STO itself, the situation is still no clear. Dikin *et al.* reported the onset of hysteresis in out-of-plane *MR* with an onset at T_c, but in the insulating phase also hysteresis at higher temperatures [8]. In later work, they also reported a sweep rate dependence of the hysteresis [74]. The results were interpreted as the co-existence of magnetism and superconductivity. Our results (hysteresis and a sweep rate dependence below T_c would indicate that no magnetism needs to be assumed on the superconducting side, but can exist on the insulating side of the doping phase diagram. In Ref. [79], hysteretic in-plane magnetoresistance was found to develop below T_c, which was explained by the existence of ferromagnetic dipoles outside the 2DEG.

In our case, as we know from TEM studies (see Section 4.3.1, a-LTO/STO is amorphous. Redox reactions in a-LTO/STO cannot be well controlled and can easily lead to the development of large inhomogeneous regions leading to percolation behavior(see Chapter 4). Therefore, other mechanisms may lead to hysteretic *MR*. In particular flux trapping in granular superconductors can give rise to the hysteresis of the critical current [246, 253, 256, 257, 259], which leads to hysteretic magnetoresistace [247, 251, 252, 254, 255]. Qualitatively it can be described by a two-level model, where the sample is represented by superconducting grains and a weak link network [257, 260]. In such systems, the magnetic flux can be trapped in grains, with shielding current flowing through the network of weak links [257]. Applying this to our case, the initial field increase leads to penetration of the magnetic field through the weak links, to the destruction of the weakest Josephson junctions, and, therefore, to an increase of resistance. The non-monotonous dependence of resistance in increasing branch of the field sweep dependence can be a result of complex rearrangements of weak links or the pinning of Josephson vortices in intergranular media. At some magnetic field, the magnetic flux will penetrate the grains and produce a current, which leads to diamagnetic contribution to the magnetization. When the magnetic field decreases, this current is reversed and produces a paramagnetic contribution to the magnetization, reducing the average field within junction in the Josephson junction network. The field at which the dip on the reverse curve reaches its minimum is the point where there is a maximum cancellation between the applied field and trapped flux. With the further reduction of the magnetic field to zero, most of the flux escapes from the weak link network, and magnetic flux from grains suppresses the maximum of critical current. In reversing the magnetic field, the trapped flux will be aligned with the applied field suppressing critical current further. Moreover, this will not be a two-level system; the strength of the Josephson coupling can vary across samples producing more complex magnetization behavior of grains and intergrain media [255, 257]. This and complex pinning mechanism are the most likely reasons why we do not observe the expected dependence $R \propto ln(\dot{H})$ [261–264].

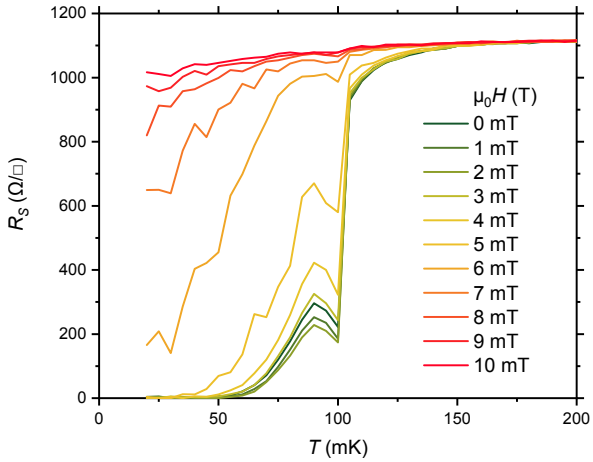

Figure 5.5: The sheet resistance $R_S(T)$ at different out-of-plane magnetic fields for LGAO/GLATO/STO.

5.3. Study of LGAO/GLATO/STO

5.3.1. Results

The temperature dependence for different magnetic field of LGAO/GLATO/STO is shown in Fig. 5.5 and, like a-LTO/STO, exhibits small critical fields, as well as an initial drop in resistance at high temperatures followed by a shoulder feature at low temperatures. The drop and shoulder behave qualitatively similar to a-LTO/STO and point again to the existence of granular superconductivity. However, backgate experiments find quite different behavior for the SIT in the sense that it occurs at a much smaller negative gate voltage, around -5 V to -10 V, as shown in Fig. 5.6a. From the temperature dependence of the sheet resistance in Fig. 5.6b it can be seen that there are three distinct regimes, superconducting, metallic, and insulating. The 50% line (resistance has dropped to 50% of the normal state value) of T_c in Fig. 5.3a has a sharp decrease near SIT, indicating insensitivity to small features in transition.

In this case, to study the superconducting state, we measured $I(V)$ curves at different temperatures and gate voltages. Measurements at 40 V, 20 V, 5 V and 0 V are presented in Fig. 5.7a-d. The $I(V)$ curves, presented in log-log fashion, show multiple steps, which indicates inhomogeneous superconductivity in our sample similar to LAO/STO [3]. In various sections of the $I(V)$ curves we observe power-

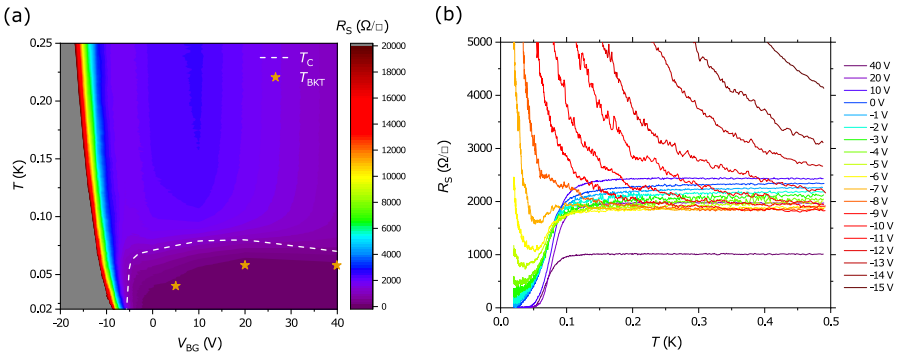

Figure 5.6: (a)-(b) Resistance map of LGAO/GLTAO/STO with the color scale indicating the magnitude of the sheet resistance R_S. Stars and dashed line represent T_{BKT} determined from the $I(V)$ characteristics and T_c determined as the temperature at 50 % drop of the sheet resistance. (b) $R_S(T)$ at different gate voltages for LGAO/GLTAO/STO.

law dependences and from that determined the Berezinskii–Kosterlitz–Thouless transition temperature (T_{BKT}) using the $V \sim I^3$ criterion [3]. It means we find the temperature where that power law holds, as indicated by the dashed lines in the Figure. Note that the same power 3 holds for homogeneous systems and for proximity-coupled superconducting arrays [249]. The values for T_{BKT} do not follow the 50% line, and in particular drop below the lowest measured temperature at 0 V, close to when $R(T)$ start to exhibit finite resistance. Furthermore, T_{BKT} is significantly below the 50% line, indicating again that T_c is not that of a homogeneous system but rather the signature of the formation of weak link network like in granular superconductor system [248], similar to Josephson Junction arrays [249, 250]. Recently, it was argued that $V \sim I^3$ scaling in STO-based interfaces can arise due to puddle-like inhomogeneities [265] where the network is built from puddles with different strength rather than connected by weak links, but for our LGAO/GLTAO/STO sample a two-level model based on the superconducting granules and weak links network, where $V \sim I^3$ is signature of superconductivity in weak links [257, 266] describe data better.

The temperature dependence of the resistance in the insulating phase can be described by Efros–Shklovskii (ES) variable range hopping [267] of the form

$$R_S(T) = R_0 e^{\sqrt{T_0/T}}, \tag{5.3}$$

where T_0 and R_0 are fitting parameters. In order to see that, in Fig. 5.8a we plot R_S versus $T^{-1/2}$ on a logarithmic scale. We see the ES-dependence develop from -5 V onward. The fitting parameters T_0 and R_0 are given in Fig. 5.8b. Similar dependen-

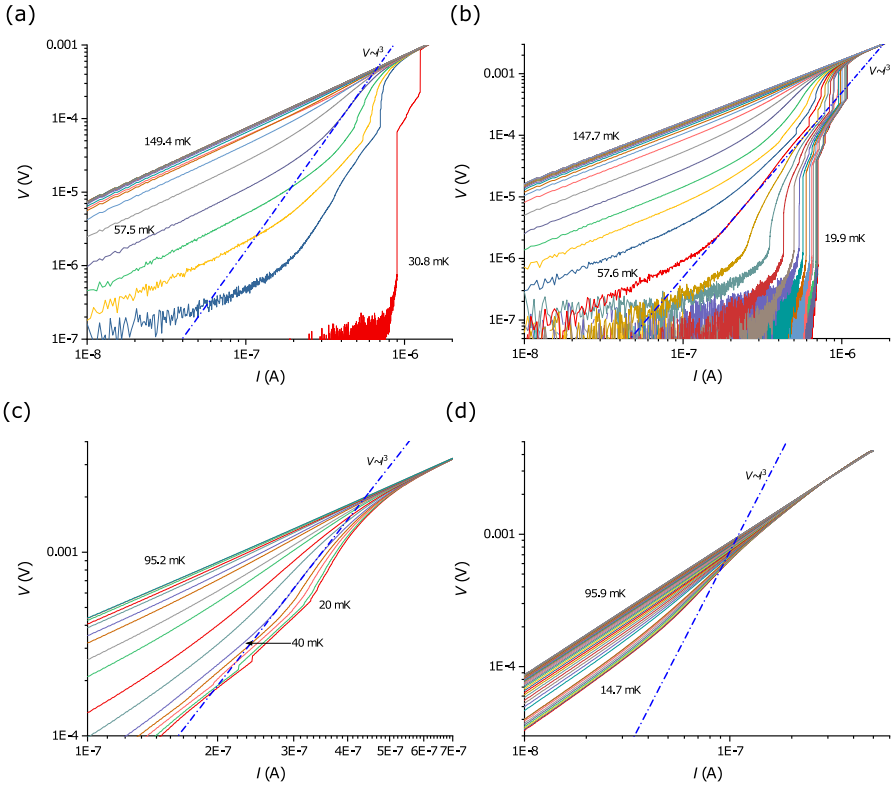

Figure 5.7: $I(V)$ characteristics taken on LGAO/GLTAO/STO at (a) 40 V, (b) 20 V, (c) 5 V and (d) 0 V. The dashed lines show the $V \propto I^3$ behavior used to determine the Berezinskii-Kosterlitz-Thouless temperature T_{BKT} correspondingly.

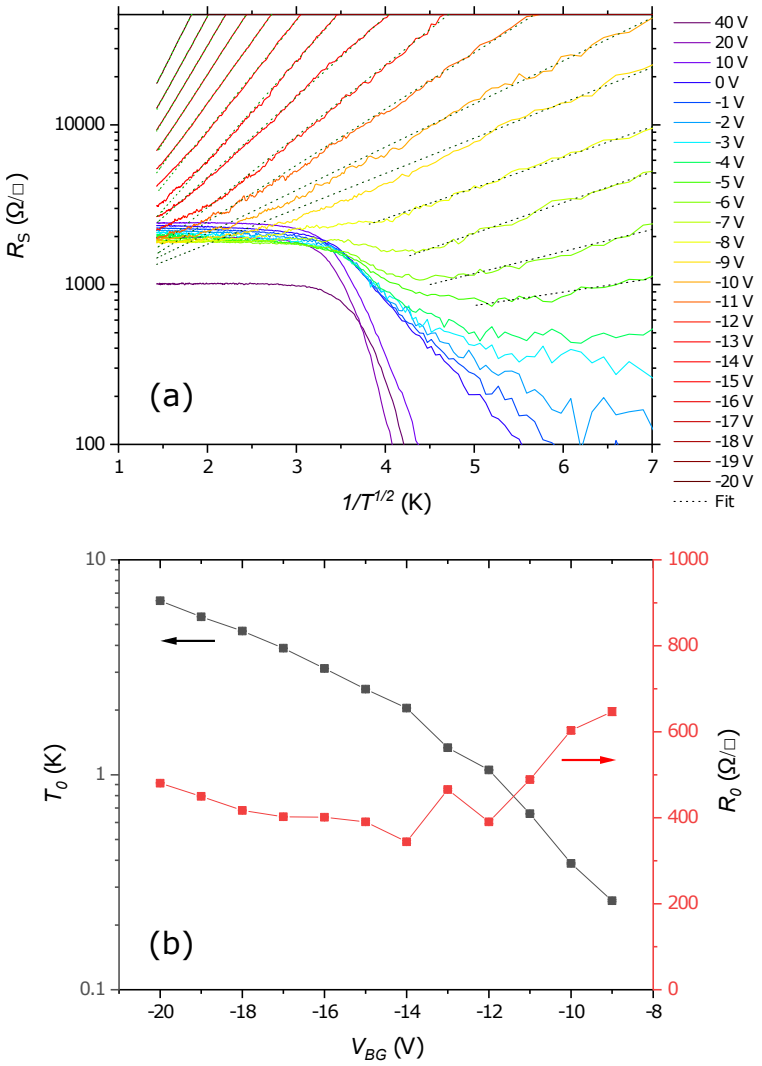

Figure 5.8: (a) Resistance versus $T^{-1/2}$ for LGAO/GLTAO/STO at different gate voltages. The dashed lines are used to fit variable range hopping behavior (see text). (b) Variation of the fit parameters of Eq. 5.1 with applied gate voltage V_{BG}.

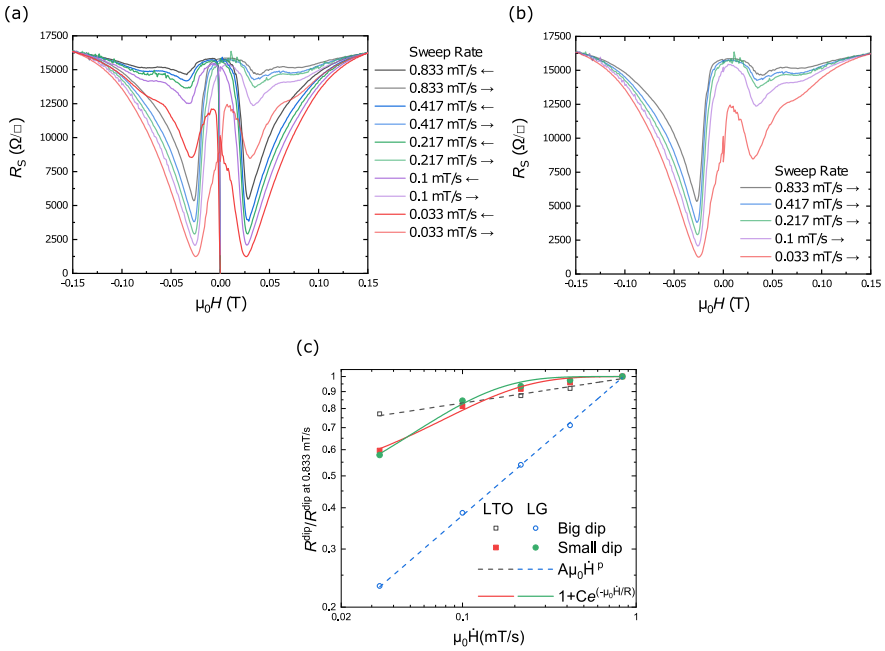

Figure 5.9: Magnetoresistance in LGAO/GLTAO/STO at a gate voltage of 30 V and at 25 mK for different magnetic field sweep rates in (a) both directions and (b) in one direction. (c) Sweep rate dependence of normalized dips and corresponding fits for LGAO/GLTAO/STO (denoted LG in the legend) and a-LTO/STO (denoted LTO in the legend).

cies have been reported for many systems exhibiting SIT, among them HTC's [268], metal films [266, 269], and superconductor-semiconductor arrays [270]. As can be seen in Fig. 5.8b, the prefactor R_0 varies with the gate voltage in a similar manner as Pb and Al films, where the prefactor depends on thickness [266]. One note to make is that, although we found that a function with power 1/2 in the exponent describes our data best, we cannot fully exclude a 1/3 dependence, which is expected for Variable Range Hopping in two dimensions. Moreover, we were not able to observe activated behavior, which may appear at even lower gate voltages, but there the sample became too insulating to measure in our setup's temperature range.

In the magnetic field dependence of the resistance (see Fig. 5.9a,b), we observe butterfly-type hysteresis in the superconducting regime, again as in a-LTO/STO. Furthermore, the hysteresis is sensitive to the field sweep rate, and the rate dependence of the dips can be fitted with Eqs. 5.1, 5.2. By driving LGAO/GLTAO/STO

through the SIT (which could not be done in a-LTO/STO) we observed a change of hysteresis (Fig. 5.10a) somewhat similar to Ref. [74]. There is no significant change between -2 V and -6 V, but at -8 V, where the local minimum on the R_S(T) curve vanishes, a crossover occurs to a different type of behavior, where the resistance of the back sweep in the positive quadrant lies above the up sweep. We should point out here that it is significant that hysteresis also and still can be observed in the insulating state at -11 V. Figs. 5.10b,c show the temperature dependence of this effect at -8 V and -11 V. At -8 V, hysteresis is already visible at 100 mK, which corresponds to T_c in the metallic state, even though R_S at that gate voltage does not show a dip anymore. Also at -11 V, hysteresis sets in at 100 mK. The observations clearly point to a state in which superconducting puddles or granules exist with a T_c of the metallic state, but where phase coherence has been lost.

One more often observed feature of the *MR* curves is a strong relaxation of the resistance when applying the field for the first time. This is seen as sharp spikes in Fig. 5.10 where the resistance increases (decreases) on the superconducting (insulating) side of the SIT. Such transient decrease near zero field was previously reported by Ref. [258], who argued that the relaxation effect of the magnetization in the sample leads to such behavior, but we observed the effect only during the initial sweep away from 0 T and not following ones. The behavior can be a sign of the magnetocaloric effect. On the other hand, developing percolation paths made of weak links, which are destroyed by a magnetic field, also can lead to such effects, especially since our samples have relatively low critical fields in the superconducting state. As we showed previously for such inhomogeneous sample measured in the VDP geometry, an increase of resistance with cooling can occur when some regions in the sample undergo a superconducting transition, but their contribution to the measured voltage yields an increase of voltage instead of decrease [230](also see Chapter 4). The application of the external magnetic field destroys these regions, and the resistance will decrease or increase depending on the distribution of the weak links.

5.3.2. Discussion

We already discussed the a-LTO/STO behavior, and the differences in magnetotransport properties between that system and LGAO/GLTAO/STO are likely to originate from a different type of disorder. In contrast to amorphous LTO/STO, LGAO/GLTAO/STO is crystalline, but strongly intermixed. In LGAO/GLTAO/STO the magnetic ions such as Gd^{3+} with 7 f-electrons and Ti^{3+} with 1 d-electron are brought to be right at the interface and in particular the Ti^{3+} distribution is in-

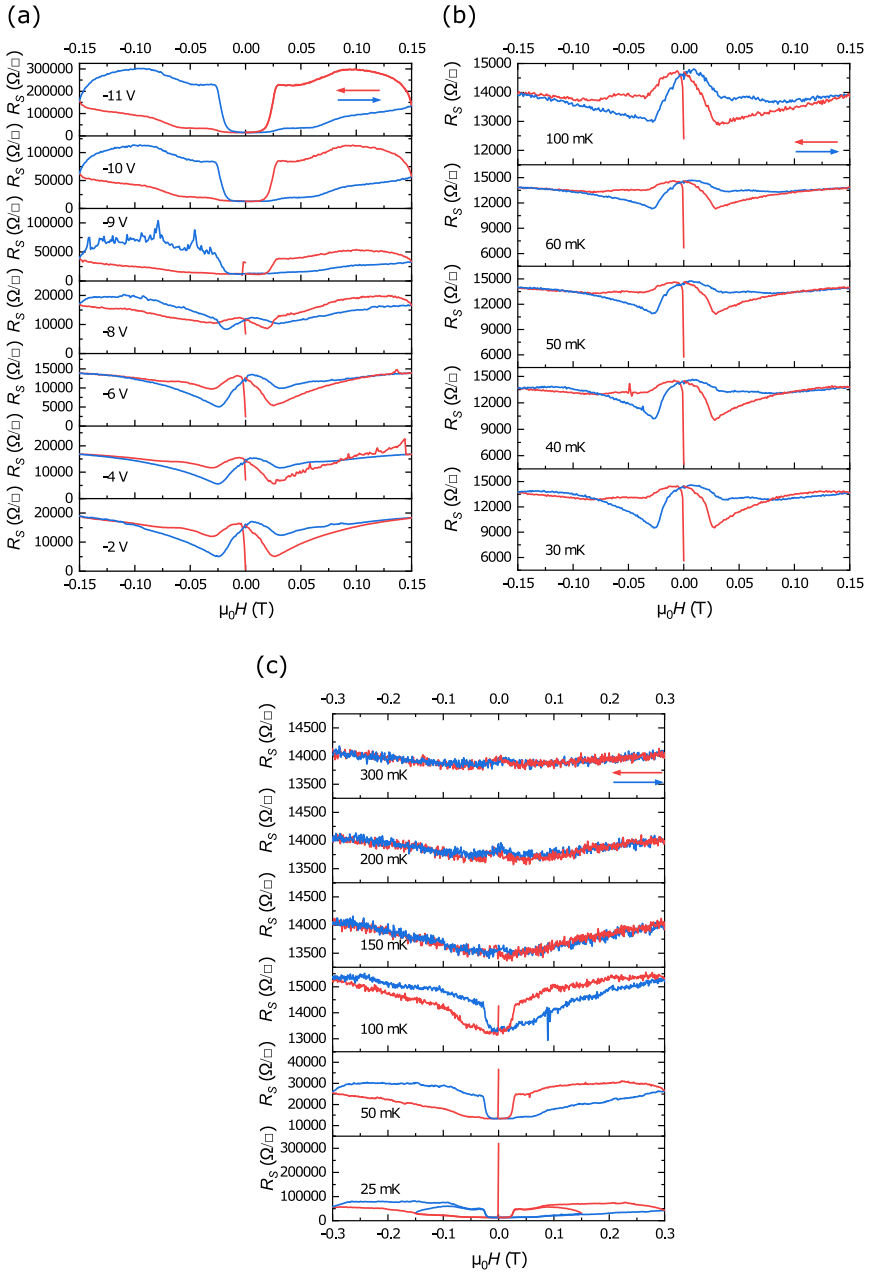

Figure 5.10: (a) Magnetoresistance *MR* for LGAO/GLTAO/STO at different gate voltages across the Superconductor-Insulator Transition (SIT) and 25 mK with a sweep rate of 0.033 T/s. (b) *MR* at various temperatures at −8 V with a sweep rate of 0.833 T/s and (c) at -11 V with sweep rate 0.033 T/s.

homogeneous. Magnetic doping suppresses the development of superconducting regions and Josephson coupling between them and, overall, leads to the lower T_c and T_{BKT} we observe. Nevertheless, this system exhibit a SIT very similar to that of granular superconductors, and many properties of this system can be understood via two-level model [257, 260] similar to case of a-LTO/STO, but the signatures of such behaviour in in the SIT is more pronounced. Moreover, driving system into insulating state in LGAO/GLTAO/STO requires smaller gate voltage range. This is in agreement with previous reports on Josephson coupling between superconducting islands in crystalline (but non-magnetic) STO-based structures [58, 60–62, 64].

The presence of magnetic doping and tunable AHE at normal state (see Chapter 3) point out that the magnetic origin of hysteresys in LGAO/GLTAO/STO can be possible. However, if we compare LGAO/GLTAO/STO with another magnetically doped interface LAO/ETO/STO, which also show tunable AHE [132], we found significant difference in their behaviour. In LAO/ETO/STO, hysteresis disappears on the Kondo-like insulating side, which is set in at voltage above SIT [132]. Moreover, the shape of hysteresis is different, and, in contrast to the LGAO/GLTAO/STO mentioned above, there is no sweep rate dependence of *MR* in LAO/ETO/STO. Still, a non-uniform magnetic state of GLTAO layer can give rise of some features of hysteresis; this non-uniform magnetic doping can enhance vortex formation as well as flux pinning at LGAO/GLTAO/STO in a somewhat similar manner to superconducting PbBi with Ni wires on top [271].

At the same time a similar behaviour of hysteresis in a-LTO/STO is indicated on the granular superconductivity as the main source of hysteresis. Indeed, the hysteresis has a characteristic butterfly shape and develops below onset of superconductivity with lowering temperature. Furthermore, the sweep rate dependents of the *MR* peaks can be fitted with the same functions as in a-LTO/STO. As we mentioned above the sweep rate dependence can be signatures of magnetocaloric effect, but the shape of hysteresis is ferromagnetic one [81, 82, 95, 258] only in insulating side of SIT.

5.4. Summary

To summarize, we have studied the occurrence of Superconductor-Insulator transitions in an amophous oxide interface system, a-LTO/STO, and in a crystalline one, LGAO/GLTAO/STO. We have observed that both systems exhibit granular behavior, but the behavior across the SIT is different due to different types of disorder. Both systems exhibit hysteresis below T_c, and although previously

similar hysteresis was argued to be due to the presence of (coexistent) ferromagnetism, we propose it is rather the signature of granularity in the superconducting systems. a-LTO/STO shows the presence of large scale non-uniformities, and a complex response to magnetic field sweeps which points to varying stregth of superconducting area's and the links between them. LGAO/GLTAO/STO also shows properties of typical granular superconducting material, and can be better described by the two-level model in a simplified picture. The magnetic moments in LGAO/GLTAO/STO seem to suppress the formation of the weak links between grains to the lower temperature and alter properties of this system compare to LAO/STO. Moreover, we observed ES-like temperature dependence of resistance on the insulating side of transition.

6

On a possible Kondo effect in $LaAlO_3/Eu_{1-x}La_xTiO_3/SrTiO_3$ heterostructures

In this chapter, we study $LaAlO_3/Eu_{1-x}La_xTiO_3/SrTiO_3$ structures with different thicknesses of the $Eu_{1-x}La_xTiO_3$ layer and for $x = 0$ ($EuTiO_3$) and $x = 0.1$. We observe that both systems have many properties similar to previously studied $LaAlO_3/EuTiO_3/SrTiO_3$ and other oxide interfaces, such as the formation of a 2D electron gas for 1 or 2 unit cells of $Eu_{1-x}La_xTiO_3$, a metal-insulator transition driven by the thickness increase of $Eu_{1-x}La_xTiO_3$ layer, the presence of an Anomalous Hall effect (AHE) when driving the systems above the Lifshitz point with a backgate voltage, and a minimum in the temperature dependence of the sheet resistance below the Lifshitz point in the one-band regime. However, and notwithstanding the likely presence of magnetism in the system, we do not attribute that minimum to the Kondo effect, but rather to the properties of $SrTiO_3$ crystal and the inevitable effects of charge trapping when using back gates.

6.1. Introduction

Oxide interfaces, mainly based on the $SrTiO_3$ (STO), are systems that have significant freedom of manipulating various properties by applying a gate voltage. Among them, tunable spin polarisation or magnetism, and its signature, the Anomalous Hall effect (AHE), have been extensively studied in the past decade in various STO-based structures [78, 91, 96, 132, 133, 135] (also Chapter 3). The AHE can be completely switched off by a gate voltage. The switch point is strongly connected to the so-called Lifshitz transition [36], which separates two regimes with only $3d_{xy}$ type of orbitals occupied, leading to single band transport, and with $3d_{xy}$ and $3d_{xz/yz}$ and the involvement of two bands. The latter regime coincides with the presence of AHE and, therefore, spin-polarisation [36, 91, 96, 132, 133, 135], whereas the former one a non-spin polarised state where, however, a non-monotonous temperature dependence of resistance with a pronounced minimum has been observed. This behavior of the sheet resistance has been attributed to the Kondo-regime [132, 133]. For STO(001)-based interfaces, it has been proposed that different coupling between the localized magnetic moments and the $3d_{xy}$ and $3d_{xz/yz}$ electrons, due to the different orbital orientation relatively to the interface plane, can explain various magnetotransport properties of STO-structures, including a gate tunable Kondo-like minimum, AHE, and behavior of the in-plane magnetoresistance (*MR*) [90, 96]. Nevertheless, the mechanism for invoking AHE is still a matter of debate. Some studies find an induced AHE in structures with external magnetic delta doping [132, 133], in which case the presence of magnetism can be readily argued. Others find AHE also in systems without magnetic ions and suggest a mechanism arising from the properties of the STO [91, 96]. Also the Kondo-picture proposed by Refs. [90, 96] has been challenged. It was argued that enhanced spin-orbit coupling (SOC) at low temperature can produce some features of the in-plane *MR* which previously have been interpreted in favor of the picture supporting Kondo behaviour [98].

This work aims to study the gate-tunable magnetic interactions. We choose as a starting point the first reported delta-doped system, $LaAlO_3/EuTiO_3$/STO (LAO/ETO/STO). This system is reported to be ferromagnetic [132, 139] and to exhibit both tunable AHE and Kondo-like behavior. Bulk $EuTiO_3$ is an antiferromagnetic band insulator [175–181]. The oxidation state of Eu is Eu^{2+}; therefore, Ti is in the tetravalent state and does not contribute to the magnetization. However, doping with La will lead to the development of ferromagnetism [145, 192], because La is in La^{3+}state, and the doping introduces electrons into the conduction band of the $3d$ t_{2g} states of the Ti, turning ETO in ferromagnetic metal [145, 192]. In our work, to understand the role of magnetic doping on magnetic interactions, we

also investigated nominally non-magnetic LAO/STO and LAO/$Eu_{1-x}La_xTiO_3$/STO (LAO/ELTO/STO).

We have prepared a set of LAO/STO samples with and without ETO and ELTO δ-doping layers and utilized a back gate geometry to study them. We observe that AHE is stronger in samples with a higher concentration of Eu moments and we find a transition between tunable AHE and Kondo-like regimes. Nevertheless, unlike the AHE, the Kondo-like regime seems to be present even in non-doped samples. We come to the conclusion that gate-tunable Kondo-like resistance behavior is not a sign of magnetic interactions, but most likely the result of the interplay between the electron trapping mechanism and the temperature dependence of STO permittivity, the carrier concentration, and various scattering mechanisms. The combination of these effects leads to more effective back gating at low temperatures and therefore to an increase in resistance.

6.2. Experimental details

The oxide structures have been grown by Pulsed Laser Deposition (PLD) on TiO_2-terminated (001)-oriented STO. In the literature, two types of targets have been used to grow ETO, the pyrochlore material $Eu_2Ti_2O_7$ [139, 147, 148, 272–274], and the perovskite material $EuTiO_3$ [146, 150, 189, 275]. In this work, we choose to work with the latter. The PLD targets for ETO and $Eu_{0.9}La_{0.1}TiO_3$ were fabricated from sintered and pressed powders [1]. The LAO target was commercially purchased. The La doping was chosen at 10% to ensure a significant difference between intentionally doped films and unintentional doping due to possible intermixing. Some significant optimization of the growth parameters was required. In order to prevent bulk conductivity of the STO due to oxygen depletion at the high growth temperatures, some oxygen in the PLD chamber is needed, but the oxygen pressure should not be too high otherwise the ETO and ELTO films turn into an amorphous or form a pyrochlore structure.

For ETO and ELTO, the laser spot size was fixed at 1.38 mm^2. For optimisation, we used a fixed thickness of 10 unit cells (u.c.) determined from the periodicity of visible specular beam intensity oscillations using Reflection High-Energy Electron Diffraction (RHEED). Fig. 6.1a shows the number of visible oscillations plotted against growth temperature for the laser fluences 1.1 and 1.54 J/cm^2. The maximum number of visible oscillations is 4, in the temperature range 750-800 °C and at a nominal pressure 1×10^{-4} mbar. Above 4 u.c. thickness, the films re-

[1] The targets were prepared by Dr. Yingkai Huang at the University of Amsterdam

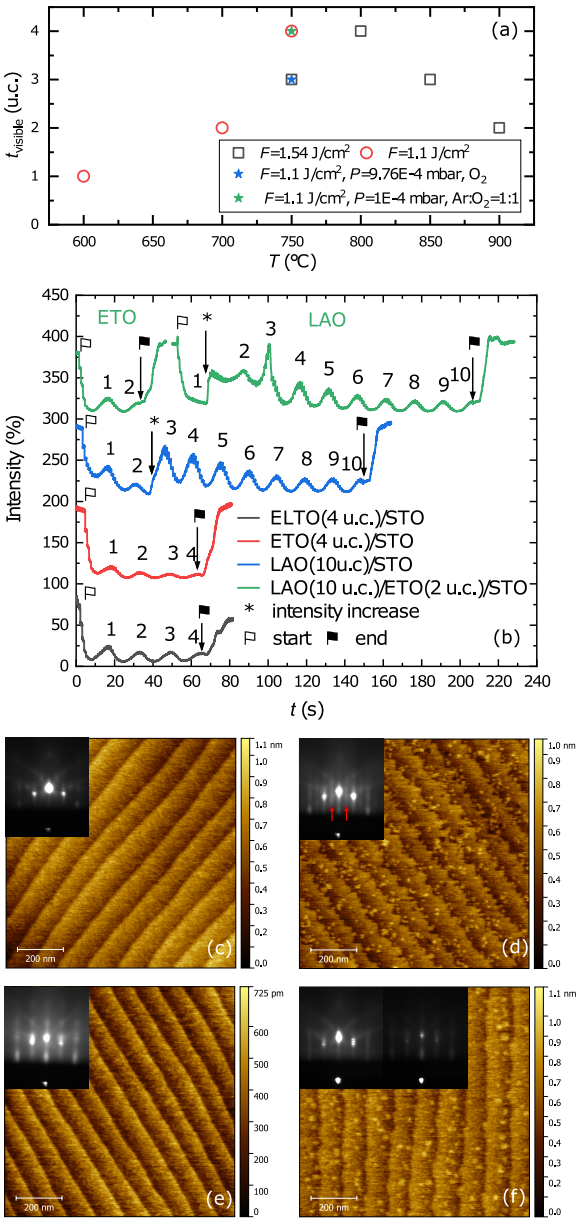

Figure 6.1: (a) Temperature dependence of the visible formation of unit cells extracted from RHEED intensity. If not indicated otherwise, the atmosphere was O_2, and the pressure was 1×10^{-4}. (b) RHEED intensity monitoring. (c)-(f) AFM image of surfaces of TiO_2-terminated STO, ETO(4 u.c.)/STO, LAO/STO, and LAO/ELTO(2 u.c.)/STO correspondingly. On the inserts corresponding RHEED patterns after deposition. Red arrows are guides for the eye. Note on the last insert left RHEED pattern after deposition of ELTO, the right one after LAO.

sult mostly in an amorphous pattern (Fig. 6.8 in the Appendix 6.6), although the samples grown at 1.54 J/cm^2 and 800 °C show some weak signatures of 2D growth (Fig. 6.8a in Appendix 6.6). Still, 4 u.c. is enough to study delta-doped LAO/STO structures. Based on the results above, we chose a fluence of 1.54 J/cm^2 for ETO and ELTO. For LAO a growth fluence of 1.3 J/cm^2 and a spot size of 1.76 mm^2 were used. The temperature was set at 800 °C and the pressure, consisting of a 1:1 mix of Ar:O_2, at 1×10^{-4} mbar. The maximum thickness of $Eu_{1-x}La_xTiO_3$ layer was fixed at 4 u.c. The following samples were grown (the numeral denoting number of u.c.'s): LAO(10)/ETO(x)/STO (with x= 2, 3, 4), LAO(10)/ELTO(x)/STO (with x=2, 4), ELTO(4)/STO, ETO(4)/STO and LAO(10)/STO.

ETO and ELTO show similar growth. The oscillations are clearly visible for ETO(4)/STO and ELTO(4)/STO samples, as shown in Fig. 6.1b (black and red lines). The RHEED pattern for ETO(4)/STO shows additional lines at the 1/2 position between the main lines for films with $t > 2$ u.c. (insert in Fig. 6.1d); such lines have been observed for stoichiometric $Eu_{1-x}La_xTiO_3$ films [149]. The STO surface steps can been clearly seen in the Atomic Force Microscopy (AFM) scan before and after growth (Fig. 6.1c,d), but the edges became more rough than on the bare STO surface. Moreover, there are island-like features in the topography of the film. During the growth of LAO, clear oscillations are seen when growing directly on STO (blue line in Fig. 6.1b). The RHEED pattern shows a transition from 2D growth to 3D growth (insert in Fig. 6.1e), most likely due to the low oxygen pressure. A clear underlying STO step pattern can be seen in the AFM scan in Fig. 6.1e. This is different when the LAO layer is grown on ETO or ELTO films. In Fig. 6.1b (green line) the first two oscillations during LAO growth become less pronounced, and their intensity decreases with the increase of the ETO or ELTO layer thickness. The thickness of the LAO layer was determined from the number of pulses for a single period of oscillations and, strictly speaking, can vary between 8 and 10 u.c. That variation is not crucial for the conductivity of LAO/$EuTiO_3$/STO, in contrast to the thickness of the ETO layer [139]. The LAO layer grown on the ETO or ELTO also shows 3D features in the RHEED pattern, but the 2D features are more pronounced. The underlying topography of ETO/ELTO films can still been seen after depositing the LAO layers. The AFM scans and RHEED patterns for the rest of the films are shown in the Appendix Fig. 6.9. The magnetotransport properties have been measured in van der Pauw geometry in a PPMS with home-built insert as described in Chapter 2.

6.3. Results

6.3.1. Metal Insulator Transition and transport properties

First we show that the behavior of our samples is similar to the ones studied in Refs. [132, 139]. Both our LAO/ETO/STO and LAO/ELTO/STO show a Metal-Insulator transition (MIT) as function of E(L)TO thickness around 2 u.c. (Fig. 6.2a), which is in agreement with the results of Ref. [139]. From now, we will refer to the two conducting samples, LAO(10)/$EuTiO_3$(2)/STO and LAO(10)/$Eu_{0.9}La_{0.1}TiO_3$(2)/STO, as LAO/ETO/STO and LAO/ELTO/STO respectively. Uncapped ETO and ELTO samples were insulating, which means that La doping [145, 192] (or La intermixing in the LAO/$Eu_{1-x}La_xTiO_3$/STO) in our films is not the driving mechanism of the MIT. Furthermore, despite the lower oxygen content, the conductance of our films cannot be attributed to the conduction due to oxygen vacancies in the STO surface alone [95]; the LAO layer is essential for creating the two-dimensional electron liquid. At room temperature, LAO/STO has a lower sheet resistance R_S than LAO/ELTO/STO, which in turn is lower than that of LAO/ETO/STO. The introduction of the thin sheet of $Eu_{1-x}La_xTiO_3$ also changes the temperature dependence of R_S: the LAO/STO sample exhibits a monotonous decrease down to 3 K, whereas the delta-doped samples show an upturn below 10 K (Fig. 6.2b). Such a change in $R_S(T)$ has been reported in Ref. [139] and was attributed to a possible Kondo effect [95, 139].

6.3.2. Magnetotransport properties at zero gate voltage

Before applying gate voltages, we analyze the temperature dependence of the magnetotransport properties for the three conducting samples. In LAO/STO, the value of *MR* as function of an applied magnetic field out of the plane of the sample continuously increases with decreasing temperature (Fig. 6.3a). The high values of *MR*, around 50 %, and the almost linear shape in high fields below 50 K point to spatial conductance fluctuation (see Chapter 4 or [232–238]). In the doped samples, the *MR* behavior is less monotonous; *MR* increased only up to 10-12% until the temperature reaches 10 K (Fig. 6.3c,e). Below that temperature, the *MR* decreases, tracing the upturn in the temperature dependence of R_S.

Below 100 K, the Hall coefficient R_H develops a non-linearity in high fields, indicating the onset of two-band transport [36]. Furthermore, below 10 K, there is also a low-field non-linearity in the magnetically doped samples. This indicates

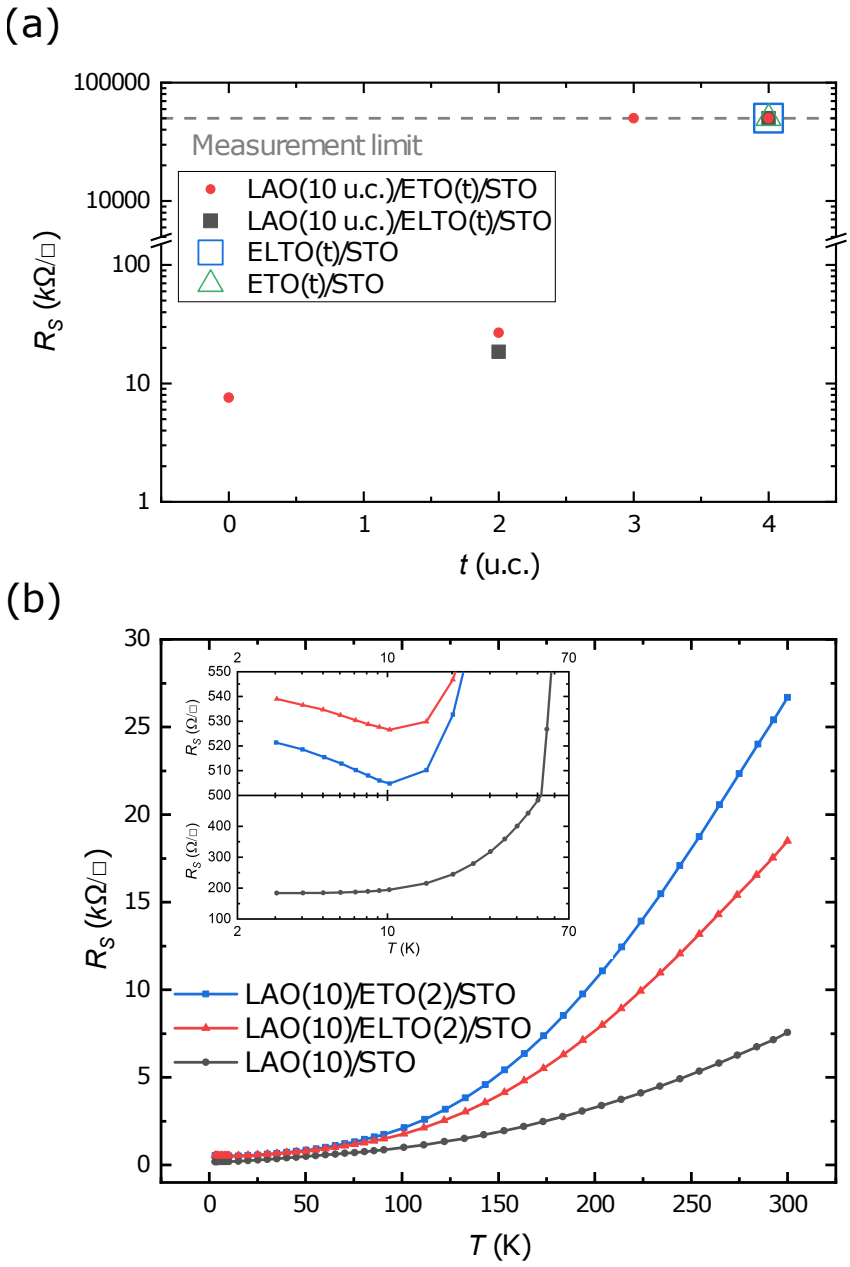

Figure 6.2: (a) The thickness dependence of the sheet resistance R_S at 300 K. (b) Temperature dependence of R_S for conducting samples. In the insert, zoom-in for the low-temperature region.

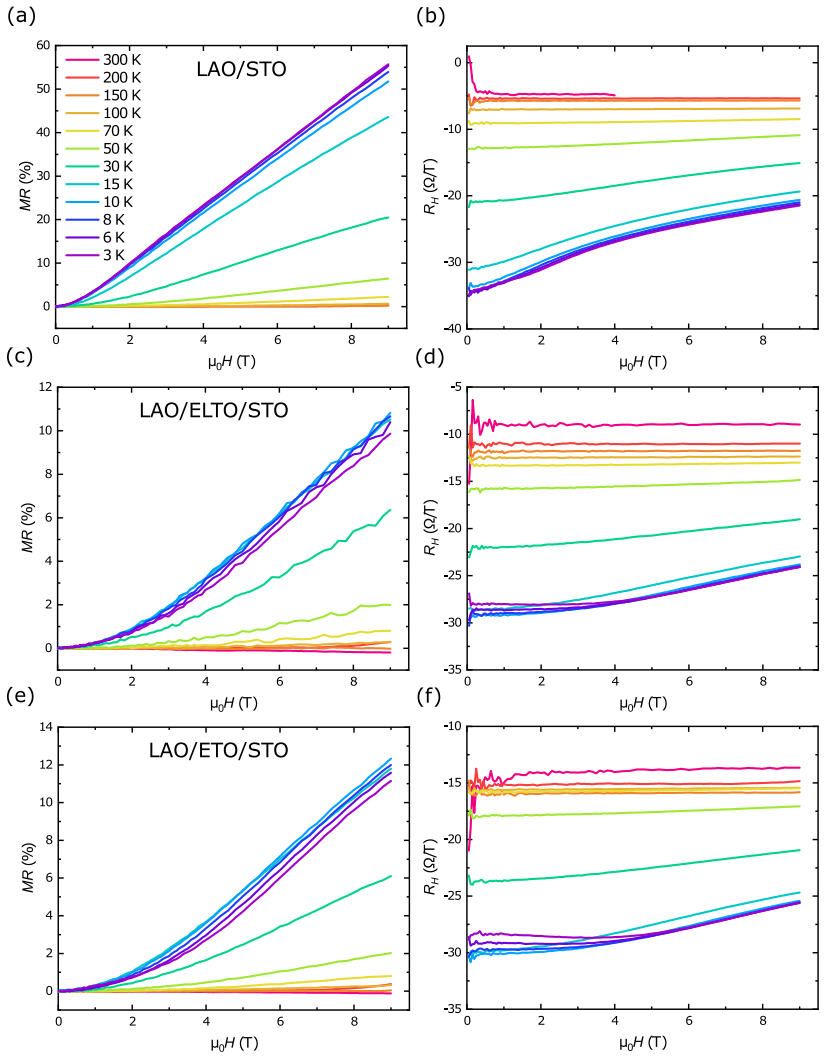

Figure 6.3: Magnetoresistance *MR* at different temperatures indicated by the colors for (a) LAO/STO, (c) LAO/ETO/STO, and (e) LAO/ELTO/STO. The Hall coefficient at different temperatures (same colors as in a,c,e) for (b) LAO/STO, (d) LAO/ETO/STO, and (f) LAO/ETO/STO.

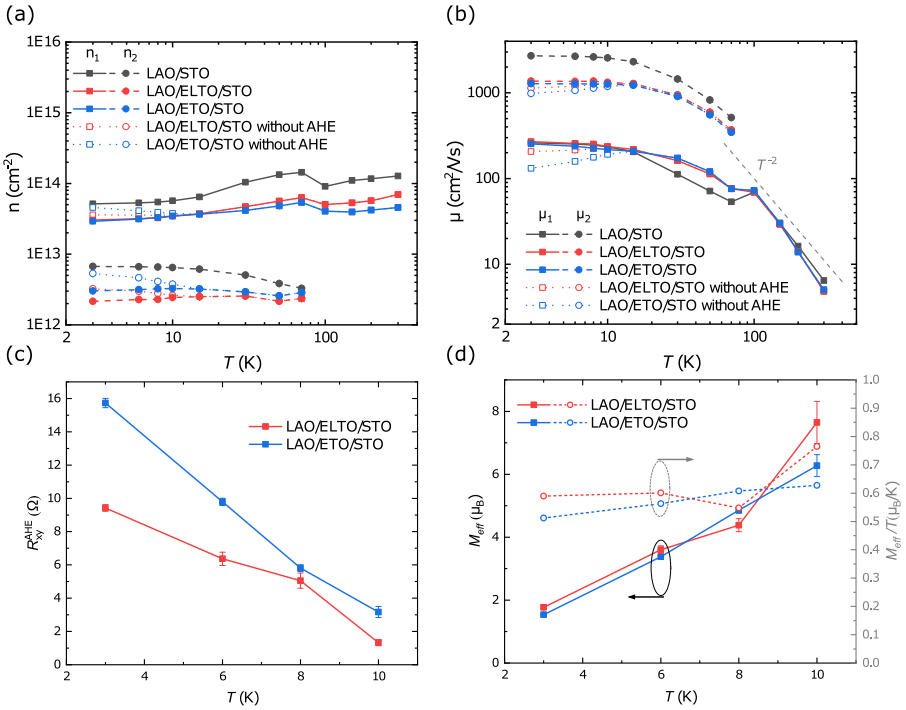

Figure 6.4: For both the LAO/STO and the LAO/E(L)TO/STO samples, the temperature dependence of (a) the carrier concentrations n_i, (b) the mobilities μ_i, (c) the Anomalous Hall coefficient, and (d) values of M_{eff} (filled symbols) and the ratio M_{eff}/T ratio (open symbols) taken from fitting as described in the text. Note that n_i and μ_i is given with and without correction for AHE when appropriate.

the presence of an Anomalous Hall Effect (AHE) [36, 91, 132] (see also Chapter 3). To analyze the data with respect to carrier densities n_i and mobilities μ_i in the presence of AHE, we followed the subtraction method described in Chapter 3 as Method 1. To increase the precision of the fit, we used the derivative of the subtraction result to determine the fitting range. The two-band analysis in a regime without AHE was performed using the fitting of the conductance tensor components [37] (also Section 3.3.5). The extracted values for n_i, μ_i, and for the Anomalous Hall coefficient R_{xy}^{AHE}, and the effective magnetic moment M_{eff} are shown in Fig. 6.4. Also shown are the values for n_i, μ_i when no AHE is taken into account. We see that in the one band region, the mobility of the samples roughly follows a T^{-2} dependence in the temperature range 150-50 K (Fig. 6.4b). The temperature dependence above 150 K is often ascribed to longitudinal optical phonon scattering, and the origin of T^{-2} mobility dependence is usually attributed to electron-electron scattering [276, 277]. As was mentioned above, the second band appears below 100 K. Some unphysical jumps are probably related to the low carrier concentration of the second band leading to overestimating (underestimating) the carrier concentration (mobility) for both type of carriers. Overall it is clear that the trend is an increase of $\mu_{1,2}$ towards low temperatures with saturation below 10 K and a continuous although small decrease of n_1. The saturation of the mobility at a low-temperature limit is most likely due to the interface, to ionized donors, and to ionized impurity scattering [276]. In the fit without the AHE, with decreasing temperature we see an increase in carrier concentration and an decrease in mobility for the magnetically doped samples below 10 K. However, when accounting for the AHE, the fits become consistent with the general trend of LAO/STO. The AHE grows when lowering the temperature, but we see that the fit parameter M_{eff} decreases almost linearly with temperature as can be seen better from the ratio M_{eff}/T. This is quite counterintuitive. If M_{eff} would simply represent the saturation magnetization of a ferromagnetically ordering interface, the trend should be opposite. Since an ordering temperature of around 10 K is expected, this points to a different interpretation of M_{eff}, which may not be surprising, since the AHE depens on more than the magnetization alone, with SOC to start with. It does not affect the determination of R_{xy}^{AHE} and the shape of the function used.

6.3.3. Gate tuning of the Anomalous Hall Effect

We have studied both the temperature and gate dependence of the AHE in doped samples. First, we consider the behavior of LAO/ETO/STO. All in all, the results are similar to those of previous AHE studies in the two-band regime in the oxide interfaces [36, 132, 135, 191]. The Lifshitz point [36] is located near 25 V, carri-

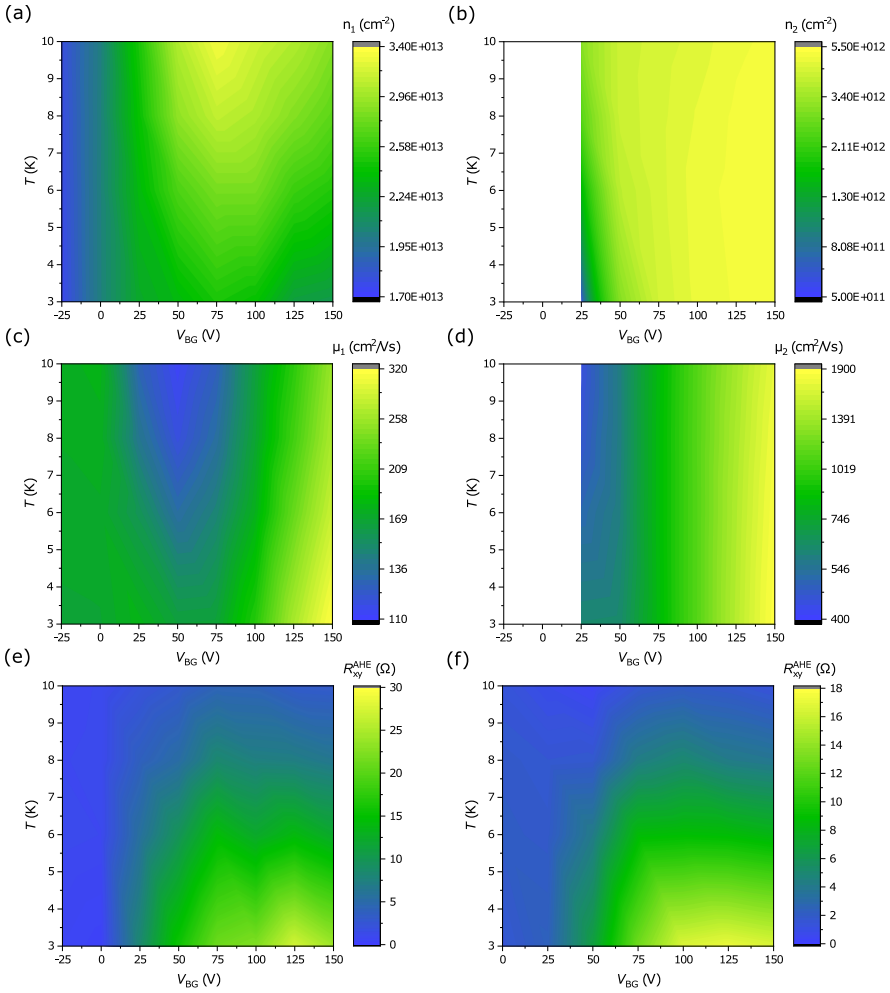

Figure 6.5: Temperature and back gate voltage dependence of (a-b) carrier concentrations, (c-d) mobilities, (e) Anomalous Hall coefficient for the LAO/ETO/STO sample. (f) Anomalous Hall coefficient for the LAO/ELTO/STO sample. The color scale for all quantities gives the range of their values.

ers of the second type appear above that voltage, see Fig. 6.5b. Unlike the carrier concentration and mobility of the low mobile carriers (Fig. 6.5a,c), the carrier concentration and mobility of the high mobile carriers (Fig. 6.5b,d) are less sensitive to a change in temperature. On the other hand, the change in voltage affects n_i and μ_i much stronger. The behavior is qualitatively the same for both samples; numbers for LAO/ELTO/STO can be found in the Appendix Fig. 6.10. The AHE disappears in the region where two-band behavior is disappearing, as would be expected in the picture where the AHE is simply controlled by the second type of carriers [96]. However, R_{xy}^{AHE} also disappears above 10 K. That can be due to vanishing of the magnetization [132], of the spin-orbit coupling (Section 3), or both. Indeed we see the signature of the weak antilocalization (WAL) indicative of spin orbit coupling in the low field *MR* in all samples. For LAO/ETO/STO this is shown in Fig. 6.6a,b and for LAO/STO and LAO/ELTO/STO in Appendix Fig. 6.11 . Note that the *MR* is strongly affected by changes in gate voltage and temperature. At the same time, the AHE coefficient is higher in the sample with higher Eu concentration. Besides that, the gate voltage and temperature dependence of the AHE coefficient for LAO/ELTO/STO (Fig. 6.5f) are similar to LAO/ETO/STO.

In STO-based interfaces, the AHE is often attributed to skew scattering [91, 96], one of the extrinsic mechanism for the AHE [100, 103, 104], in this case in the second band [91, 96]. If that mechanism is dominant, the AHE would be sensitive to changes in the scattering time. As we pointed out, the mobilities and carrier concentration do not change dramatically with temperature but change with the back gate voltage. However, we see that the mobility of the second band increases continuously with gate voltage, whereas the AHE first increases but then enters a saturation-like regime. To illustrate this, we plot R_{xy}^{AHE} versus μ_2 in Fig. 6.6c. Again that result is in agreement with [132]. Still, it is unexpected for simple skew-scattering pictures in the high mobile band, where R_{xy}^{AHE} would be proportional to the scattering time, and therefore roughly proportional to mobility (we can ignore the change of carrier mass because it does not change significantly with back gate voltage [278]). To shed more light on the mechanism responsible for the AHE, we performed a scaling analysis of the conductivity by calculating the values for σ_{xx} and σ_{xy}, as follows [151]:

$$\sigma_{xx} = \frac{R_S}{R_S^2 + R_{xy}^{AHE2}}, \quad \sigma_{xy} = \frac{R_{xy}^{AHE}}{R_S^2 + R_{xy}^{AHE2}}, \tag{6.1}$$

and then plotting them against each other. The results are shown in Fig. 6.6d for 3 K; the calculated σ_{xx} and σ_{xy} are plotted in the Appendix, Fig. 6.13, for all temperatures. We observe that σ_{xy} scales with σ_{xx} as $\sigma_{xy} \approx \sigma_{xy}^{1.8-2}$ in the region $\sigma_{xx} > 10^{-3}\ \Omega^{-1}\mathrm{m}^{-1}$. This exponent is close to the value of 1.6 observed in the scaling of ELTO metal films [151], which is often attributed to the intrinsic contribu-

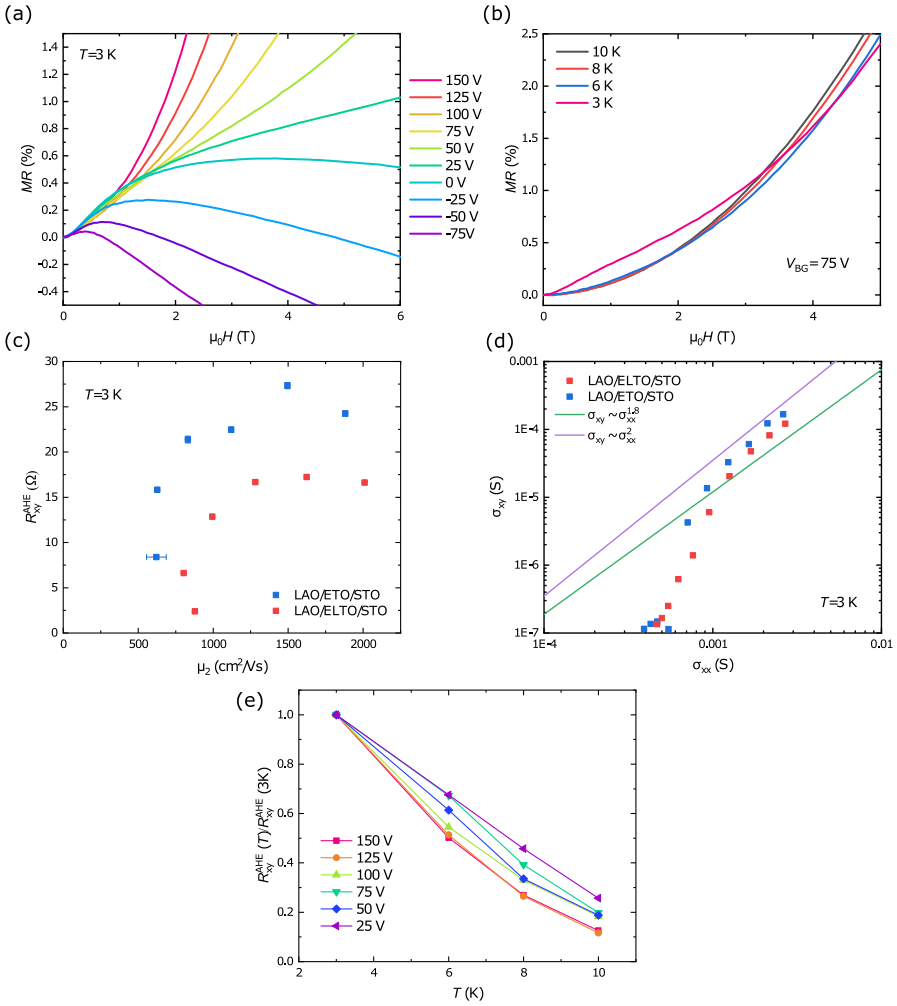

Figure 6.6: (a) Magnetoresistance *MR* with the field out of the plane at back gate voltages as indicated for LAO/ETO/STO at 3 K. (b) *MR* for LAO/ETO/STO at $V_{BG} = 75\ V$. (c) R_{xy}^{AHE} versus μ_2 for both magnetically doped samples. (d) A plot of the conductances σ_{xy} versus σ_{xx} at 3 K to investigate Scaling behavior. (e) Temperature and back gate voltage dependence of the normalized Anomalous Hall coefficient R_{xy}^{AHE} for the LAO/ELTO/STO sample.

tion to the AHE, suppressed by the disorder. Nevertheless, the meaning of scaling is somewhat limited because it corresponds to the saturation-like region, where R_{xy}^{AHE} changes less significantly than the decrease of the sheet resistance. Moreover, the interpretation of conductance scaling is often based on the ferromagnetic two-dimensional Rashba model [111, 116], where the scaling results were obtained for fixed Rashba constant. However, besides the more complex band structure in the STO-based interfaces, the Rashba constant modified with gate voltage [5, 48], as in our case can be seen from the tunable WAL effects.

A final note concerns the behavior of the fitting parameter M_{eff} in the extraction of R_{xy}^{AHE}. As seen in Appendix Fig. 6.12a,c, it shows enhancement in regions where the AHE vanishes, for instance at temperatures above 8 K and in the gate voltage range below 25 V. Most likely, the hyperbolic tangent function becomes inadequate to describe the almost flat curve. Furthermore, in most of $V_{BG} - T$ space, the ratio M_{eff}/T is only weakly temperature-dependent (Appendix Fig. 6.12b,d). Still, the point to keep in mind is that we observe the AHE in the temperature-voltage regime where the earlier studies found magnetism. A better way to establish the behavior of magnetization could be the study of the temperature dependence of the ratio $R_{xy}^{AHE}/R_{xy}^{AHE}(3\text{ K})$ because it is proportional to the temperature dependence of $M_S/M_S(3K)$ as long as carrier concentration and mobilities do not change significantly. In Fig. 6.6e, we plot $R_{xy}^{AHE}/R_{xy}^{AHE}(3\text{ K})$ at gate voltages above Lifshitz point. The ratio increases with temperature, but we do not see saturation as in Ref. [132] (note that the way in which R_{xy}^{AHE} is extracted in Ref. [132], by simple linear extrapolation, is different from ours). The temperature dependence of $R_{xy}^{AHE}/R_{xy}^{AHE}(3\text{ K})$ changes from linear at 25 V to upward curving at higher voltages. Still, as it shows a clear increase from roughly 0, it can be a signature of ferromagnetic behavior.

6.3.4. The Kondo regime in resistance

By decreasing the gate voltage below 25 V, where the AHE and the second band carrier concentration fall to zero in the magnetically doped samples, we observed the development of a minimum in the temperature dependence of the sheet resistance (Fig. 6.7a,b). That particular feature in the temperature dependence is often attributed to Kondo-like behaviour [132], which might well be connected to the magnetism of the doping layers. However, and surprisingly, we see similar behavior in nominally non-doped LAO/STO samples (Fig. 6.7c), where we do not observe AHE. It is an intriguing observation because the variation of magnetic content significantly affects the spin-polarized phase of the 2DEG, where the moment was argued to be ferromagnetically coupled with $3d_{xz/yz}$ electrons but seems not to have

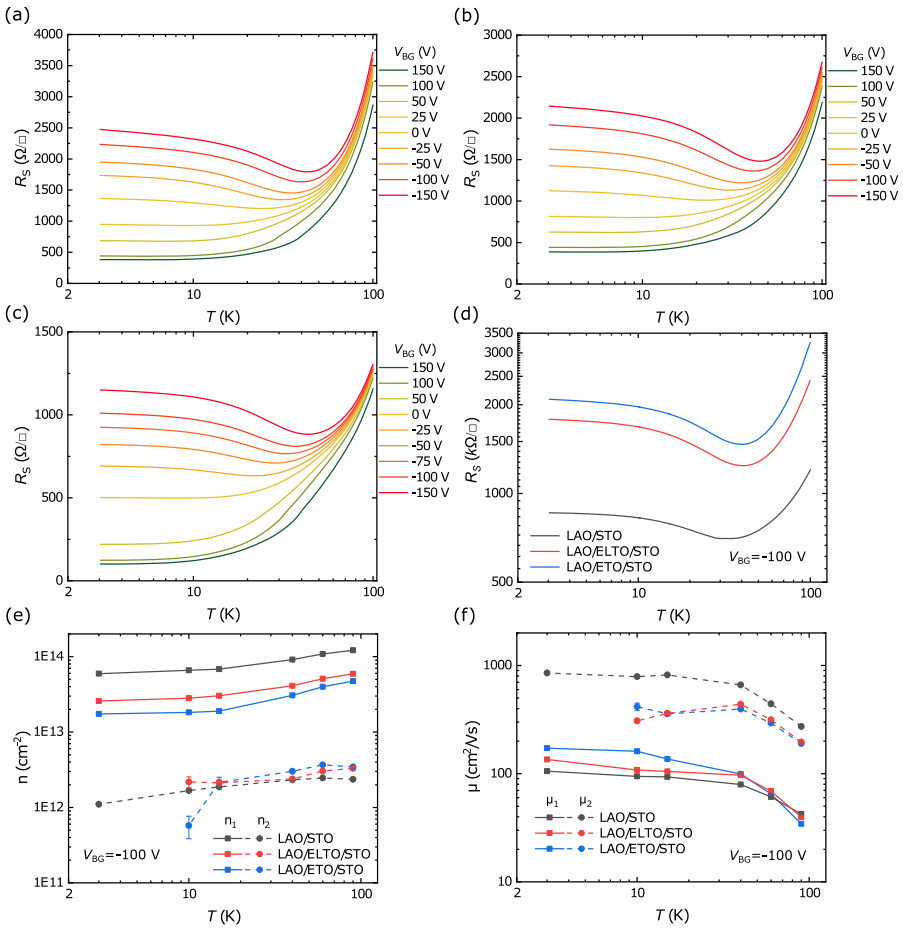

Figure 6.7: Temperature dependence of the sheet resistance R_S at different gate voltages as indicated for (a) LAO/ETO/STO, (b) LAO/ELTO/STO, and (c) LAO/STO. (d) $R_S(T)$ for all three samples measured at −100 V, (e) carrier concentration, and (f) mobility at −100 V for all three samples.

any qualitative effect on the Kondo-like regime, where moments has been argued to be antiferromagnetically coupled with $3d_{xy}$ electrons [90, 96].

To understand the nature of this behavior, we measured the temperature dependence of the sheet resistance $R_S(T)$ for all three samples at -100 V and performed magnetotransport measurements during cooldown at a few temperatures in order to find carrier concentrations and mobilities at this gate voltage. As can be seen in Fig. 6.7d, the samples show differences values of the sheet resistance but follow the same trend with a minimum around 30-40 K and saturation-like behavior below 10 K. The extracted carrier concentrations (Fig. 6.7e) from the magnetotransport data showed a constant decrease in carrier density with decreasing temperature. This is similar to the behavior of the carrier concentration of the low mobility carriers without back gate voltage, but here it is also observed for the high mobility carriers, and especially strong below 10 K. At the same time, the mobility (Fig. 6.7f) increases at first with decreasing temperature, but below 40 K saturates, in a similar way to the temperature dependence without applied back gate voltage, and can be described the same scattering picture. Important to note is that the change in the temperature dependence of the mobility happens around the temperature corresponding to the minimum in the sheet resistance.

6.4. Discussion

The results shown here are consistent with studies of LAO/ETO/STO in Ref. [132, 139, 191]. The same as in the earlier studies, we observe the MIT, the tunable AHE, the appearance of a resistance minimum and also WAL behavior. The AHE is the possible signature of ferromagnetism. Indeed, XMCD data seems to support that picture [132, 139]. Nevertheless, bulk ETO is an antiferomagnet [175–181]. It is also isostructural to STO, and, therefore, stoichiometric ETO should remain antiferromagnetic, when grown on STO [152]. At the same time, experiments revealed that antiferromagnetism only occurs for post-annealed PLD films [147, 148], and films grown by MBE [152]. Here we used PLD films without annealing, which can become ferromagnetic [147, 148, 189] because of either the formation of oxygen vacancies [147] or a longer out-of-plane lattice constant [148]. Amorphisation of ETO will also lead to the ferromagnetism [190], but in the films we studied, we do not observe, from the RHEED patterns and the intensity variations, signatures of amorphization in the films with thickness below 4 u.c. The doping with La [145, 151, 192] or oxygen deficiency [151] can also turn ETO into a ferromagnetic metal. However, the observed MIT and its weak sensitivity to the La content indicate that the occurrence of the AHE has a more complicated background than just due to

ferromagnetism induced by off-stochiometry in the ETO layer. Ref. [91] observed variations of the AHE with changes in the oxygen pressure used during the growth and proposed an indirect connection between the AHE and magnetism induced by Sr vacancies rather than with external magnetic moments, including Ti^{3+} induced by oxygen vacancies. However, we used the same growth pressure for the non-doped LAO/STO sample and LAO/E(L)TO/STO, so the variation of Sr vacancies should not be too high from sample to sample. With increasing Eu content, we observe an increase of the AHE magnitude contrary to Ref. [91]. Refs. [90, 96] proposed a ferromagnetic coupling of $3d_{xz/yz}$ with localized magnetic moments such as Ti^{3+} formed due to oxygen vacancies. That indeed can explain the observation of AHE above Lifshitz point, since skew-scattering of $3d_{xz/yz}$ carriers seems to be a dominant contribution to the AHE in oxide interfaces in the two-band regime [91, 96, 132, 133]. Nevertheless, it appears to be not straightforward to explain our results on the tunable AHE. First, the AHE coefficient does not scale linearly with mobility of high mobile carriers. Second, and probably more importantly, our non-doped LAO/STO sample does not exhibit an AHE, despite the presence of $3d_{xz/yz}$ carriers. All in all, there are certainly multiple ways to induce magnetization and AHE, but in our samples magnetic doping is the main one.

In the framework of magnetic doping, we have further indication indication that the picture of magnetic interactions based purely on the symmetry of orbitals does not hold, specifically from the data in the negative gate voltage range, where the AHE vanishes. The authors of Ref. [90, 96] argued that the coupling between mobile $3d_{xy}$ electrons and localized magnetic moments is antiferromagnetic. Strong support of this picture came from the behavior of the negative in-plane *MR*. Above the Lifshitz point, the observed large drop of (negative) in-plane *MR* was attributed to the destruction of Kondo-screening and polarisations of magnetic moments with applied field [90, 96, 97]. However, that picture was challenged by Diez *et al.* [98] who found that the negative in-plane *MR* survives up to 20 K, opposite to the expectations from the temperature-dependent Kondo picture. Furthermore, single-particle Boltzmann transport theory was sufficient to reproduce the large negative *MR* by taking into the account finite-range electrostatic impurity scattering, the anisotropic Fermi surface above the Lifshitz transition and the SOC.

In this work, we also further challenge the Kondo picture. The experiments on the LAO/STO interface performed in Ref. [99] showed that the resistance minimum could be controlled by applying hydrostatic pressure. They concluded that impurity scattering, the pressure, and the temperature dependence of the STO dielectric constant plus thermally activated charge trapping are the mechanism responsi-

ble for the resistance minimum. Although we studied the back gate voltage dependence of the sheet resistance in this work, our result can be interpreted in a somewhat similar manner. At negative gate voltages, the carrier concentration decreases in the whole temperature range, but down to 40-50 K the mobility enhances due to a decrease of electron-electron scattering. Taken together, that is the reason why we observe a decrease in the resistance down to a minimum temperature. However, with a further decrease in temperature, the change in mobility is much less steep due to various scattering mechanisms coming into play, as discussed in Sec. 6.3.2. Simultaneously, the decrease of the carrier concentration is continuous and especially pronounced for the high mobility carriers. It is not surprising then that in this region the sheet resistance starts to grow again.

Two mechanisms are responsible for the decrease in the carrier concentration. One is charge trapping [54, 55], which is less effective at high temperatures than at low temperatures. Second and probably dominant here is the complex behavior of the electric permittivity of the STO single crystal substrate at low temperatures. Indeed, at high temperatures above 40 K, the permittivity hardly changes with the applied electric field, but it does change significantly at lower temperature [279–281]. It means that the effect of back gating will be significantly more efficient in the low-temperature region. Furthermore, it is well known that back gate experiments significantly affect the carrier concentration of the second type of carriers [36, 59] at low temperatures. Below 10 K, a back gate voltage depletes, or almost depletes, the second band; therefore the saturation-like behavior in this range can be explained by the much weaker change in the mobility and carrier concentration of the low mobile carriers with temperature. Note, that our results do not exclude a possibility to induce the Kondo effect at the LAO/STO interface, but only indicate that in the back gate geometry, other effects are dominant and responsible for the resistance minimum in the temperature dependence when it occurs after the application of a gate voltage.

6.5. Conclusion

In conclusion, we have studied the LAO/STO interface with and without an inserted magnetic delta-doping layer of $Eu_{1-x}La_xTiO_3$. Our experimental results are partially in agreement with previous research on these structures [132, 139, 191]. We observe that, despite the substitution of Lanthanum for Europium, the MIT happens at 2 u.c. Moreover, the AHE is indeed induced by inserting the 2 u.c. of ETO or ELTO, and can be gate tuned. Furthermore, as an important part of our message, we find that the minimum in the sheet resistance as function of tem-

perature, found at negative back gate voltages, and which previously has been attributed to Kondo-like behavior, rather arises from the behavior of the the carrier concentrations and mobilities of both conduction bands, and is most probably due to spinless scattering mechanisms, charge trapping, and the complex temperature and electric field dependence of the STO permittivity.

6.6. Appendix

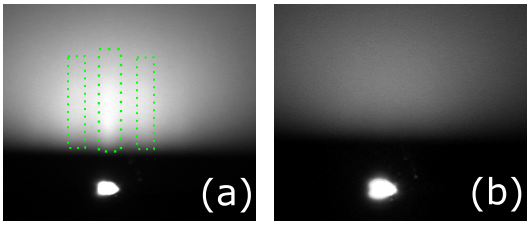

Figure 6.8: RHEED pattern after deposition of ELTO at different laser fluences F and oxygen/argoon pressures; (a) $F = 1.54$ J/cm^2, $P_{O_2} = 1 \times 10^{-4}$, $T = 800$ °C (dotted lines are guides to the eye) and (b) $F = 1.1$ J/cm^2, $P_{Ar+O_2} = 1 \times 10^{-4}$, $T = 750$ °C.

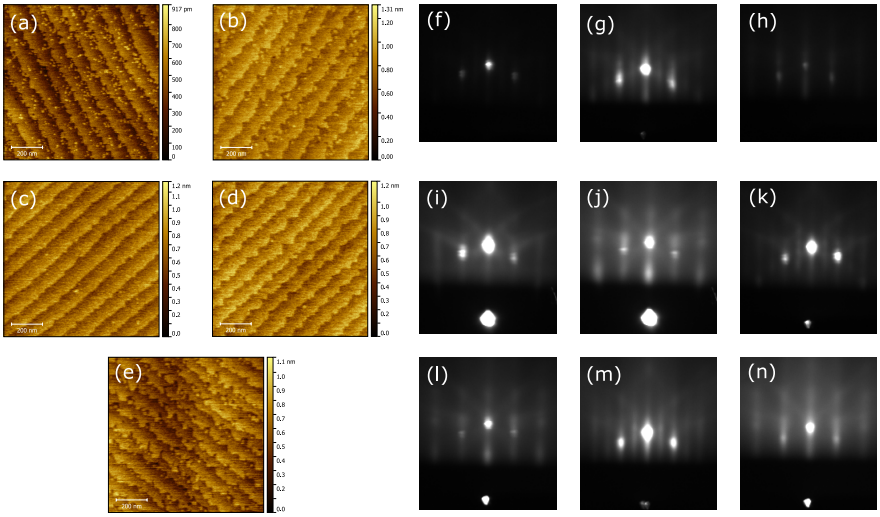

Figure 6.9: Atomic Force Microscopy (AFM) images of various sample surfaces after growth. The numerals denote the number of unit cells. (a) ELTO(4)/STO, (b) LAO/ELTO(4)/STO, (c) LAO/ETO(2)/STO, (d) LAO/ETO(3)/STO, and (e) LAO/ETO(4)/STO. RHEED patterns after deposition (f) ELTO(4)/STO, (g) and (h) LAO/ELTO(4)/STO for ELTO and LAO layers, respectively; (i) and (j) LAO/ETO(2)/STO for ETO and LAO layers respectively; (k) and (l) LAO/ETO(3)/STO for ETO and LAO layers respectively; (m) and (n) LAO/ETO(4)/STO for ETO and LAO layers, respectively.

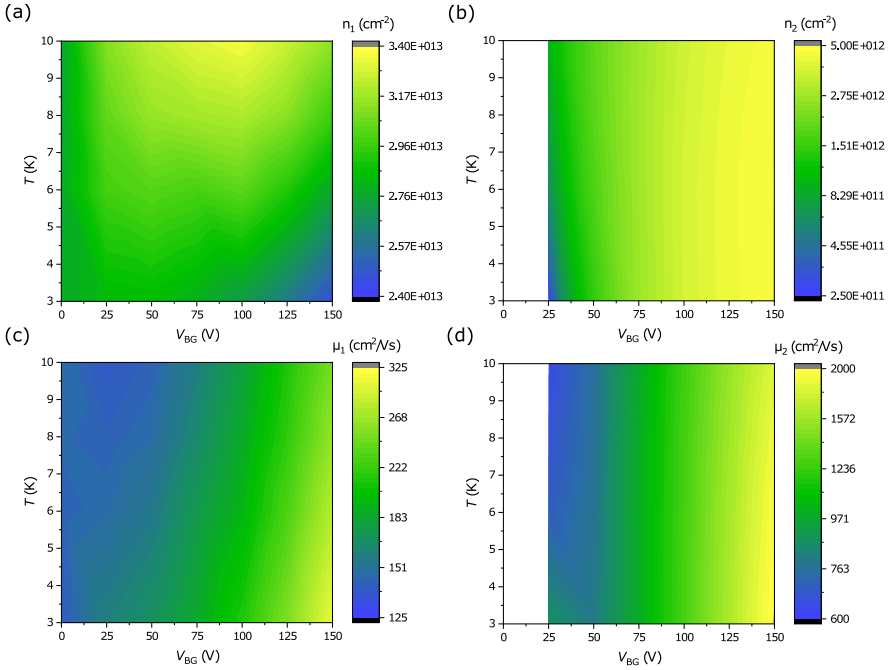

Figure 6.10: Temperature and back gate voltage dependence of (a-b) carrier concentrations and (c-d) mobilities for the LAO/ELTO/STO sample. The color scale for all quantities gives the range of their values.

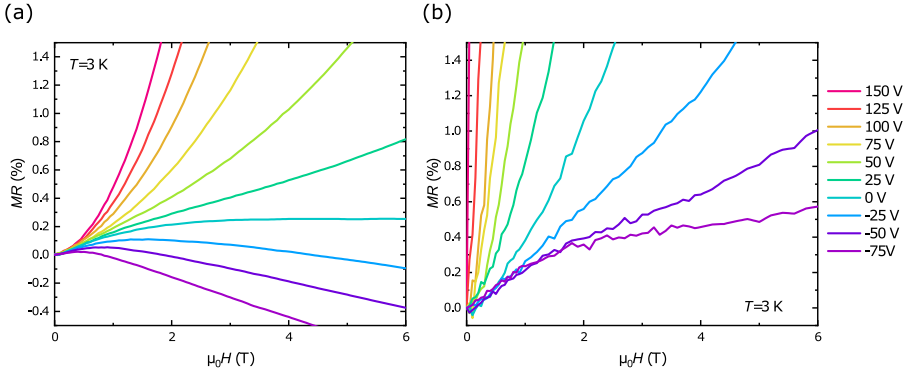

Figure 6.11: Magnetoresistance *MR* with the field out of the plane at various back gate voltages as indicated for (a) the LAO/ELTO/STO sample and (b) the LAO/STO sample at 3 K.

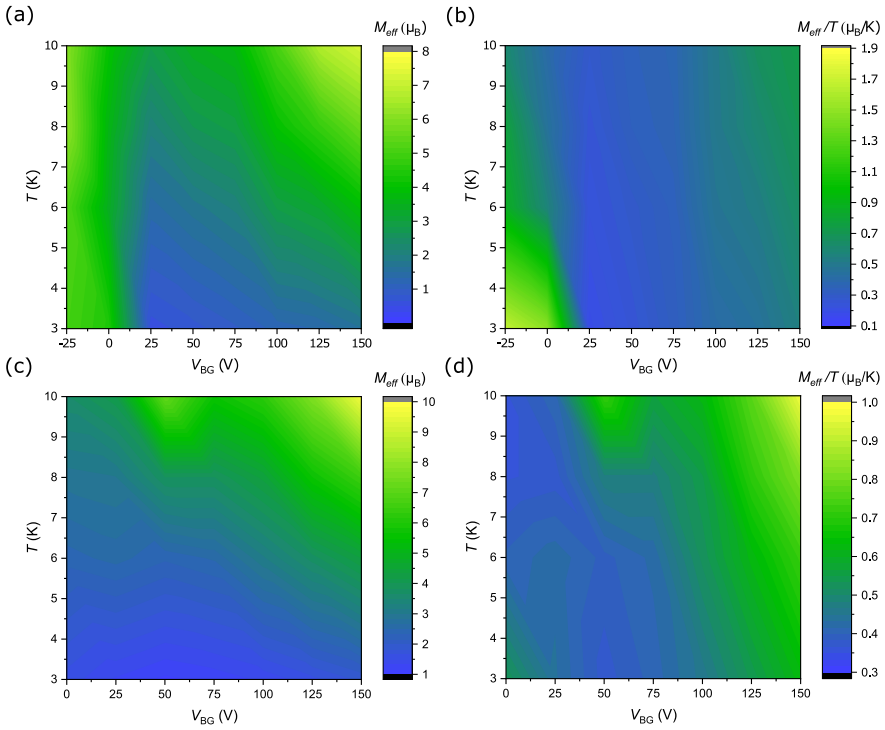

Figure 6.12: Temperature and back gate voltage dependence of the fit parameter M_{eff} for (a-b) the LAO/ETO/STO sample and (c-d) the LAO/ELTO/STO sample.

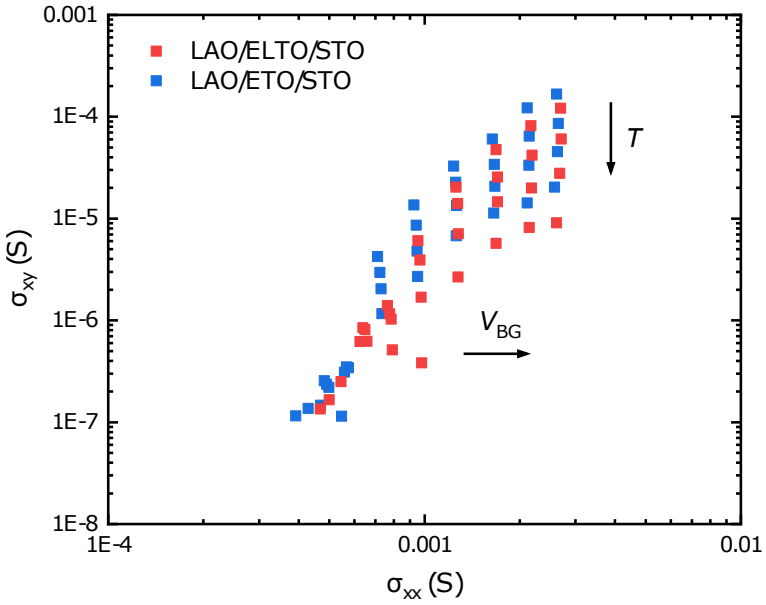

Figure 6.13: Plot of σ_{xy} versus σ_{xx} for the LAO/ETO/STO sample in order to analyze conductance scaling. Note that trend of a decrease of σ_{xy} with increasing temperature is followed poorly in the region $\sigma_{xx} < 8 \times 10^{-4}\ \Omega^{-1}\ \mathrm{m}^{-1}$.

Bibliography

[1] S. Datta and B. Das. *Electronic Analog of the Electro-Optic Modulator*. Applied Physics Letters **56**, 665–667 (1990).

[2] A. Ohtomo and H. Y. Hwang. *A High-Mobility Electron Gas at the $LaAlO_3$/$SrTiO_3$ Heterointerface*. Nature **427**, 423–426 (2004).

[3] N. Reyren, S. Thiel, A. D. Caviglia, L. F. Kourkoutis, G. Hammerl, C. Richter, C. W. Schneider, T. Kopp, A.-S. Rüetschi, D. Jaccard, M. Gabay, D. A. Muller, J.-M. Triscone, and J. Mannhart. *Superconducting Interfaces Between Insulating Oxides*. Science **317**, 1196–1199 (2007).

[4] A. D. Caviglia, S. Gariglio, N. Reyren, D. Jaccard, T. Schneider, M. Gabay, S. Thiel, G. Hammerl, J. Mannhart, and J.-M. Triscone. *Electric Field Control of the $LaAlO_3$/$SrTiO_3$ Interface Ground State*. Nature **456**, 624 (2008).

[5] A. D. Caviglia, M. Gabay, S. Gariglio, N. Reyren, C. Cancellieri, and J.-M. Triscone. *Tunable Rashba Spin-Orbit Interaction at Oxide Interfaces*. Phys. Rev. Lett. **104**, 126803 (2010).

[6] J. A. Bert, B. Kalisky, C. Bell, M. Kim, Y. Hikita, H. Y. Hwang, and K. A. Moler. *Direct Imaging of the Coexistence of Ferromagnetism and Superconductivity at the $LaAlO_3$/$SrTiO_3$ Interface*. Nature Physics **7**, 767–771 (2011).

[7] L. Li, C. Richter, J. Mannhart, and R. C. Ashoori. *Coexistence of Magnetic Order and Two-Dimensional Superconductivity at $LaAlO_3$/$SrTiO_3$ Interfaces*. Nature Physics **7**, 762 (2011).

[8] D. A. Dikin, M. Mehta, C. W. Bark, C. M. Folkman, C. B. Eom, and V. Chandrasekhar. *Coexistence of Superconductivity and Ferromagnetism in Two Dimensions*. Phys. Rev. Lett. **107**, 056802 (2011).

[9] T. Ihn. *Semiconductor Nanostructures: Quantum States and Electronic Transport*. (Oxford University Press, Oxford, 2009).

[10] Y. A. Bychkov and E. I. Rashba. *Properties of a 2D Electron Gas with Lifted Spectral Degeneracy*. Soviet Journal of Experimental and Theoretical Physics Letters **39**, 78 (1984).

[11] Y. A. Bychkov and E. I. Rashba. *Oscillatory Effects and the Magnetic Susceptibility of Carriers in Inversion Layers*. Journal of Physics C: Solid State Physics **17**, 6039–6045 (1984).

[12] G. Herranz, G. Singh, N. Bergeal, A. Jouan, J. Lesueur, J. Gázquez, M. Varela, M. Scigaj, N. Dix, F. Sánchez, and J. Fontcuberta. *Engineering Two-Dimensional Superconductivity and Rashba Spin-Orbit Coupling in $LaAlO_3/SrTiO_3$ Quantum Wells by Selective Orbital Occupancy*. Nature Communications **6**, 6028 (2015).

[13] S.-G. Lim, S. Kriventsov, T. N. Jackson, J. H. Haeni, D. G. Schlom, A. M. Balbashov, R. Uecker, P. Reiche, J. L. Freeouf, and G. Lucovsky. *Dielectric Functions and Optical Bandgaps of High-K Dielectrics for Metal-Oxide-Semiconductor Field-Effect Transistors by Far Ultraviolet Spectroscopic Ellipsometry*. Journal of Applied Physics **91**, 4500–4505 (2002).

[14] M. Cardona. *Optical Properties and Band Structure of $SrTiO_3$ and $BaTiO_3$*. Phys. Rev. **140**, A651–A655 (1965).

[15] L. F. Mattheiss. *Energy Bands for $KNiF_3$, $SrTiO_3$, $KMoO_3$, and $KTaO_3$*. Phys. Rev. B **6**, 4718–4740 (1972).

[16] H. Unoki and T. Sakudo. *Electron Spin Resonance of Fe^{3+} in $SrTiO_3$ with Special Reference to the 110°K Phase Transition*. Journal of the Physical Society of Japan **23**, 546–552 (1967).

[17] R. A. Cowley. *The Phase Transition of Strontium Titanate*. Philosophical Transactions: Mathematical, Physical and Engineering Sciences **354**, 2799–2814 (1996).

[18] N. Nakagawa, H. Y. Hwang, and D. A. Muller. *Why Some Interfaces Cannot Be Sharp*. Nature Materials **5**, 204–209 (2006).

[19] S. Gariglio, M. Gabay, and J.-M. Triscone. *Research Update: Conductivity and Beyond at the $LaAlO_3/SrTiO_3$ Interface*. APL Materials **4**, 060701 (2016).

[20] S. Thiel, G. Hammerl, A. Schmehl, C. W. Schneider, and J. Mannhart. *Tunable Quasi-Two-Dimensional Electron Gases in Oxide Heterostructures*. Science **313**, 1942–1945 (2006).

[21] L. Yu and A. Zunger. *A Polarity-Induced Defect Mechanism for Conductivity and Magnetism at Polar-Nonpolar Oxide Interfaces*. Nature Communications **5**, 5118 (2014).

[22] P. R. Willmott, S. A. Pauli, R. Herger, C. M. Schlepütz, D. Martoccia, B. D. Patterson, B. Delley, R. Clarke, D. Kumah, C. Cionca, and Y. Yacoby. *Structural Basis for the Conducting Interface between $LaAlO_3$ and $SrTiO_3$*. Phys. Rev. Lett. **99**, 155502 (2007).

[23] G. Herranz, M. Basletić, M. Bibes, C. Carrétéro, E. Tafra, E. Jacquet, K. Bouzehouane, C. Deranlot, A. Hamzić, J.-M. Broto, A. Barthélémy, and A. Fert. *High Mobility in $LaAlO_3/SrTiO_3$ Heterostructures: Origin, Dimensionality, and Perspectives*. Phys. Rev. Lett. **98**, 216803 (2007).

[24] A. Kalabukhov, R. Gunnarsson, J. Börjesson, E. Olsson, T. Claeson, and D. Winkler. *Effect of Oxygen Vacancies in the $SrTiO_3$ Substrate on the Electrical Properties of the $LaAlO_3$/$SrTiO_3$ Interface*. Phys. Rev. B **75**, 121404 (2007).

[25] Z. Q. Liu, C. J. Li, W. M. Lü, X. H. Huang, Z. Huang, S. W. Zeng, X. P. Qiu, L. S. Huang, A. Annadi, J. S. Chen, J. M. D. Coey, T. Venkatesan, and Ariando. *Origin of the Two-Dimensional Electron Gas at $LaAlO_3$/$SrTiO_3$ Interfaces: The Role of Oxygen Vacancies and Electronic Reconstruction*. Phys. Rev. X **3**, 021010 (2013).

[26] Y. Chen, N. Pryds, J. E. Kleibeuker, G. Koster, J. Sun, E. Stamate, B. Shen, G. Rijnders, and S. Linderoth. *Metallic and Insulating Interfaces of Amorphous $SrTiO_3$-Based Oxide Heterostructures*. Nano Letters **11**, 3774–3778 (2011).

[27] L. W. van Heeringen, G. A. de Wijs, A. McCollam, J. C. Maan, and A. Fasolino. *$k\cdot p$ Subband Structure of the $LaAlO_3$/$SrTiO_3$ Interface*. Phys. Rev. B **88**, 205140 (2013).

[28] Z. Zhong, A. Tóth, and K. Held. *Theory of Spin-Orbit Coupling at $LaAlO_3$/$SrTiO_3$ Interfaces and $SrTiO_3$ Surfaces*. Phys. Rev. B **87**, 161102 (2013).

[29] A. Janotti, D. Steiauf, and C. G. Van de Walle. *Strain Effects on the Electronic Structure of $SrTiO_3$: Toward High Electron Mobilities*. Phys. Rev. B **84**, 201304 (2011).

[30] R. Bistritzer, G. Khalsa, and A. H. MacDonald. *Electronic Structure of Doped d^0 Perovskite Semiconductors*. Phys. Rev. B **83**, 115114 (2011).

[31] A. E. M. Smink. *Manifold Field Effects at a Complex Oxide Interface*. PhD thesis (2019).

[32] L. W. van Heeringen, A. McCollam, G. A. de Wijs, and A. Fasolino. *Theoretical Models of Rashba Spin Splitting in Asymmetric $SrTiO_3$-Based Heterostructures*. Phys. Rev. B **95**, 155134 (2017).

[33] M. Salluzzo, J. C. Cezar, N. B. Brookes, V. Bisogni, G. M. De Luca, C. Richter, S. Thiel, J. Mannhart, M. Huijben, A. Brinkman, G. Rijnders, and G. Ghiringhelli. *Orbital Reconstruction and the Two-Dimensional Electron Gas at the $LaAlO_3$/$SrTiO_3$ Interface*. Phys. Rev. Lett. **102**, 166804 (2009).

[34] G. Khalsa and A. H. MacDonald. *Theory of the $SrTiO_3$ Surface State Two-Dimensional Electron Gas*. Phys. Rev. B **86**, 125121 (2012).

[35] P. D. C. King, S. McKeown Walker, A. Tamai, A. de la Torre, T. Eknapakul, P. Buaphet, S.-K. Mo, W. Meevasana, M. S. Bahramy, and F. Baumberger. *Quasiparticle Dynamics and Spin-Orbital Texture of the $SrTiO_3$ Two-Dimensional Electron Gas*. Nature Communications **5**, 3414 (2014).

[36] A. Joshua, S. Pecker, J. Ruhman, E. Altman, and S. Ilani. *A Universal Critical Density Underlying the Physics of Electrons at the $LaAlO_3$/$SrTiO_3$ Interface*. Nature Communications **3**, 1129 (2012).

[37] A. E. M. Smink, J. C. de Boer, M. P. Stehno, A. Brinkman, W. G. van der Wiel, and H. Hilgenkamp. *Gate-Tunable Band Structure of the $LaAlO_3-SrTiO_3$ Interface*. Phys. Rev. Lett. **118**, 106401 (2017).

[38] B. L. Altshuler, D. Khmel'nitzkii, A. I. Larkin, and P. A. Lee. *Magnetoresistance and Hall Effect in a Disordered Two-Dimensional Electron Gas*. Phys. Rev. B **22**, 5142–5153 (1980).

[39] Y. Araki, G. Khalsa, and A. H. MacDonald. *Weak Localization, Spin Relaxation, and Spin Diffusion: Crossover Between Weak and Strong Rashba Coupling Limits*. Phys. Rev. B **90**, 125309 (2014).

[40] C. Beenakker and H. van Houten, *Quantum Transport in Semiconductor Nanostructures*, in *Semiconductor heterostructures and nanostructures*, Vol. 44, edited by H. Ehrenreich and D. Turnbull, Solid State Physics (Academic Press, 1991), pp. 1 –228.

[41] S. Hikami, A. I. Larkin, and Y. Nagaoka. *Spin-Orbit Interaction and Magnetoresistance in the Two Dimensional Random System*. Progress of Theoretical Physics **63**, 707–710 (1980).

[42] G. Bergmann. *Weak Anti-Localization - An Experimental Proof for the Destructive Interference of Rotated Spin* 1/2. Solid State Communications **42**, 815 –817 (1982).

[43] P. Seiler, E. Lettl, D. Braak, and T. Kopp. *Weak Antilocalization within a Genuine Multiband Model*. Phys. Rev. B **100**, 115415 (2019).

[44] D. Stornaiuolo, S. Gariglio, A. Fête, M. Gabay, D. Li, D. Massarotti, and J.-M. Triscone. *Weak Localization and Spin-Orbit Interaction in Side-Gate Field Effect Devices at the $LaAlO_3$/$SrTiO_3$ Interface*. Phys. Rev. B **90**, 235426 (2014).

[45] S. Hurand, A. Jouan, C. Feuillet-Palma, G. Singh, J. Biscaras, E. Lesne, N. Reyren, A. Barthélémy, M. Bibes, J. E. Villegas, C. Ulysse, X. Lafosse, M. Pannetier-Lecoeur, S. Caprara, M. Grilli, J. Lesueur, and N. Bergeal. *Field-Effect Control of Superconductivity and Rashba Spin-Orbit Coupling in Top-Gated $LaAlO_3$/$SrTiO_3$ Devices*. Scientific Reports **5**, 12751 (2015).

[46] C. Yin, P. Seiler, L. M. K. Tang, I. Leermakers, N. Lebedev, U. Zeitler, and J. Aarts. *Tuning Rashba Spin-Orbit Coupling at $LaAlO_3$/$SrTiO_3$ Interfaces by Band Filling*. Phys. Rev. B **101**, 245114 (2020).

[47] M. Ben Shalom, M. Sachs, D. Rakhmilevitch, A. Palevski, and Y. Dagan. *Tuning Spin-Orbit Coupling and Superconductivity at the $SrTiO_3$/$LaAlO_3$ Interface: A Magnetotransport Study*. Phys. Rev. Lett. **104**, 126802 (2010).

[48] H. Liang, L. Cheng, L. Wei, Z. Luo, G. Yu, C. Zeng, and Z. Zhang. *Non-monotonically Tunable Rashba Spin-Orbit Coupling by Multiple-Band Filling Control in $SrTiO_3$-Based Interfacial d-Electron Gases*. Phys. Rev. B **92**, 075309 (2015).

[49] E. Lesne, Y. Fu, S. Oyarzun, J. C. Rojas-Sánchez, D. C. Vaz, H. Naganuma, G. Sicoli, J.-P. Attané, M. Jamet, E. Jacquet, J.-M. George, A. Barthélémy, H. Jaffrès, A. Fert, M. Bibes, and L. Vila. *Highly Efficient and Tunable Spin-to-Charge Conversion through Rashba Coupling at Oxide Interfaces*. Nature Materials **15**, 1261 (2016).

[50] H. Nakamura, T. Koga, and T. Kimura. *Experimental Evidence of Cubic Rashba Effect in an Inversion-Symmetric Oxide*. Phys. Rev. Lett. **108**, 206601 (2012).

[51] A. E. M. Smink, M. P. Stehno, J. C. de Boer, A. Brinkman, W. G. van der Wiel, and H. Hilgenkamp. *Correlation between Superconductivity, Band Filling, and Electron Confinement at the $LaAlO_3$/$SrTiO_3$ Interface*. Phys. Rev. B **97**, 245113 (2018).

[52] C. Bell, S. Harashima, Y. Kozuka, M. Kim, B. G. Kim, Y. Hikita, and H. Y. Hwang. *Dominant Mobility Modulation by the Electric Field Effect at the $LaAlO_3$/$SrTiO_3$ Interface*. Phys. Rev. Lett. **103**, 226802 (2009).

[53] Z. Chen, H. Yuan, Y. Xie, D. Lu, H. Inoue, Y. Hikita, C. Bell, and H. Y. Hwang. *Dual-Gate Modulation of Carrier Density and Disorder in an Oxide Two-Dimensional Electron System*. Nano Letters **16**, 6130–6136 (2016).

[54] J. Biscaras, S. Hurand, C. Feuillet-Palma, A. Rastogi, R. C. Budhani, N. Reyren, E. Lesne, J. Lesueur, and N. Bergeal. *Limit of the Electrostatic Doping in Two-Dimensional Electron Gases of $LaXO_3$(X = Al, Ti)/$SrTiO_3$*. Scientific Reports **4**, 6788 (2014).

[55] C. Yin, A. E. M. Smink, I. Leermakers, L. M. K. Tang, N. Lebedev, U. Zeitler, W. G. van der Wiel, H. Hilgenkamp, and J. Aarts. *Electron Trapping Mechanism in $LaAlO_3$/$SrTiO_3$ Heterostructures*. Phys. Rev. Lett. **124**, 017702 (2020).

[56] M. Hosoda, Y. Hikita, H. Y. Hwang, and C. Bell. *Transistor Operation and Mobility Enhancement in Top-Gated $LaAlO_3$/$SrTiO_3$ Heterostructures*. Applied Physics Letters **103**, 103507 (2013).

[57] N. Reyren, S. Gariglio, A. D. Caviglia, D. Jaccard, T. Schneider, and J.-M. Triscone. *Anisotropy of the Superconducting Transport Properties of the $LaAlO_3$/$SrTiO_3$ Interface*. Applied Physics Letters **94**, 112506 (2009).

[58] G. Singh, A. Jouan, L. Benfatto, F. Couëdo, P. Kumar, A. Dogra, R. C. Budhani, S. Caprara, M. Grilli, E. Lesne, A. Barthélémy, M. Bibes, C. Feuillet-Palma, J. Lesueur, and N. Bergeal. *Competition between Electron Pairing and Phase Coherence in Superconducting Interfaces*. Nature Communications **9**, 407 (2018).

[59] J. Biscaras, N. Bergeal, S. Hurand, C. Grossetête, A. Rastogi, R. C. Budhani, D. LeBoeuf, C. Proust, and J. Lesueur. *Two-Dimensional Superconducting Phase in $LaTiO_3$/$SrTiO_3$ Heterostructures Induced by High-Mobility Carrier Doping*. Phys. Rev. Lett. **108**, 247004 (2012).

[60] S. Hurand, A. Jouan, C. Feuillet-Palma, G. Singh, E. Lesne, N. Reyren, A. Barthélémy, M. Bibes, J. E. Villegas, C. Ulysse, M. Pannetier-Lecoeur, M. Malnou, J. Lesueur, and N. Bergeal. *Top-Gated Field-Effect $LaAlO_3$/$SrTiO_3$ Devices Made by Ion-Irradiation*. Applied Physics Letters **108**, 052602 (2016).

[61] G. E. D. K. Prawiroatmodjo, F. Trier, D. V. Christensen, Y. Chen, N. Pryds, and T. S. Jespersen. *Evidence of Weak Superconductivity at the Room-Temperature Grown $LaAlO_3$/$SrTiO_3$ Interface*. Phys. Rev. B **93**, 184504 (2016).

[62] S. Caprara, M. Grilli, L. Benfatto, and C. Castellani. *Effective Medium Theory for Superconducting Layers: A Systematic Analysis Including Space Correlation Effects*. Phys. Rev. B **84**, 014514 (2011).

[63] N. Scopigno, D. Bucheli, S. Caprara, J. Biscaras, N. Bergeal, J. Lesueur, and M. Grilli. *Phase Separation from Electron Confinement at Oxide Interfaces*. Phys. Rev. Lett. **116**, 026804 (2016).

[64] S. Caprara, J. Biscaras, N. Bergeal, D. Bucheli, S. Hurand, C. Feuillet-Palma, A. Rastogi, R. C. Budhani, J. Lesueur, and M. Grilli. *Multiband Superconductivity and Nanoscale Inhomogeneity at Oxide Interfaces*. Phys. Rev. B **88**, 020504 (2013).

[65] Ariando, X. Wang, G. Baskaran, Z. Q. Liu, J. Huijben, J. B. Yi, A. Annadi, A. R. Barman, A. Rusydi, S. Dhar, Y. P. Feng, J. Ding, H. Hilgenkamp, and T. Venkatesan. *Electronic Phase Separation at the $LaAlO_3$/$SrTiO_3$ Interface*. Nature Communications **2**, 188 (2011).

[66] B. Kalisky, E. M. Spanton, H. Noad, J. R. Kirtley, K. C. Nowack, C. Bell, H. K. Sato, M. Hosoda, Y. Xie, Y. Hikita, C. Woltmann, G. Pfanzelt, R. Jany, C. Richter, H. Y. Hwang, J. Mannhart, and K. A. Moler. *Locally Enhanced Conductivity Due To the Tetragonal Domain Structure in $LaAlO_3$/$SrTiO_3$ Heterointerfaces*. Nature Materials **12**, 1091 (2013).

[67] H. Noad, E. M. Spanton, K. C. Nowack, H. Inoue, M. Kim, T. A. Merz, C. Bell, Y. Hikita, R. Xu, W. Liu, A. Vailionis, H. Y. Hwang, and K. A. Moler. *Variation in Superconducting Transition Temperature Due to Tetragonal Domains in Two-Dimensionally Doped $SrTiO_3$*. Phys. Rev. B **94**, 174516 (2016).

[68] M. Honig, J. A. Sulpizio, J. Drori, A. Joshua, E. Zeldov, and S. Ilani. *Local Electrostatic Imaging of Striped Domain Order in $LaAlO_3$/$SrTiO_3$*. Nature Materials **12**, 1112 (2013).

[69] H. J. H. Ma, S. Scharinger, S. W. Zeng, D. Kohlberger, M. Lange, A. Stöhr, X. R. Wang, T. Venkatesan, R. Kleiner, J. F. Scott, J. M. D. Coey, D. Koelle, and Ariando. *Local Electrical Imaging of Tetragonal Domains and Field-Induced Ferroelectric Twin Walls in Conducting $SrTiO_3$*. Phys. Rev. Lett. **116**, 257601 (2016).

[70] A. M. Goldman and N. Marković. *Superconductor-Insulator Transitions in the Two-Dimensional Limit*. Physics Today **51**, 39 (1998).

[71] V. F. Gantmakher and V. T. Dolgopolov. *Superconductor–Insulator Quantum Phase Transition*. Physics-Uspekhi **53**, 1–49 (2010).

[72] M. A. Steiner, N. P. Breznay, and A. Kapitulnik. *Approach to a Superconductor-to-Bose-Insulator Transition in Disordered Films*. Phys. Rev. B **77**, 212501 (2008).

[73] M. M. Mehta, D. A. Dikin, C. W. Bark, S. Ryu, C. M. Folkman, C. B. Eom, and V. Chandrasekhar. *Magnetic Field Tuned Superconductor-to-Insulator Transition at the $LaAlO_3$/$SrTiO_3$ Interface*. Phys. Rev. B **90**, 100506 (2014).

[74] M. M. Mehta, D. A. Dikin, C. W. Bark, S. Ryu, C. M. Folkman, C. B. Eom, and V. Chandrasekhar. *Evidence for Charge-Vortex Duality at the $LaAlO_3$/$SrTiO_3$ Interface*. Nature Communications **3**, 955 (2012).

[75] Y.-Y. Pai, A. Tylan-Tyler, P. Irvin, and J. Levy. *$LaAlO_3$/$SrTiO_3$: A Tale of Two Magnetisms*. (2016) arXiv:1610.00789.

[76] M. R. Fitzsimmons, N. W. Hengartner, S. Singh, M. Zhernenkov, F. Y. Bruno, J. Santamaria, A. Brinkman, M. Huijben, H. J. A. Molegraaf, J. de la Venta, and I. K. Schuller. *Upper Limit to Magnetism in $LaAlO_3$/$SrTiO_3$ Heterostructures*. Phys. Rev. Lett. **107**, 217201 (2011).

[77] J. M. D. Coey, M Venkatesan, and P Stamenov. *Surface Magnetism of Strontium Titanate*. Journal of Physics: Condensed Matter **28**, 485001 (2016).

[78] D. V. Christensen, Y. Frenkel, Y. Z. Chen, Y. W. Xie, Z. Y. Chen, Y. Hikita, A. Smith, L. Klein, H. Y. Hwang, N. Pryds, and B. Kalisky. *Strain-Tunable Magnetism at Oxide Domain Walls*. Nature Physics **15**, 269 (2019).

[79] A. P. Petrović, A Paré, T. R. Paudel, K Lee, S Holmes, C. H. W. Barnes, A David, T Wu, E. Y. Tsymbal, and C Panagopoulos. *Emergent Vortices at a Ferromagnetic Superconducting Oxide Interface*. New Journal of Physics **16**, 103012 (2014).

[80] A. Ron, E. Maniv, D. Graf, J.-H. Park, and Y. Dagan. *Anomalous Magnetic Ground State in an $LaAlO_3/SrTiO_3$ Interface Probed by Transport through Nanowires*. Phys. Rev. Lett. **113**, 216801 (2014).

[81] Y. Ayino, P. Xu, J. Tigre-Lazo, J. Yue, B. Jalan, and V. S. Pribiag. *Ferromagnetism and Spin-Dependent Transport at a Complex Oxide Interface*. Phys. Rev. Materials **2**, 031401 (2018).

[82] V. Guduru. *Surprising Magnetotransport in Oxide Heterostructures*. PhD thesis (2014).

[83] P. Wittlich, H. Boschker, T. Asaba, L. Li, H. M. L. Noad, C. A. Watson, K. A. Moler, D. Daraselia, D. Japaridze, A. Shengelaya, J. Wang, J. Xia, and J. Mannhart. *Exploring Possible Ferromagnetism of the $LaAlO_3/SrTiO_3$ Interface*. Phys. Rev. Materials **3**, 104418 (2019).

[84] R. Pentcheva and W. E. Pickett. *Charge Localization or Itineracy at $LaAlO_3/SrTiO_3$ Interfaces: Hole Polarons, Oxygen Vacancies, and Mobile Electrons*. Phys. Rev. B **74**, 035112 (2006).

[85] K. Janicka, J. P. Velev, and E. Y. Tsymbal. *Magnetism of $LaAlO_3/SrTiO_3$ Superlattices*. Journal of Applied Physics **103**, 07B508 (2008).

[86] N. Ganguli and P. J. Kelly. *Tuning Ferromagnetism at Interfaces between Insulating Perovskite Oxides*. Phys. Rev. Lett. **113**, 127201 (2014).

[87] G. Chen and L. Balents. *Ferromagnetism in Itinerant Two-Dimensional t_{2g} Systems*. Phys. Rev. Lett. **110**, 206401 (2013).

[88] K. Michaeli, A. C. Potter, and P. A. Lee. *Superconducting and Ferromagnetic Phases in $SrTiO_3/LaAlO_3$ Oxide Interface Structures: Possibility of Finite Momentum Pairing*. Phys. Rev. Lett. **108**, 117003 (2012).

[89] S. Banerjee, O. Erten, and M. Randeria. *Ferromagnetic Exchange, Spin-Orbit Coupling and Spiral Magnetism at the $LaAlO_3/SrTiO_3$ Interface*. Nature Physics **9**, 626–630 (2013).

[90] J. Ruhman, A. Joshua, S. Ilani, and E. Altman. *Competition between Kondo Screening and Magnetism at the $LaAlO_3/SrTiO_3$ Interface*. Phys. Rev. B **90**, 125123 (2014).

[91] F. Gunkel, C. Bell, H. Inoue, B. Kim, A. G. Swartz, T. A. Merz, Y. Hikita, S. Harashima, H. K. Sato, M. Minohara, S. Hoffmann-Eifert, R. Dittmann, and H. Y. Hwang. *Defect Control of Conventional and Anomalous Electron Transport at Complex Oxide Interfaces*. Phys. Rev. X **6**, 031035 (2016).

[92] L. Weston, X. Y. Cui, S. P. Ringer, and C. Stampfl. *Density-Functional Prediction of a Surface Magnetic Phase in $SrTiO_3$ / $LaAlO_3$ Heterostructures Induced by Al Vacancies*. Phys. Rev. Lett. **113**, 186401 (2014).

[93] N. Pavlenko, T. Kopp, and J. Mannhart. *Emerging Magnetism and Electronic Phase Separation at Titanate Interfaces*. Phys. Rev. B **88**, 201104 (2013).

[94] N. Pavlenko, T. Kopp, E. Y. Tsymbal, J. Mannhart, and G. A. Sawatzky. *Oxygen Vacancies at Titanate Interfaces: Two-Dimensional Magnetism and Orbital Reconstruction.* Phys. Rev. B **86**, 064431 (2012).

[95] A. Brinkman, M. Huijben, M. van Zalk, J. Huijben, U. Zeitler, J. C. Maan, W. G. van der Wiel, G. Rijnders, D. H. A. Blank, and H. Hilgenkamp. *Magnetic Effects at the Interface between Non-Magnetic Oxides*. Nature Materials **6**, 493 (2007).

[96] A. Joshua, J. Ruhman, S. Pecker, E. Altman, and S. Ilani. *Gate-Tunable Polarized Phase of Two-Dimensional Electrons at the $LaAlO_3$ / $SrTiO_3$ Interface*. Proceedings of the National Academy of Sciences **110**, 9633–9638 (2013).

[97] M. Ben Shalom, C. W. Tai, Y. Lereah, M. Sachs, E. Levy, D. Rakhmilevitch, A. Palevski, and Y. Dagan. *Anisotropic Magnetotransport at the $SrTiO_3$ / $LaAlO_3$ Interface*. Phys. Rev. B **80**, 140403 (2009).

[98] M. Diez, A. M. R. V. L. Monteiro, G. Mattoni, E. Cobanera, T. Hyart, E. Mulazimoglu, N. Bovenzi, C. W. J. Beenakker, and A. D. Caviglia. *Giant Negative Magnetoresistance Driven by Spin-Orbit Coupling at the $LaAlO_3$ / $SrTiO_3$ Interface*. Phys. Rev. Lett. **115**, 016803 (2015).

[99] D. Fuchs, A. Sleem, R. Schäfer, A. G. Zaitsev, M. Meffert, D. Gerthsen, R. Schneider, and H. v. Löhneysen. *Incipient Localization of Charge Carriers in the Two-Dimensional Electron System in $LaAlO_3$ / $SrTiO_3$ under Hydrostatic Pressure*. Phys. Rev. B **92**, 155313 (2015).

[100] N. Nagaosa, J. Sinova, S. Onoda, A. H. MacDonald, and N. P. Ong. *Anomalous Hall Effect*. Rev. Mod. Phys. **82**, 1539–1592 (2010).

[101] E. M. Pugh. *Hall Effect and the Magnetic Properties of Some Ferromagnetic Materials*. Phys. Rev. **36**, 1503–1511 (1930).

[102] E. M. Pugh and T. W. Lippert. *Hall e.m.f. and Intensity of Magnetization*. Phys. Rev. **42**, 709–713 (1932).

[103] J. Smit. *The Spontaneous Hall Effect in Ferromagnetics I*. Physica **21**, 877 – 887 (1955).

[104] J. Smit. *The Spontaneous Hall Effect in Ferromagnetics II*. Physica **24**, 39 –51 (1958).

[105] L. Berger. *Side-Jump Mechanism for the Hall Effect of Ferromagnets*. Phys. Rev. B **2**, 4559–4566 (1970).

[106] R. Karplus and J. M. Luttinger. *Hall Effect in Ferromagnetics*. Phys. Rev. **95**, 1154–1160 (1954).

[107] N. A. Sinitsyn, A. H. MacDonald, T. Jungwirth, V. K. Dugaev, and J. Sinova. *Anomalous Hall Effect in a Two-Dimensional Dirac Band: The Link between the Kubo-Streda Formula and the Semiclassical Boltzmann Equation Approach*. Phys. Rev. B **75**, 045315 (2007).

[108] N. A. Sinitsyn. *Semiclassical Theories of the Anomalous Hall Effect*. Journal of Physics: Condensed Matter **20**, 023201 (2007).

[109] A. Crépieux and P. Bruno. *Theory of the Anomalous Hall Effect from the Kubo Formula and the Dirac Equation*. Phys. Rev. B **64**, 014416 (2001).

[110] S. Onoda, N. Sugimoto, and N. Nagaosa. *Theory of Non-Equilibirum States Driven by Constant Electromagnetic Fields: Non-Commutative Quantum Mechanics in the Keldysh Formalism*. Progress of Theoretical Physics **116**, 61–86 (2006).

[111] S. Onoda, N. Sugimoto, and N. Nagaosa. *Quantum Transport Theory of Anomalous Electric, Thermoelectric, and Thermal Hall Effects in Ferromagnets*. Phys. Rev. B **77**, 165103 (2008).

[112] M. V. Berry. *Quantal Phase Factors Accompanying Adiabatic Changes*. Proceedings of the Royal Society of London. A. Mathematical and Physical Sciences **392**, 45–57 (1984).

[113] M.-C. Chang and Q. Niu. *Berry Phase, Hyperorbits, and the Hofstadter Spectrum: Semiclassical Dynamics in Magnetic Bloch Bands*. Phys. Rev. B **53**, 7010–7023 (1996).

[114] G. Sundaram and Q. Niu. *Wave-Packet Dynamics in Slowly Perturbed Crystals: Gradient Corrections and Berry-Phase Effects*. Phys. Rev. B **59**, 14915–14925 (1999).

[115] N. A. Sinitsyn, Q. Niu, and A. H. MacDonald. *Coordinate Shift in the Semiclassical Boltzmann Equation and the Anomalous Hall Effect*. Phys. Rev. B **73**, 075318 (2006).

[116] A. A. Kovalev, Y. Tserkovnyak, K. Výborný, and J. Sinova. *Transport Theory for Disordered Multiple-Band Systems: Anomalous Hall Effect and Anisotropic Magnetoresistance*. Phys. Rev. B **79**, 195129 (2009).

[117] D. Culcer, A. MacDonald, and Q. Niu. *Anomalous Hall Effect in Paramagnetic Two-Dimensional Systems*. Phys. Rev. B **68**, 045327 (2003).

[118] I. A. Ado, I. A. Dmitriev, P. M. Ostrovsky, and M. Titov. *Anomalous Hall Effect in a 2D Rashba Ferromagnet*. Phys. Rev. Lett. **117**, 046601 (2016).

[119] A. A. Kovalev, K. Výborný, and J. Sinova. *Hybrid Skew Scattering Regime of the Anomalous Hall Effect in Rashba Systems: Unifying Keldysh, Boltzmann, and Kubo Formalisms*. Phys. Rev. B **78**, 041305 (2008).

[120] T. Kato, Y. Ishikawa, H. Itoh, and J. ichiro Inoue. *Anomalous Hall Effect in Spin-Polarized Two-Dimensional Electron Gases with Rashba Spin–Orbit Interaction*. New Journal of Physics **9**, 350–350 (2007).

[121] M. Borunda, T. S. Nunner, T. Lück, N. A. Sinitsyn, C. Timm, J. Wunderlich, T. Jungwirth, A. H. MacDonald, and J. Sinova. *Absence of Skew Scattering in Two-Dimensional Systems: Testing the Origins of the Anomalous Hall Effect*. Phys. Rev. Lett. **99**, 066604 (2007).

[122] T. S. Nunner, N. A. Sinitsyn, M. F. Borunda, V. K. Dugaev, A. A. Kovalev, A. Abanov, C. Timm, T. Jungwirth, J.-i. Inoue, A. H. MacDonald, and J. Sinova. *Anomalous Hall Effect in a Two-Dimensional Electron Gas*. Phys. Rev. B **76**, 235312 (2007).

[123] S. Onoda, N. Sugimoto, and N. Nagaosa. *Intrinsic Versus Extrinsic Anomalous Hall Effect in Ferromagnets*. Phys. Rev. Lett. **97**, 126602 (2006).

[124] A. K. Majumdar and L. Berger. *Hall Effect and Magnetoresistance in Pure Iron, Lead, Fe-Co, and Fe-Cr Dilute Alloys*. Phys. Rev. B **7**, 4203–4220 (1973).

[125] Y. Shiomi, Y. Onose, and Y. Tokura. *Extrinsic Anomalous Hall Effect in Charge and Heat Transport in Pure Iron, $Fe_{0.997}Si_{0.003}$, and $Fe_{0.97}Co_{0.03}$*. Phys. Rev. B **79**, 100404 (2009).

[126] K. Ueno, T. Fukumura, H. Toyosaki, M. Nakano, and M. Kawasaki. *Anomalous Hall Effect in Anatase $Ti_{1-x}Co_xO_{2-\delta}$ at Low Temperature Regime*. Applied Physics Letters **90**, 072103 (2007).

[127] S. Sangiao, L. Morellon, G. Simon, J. M. De Teresa, J. A. Pardo, J. Arbiol, and M. R. Ibarra. *Anomalous Hall Effect in Fe (001) Epitaxial Thin Films over a Wide Range in Conductivity*. Phys. Rev. B **79**, 014431 (2009).

[128] A. Fernández-Pacheco, J. M. De Teresa, J. Orna, L. Morellon, P. A. Algarabel, J. A. Pardo, and M. R. Ibarra. *Universal Scaling of the Anomalous Hall Effect in Fe_3O_4 Epitaxial Thin Films*. Phys. Rev. B **77**, 100403 (2008).

[129] S. H. Chun, Y. S. Kim, H. K. Choi, I. T. Jeong, W. O. Lee, K. S. Suh, Y. S. Oh, K. H. Kim, Z. G. Khim, J. C. Woo, and Y. D. Park. *Interplay between Carrier and Impurity Concentrations in Annealed $Ga_{1-x}Mn_xAs$: Intrinsic Anomalous Hall Effect*. Phys. Rev. Lett. **98**, 026601 (2007).

[130] T. Miyasato, N. Abe, T. Fujii, A. Asamitsu, S. Onoda, Y. Onose, N. Nagaosa, and Y. Tokura. *Crossover Behavior of the Anomalous Hall Effect and Anomalous Nernst Effect in Itinerant Ferromagnets*. Phys. Rev. Lett. **99**, 086602 (2007).

[131] I. A. Ado, I. A. Dmitriev, P. M. Ostrovsky, and M. Titov. *Anomalous Hall Effect with Massive Dirac Fermions*. EPL (Europhysics Letters) **111**, 37004 (2015).

[132] D. Stornaiuolo, C. Cantoni, G. M. De Luca, R. Di Capua, E. Di. Gennaro, G. Ghiringhelli, B. Jouault, D. Marrè, D. Massarotti, F. Miletto Granozio, I. Pallecchi, C. Piamonteze, S. Rusponi, F. Tafuri, and M. Salluzzo. *Tunable Spin Polarization and Superconductivity in Engineered Oxide Interfaces*. Nature Materials **15**, 278 (2015).

[133] H. R. Zhang, Y. Zhang, H. Zhang, J. Zhang, X. Shen, X. X. Guan, Y. Z. Chen, R. C. Yu, N. Pryds, Y. S. Chen, B. G. Shen, and J. R. Sun. *Magnetic Two-Dimensional Electron Gas at the Manganite-Buffered $LaAlO_3/SrTiO_3$ Interface*. Phys. Rev. B **96**, 195167 (2017).

[134] Y. Gan, D. V. Christensen, Y. Zhang, H. Zhang, D. Krishnan, Z. Zhong, W. Niu, D. J. Carrad, K. Norrman, M. von Soosten, T. S. Jespersen, B. Shen, N. Gauquelin, J. Verbeeck, J. Sun, N. Pryds, and Y. Chen. *Diluted Oxide Interfaces with Tunable Ground States*. Advanced Materials **31**, 1805970 (2019).

[135] Y. Gan, Y. Zhang, D. V. Christensen, N. Pryds, and Y. Chen. *Gate-Tunable Rashba Spin-Orbit Coupling and Spin Polarization at Diluted Oxide Interfaces*. Phys. Rev. B **100**, 125134 (2019).

[136] Y. Zhang, Y. Gan, H. Zhang, H. Zhang, P. Norby, B. Shen, J. Sun, and Y. Chen. *Metallic Conduction and Ferromagnetism in $MAl_2O_4/SrTiO_3$ Spinel/Perovskite Heterostructures (M = Fe, Co, Ni)*. Applied Physics Letters **113**, 261603 (2018).

[137] Y. Cao, X. Liu, P. Shafer, S. Middey, D. Meyers, M. Kareev, Z. Zhong, J.-W. Kim, P. J. Ryan, E. Arenholz, and J. Chakhalian. *Anomalous Orbital Structure in a Spinel-Perovskite Interface*. npj Quantum Materials **1**, 16009 (2016).

[138] H. Zhang, X. Yan, H. Zhang, F. Wang, Y. Gu, X. Ning, T. Khan, R. Li, Y. Chen, W. Liu, S. Wang, B. Shen, and J. Sun. *Magnetic Two-Dimensional Electron Gases with High Curie Temperatures at $LaAlO_3/SrTiO_3$:Fe Interfaces*. Phys. Rev. B **97**, 155150 (2018).

[139] G. M. De Luca, R. Di Capua, E. Di Gennaro, F. M. Granozio, D. Stornaiuolo, M. Salluzzo, A. Gadaleta, I. Pallecchi, D. Marrè, C. Piamonteze, M. Radovic, Z. Ristic, and S. Rusponi. *Transport Properties of a Quasi-Two-Dimensional Electron System Formed in $LaAlO_3/EuTiO_3/SrTiO_3$ Heterostructures*. Phys. Rev. B **89**, 224413 (2014).

[140] J. Biscaras, N. Bergeal, A. Kushwaha, T. Wolf, A. Rastogi, R. C. Budhani, and J. Lesueur. *Two-dimensional Superconductivity at a Mott Insulator/Band Insulator Interface $LaTiO_3/SrTiO_3$*. Nature Communications **1**, 89 (2010).

[141] C. He, T. D. Sanders, M. T. Gray, F. J. Wong, V. V. Mehta, and Y. Suzuki. *Metal-Insulator Transitions in Epitaxial $LaVO_3$ and $LaTiO_3$ Films*. Phys. Rev. B **86**, 081401 (2012).

[142] P. Scheiderer, M. Schmitt, J. Gabel, M. Zapf, M. Stübinger, P. Schütz, L. Dudy, C. Schlueter, T.-L. Lee, M. Sing, and R. Claessen. *Tailoring Materials for Mottronics: Excess Oxygen Doping of a Prototypical Mott Insulator*. Advanced Materials **30**, 1706708.

[143] R. Aeschlimann, D. Preziosi, P. Scheiderer, M. Sing, S. Valencia, J. Santamaria, C. Luo, H. Ryll, F. Radu, R. Claessen, C. Piamonteze, and M. Bibes. *A Living-Dead Magnetic Layer at the Surface of Ferrimagnetic $DyTiO_3$ Thin Films*. Advanced Materials **30**, 1707489.

[144] M. N. Grisolia, F. Y. Bruno, D. Sando, H. J. Zhao, E. Jacquet, X. M. Chen, L. Bellaiche, A. Barthélémy, and M. Bibes. *Structural, Magnetic, and Electronic Properties of $GdTiO_3$ Mott Insulator Thin Films Grown by Pulsed Laser Deposition*. Applied Physics Letters **105**, 172402 (2014).

[145] K. S. Takahashi, M. Onoda, M. Kawasaki, N. Nagaosa, and Y. Tokura. *Control of the Anomalous Hall Effect by Doping in $Eu_{1-x}La_xTiO_3$ Thin Films*. Phys. Rev. Lett. **103**, 057204 (2009).

[146] R. Zhao, W. W. Li, L. Chen, Q. Q. Meng, J. Yang, H. Wang, Y. Q. Wang, R. J. Tang, and H. Yang. *Conduction Mechanisms of Epitaxial $EuTiO_3$ Thin Films*. Applied Physics Letters **101**, 102901 (2012).

[147] K. Shimamoto, K. Hatabayashi, Y. Hirose, S. Nakao, T. Fukumura, and T. Hasegawa. *Full Compensation of Oxygen Vacancies in $EuTiO_3$ (001) Epitaxial Thin Film Stabilized by a $SrTiO_3$ Surface Protection Layer*. Applied Physics Letters **102**, 042902 (2013).

[148] K. Fujita, N. Wakasugi, S. Murai, Y. Zong, and K. Tanaka. *High-Quality Antiferromagnetic $EuTiO_3$ Epitaxial Thin Films on $SrTiO_3$ Prepared by Pulsed Laser Deposition and Postannealing*. Applied Physics Letters **94**, 062512 (2009).

[149] A. Shkabko, C. Xu, P. Meuffels, F. Gunkel, R. Dittmann, A. Weidenkaff, and R. Waser. *Tuning Cationic Composition of La:$EuTiO_{3-\delta}$ Films*. APL Materials **1**, 052111 (2013).

[150] H.-H. Wang, A. Fleet, J. D. Brock, D. Dale, and Y. Suzuki. *Nearly Strain-Free Heteroepitaxial System for Fundamental Studies of Pulsed Laser Deposition: $EuTiO_3$ on $SrTiO_3$*. Journal of Applied Physics **96**, 5324–5328 (2004).

[151] K. S. Takahashi, H. Ishizuka, T. Murata, Q. Y. Wang, Y. Tokura, N. Nagaosa, and M. Kawasaki. *Anomalous Hall Effect Derived from Multiple Weyl Nodes in High-Mobility $EuTiO_3$ Films*. Science Advances **4** (2018) 10 . 1126 / sciadv.aar7880.

[152] J. H. Lee, X. Ke, N. J. Podraza, L. F. Kourkoutis, T. Heeg, M. Roeckerath, J. W. Freeland, C. J. Fennie, J. Schubert, D. A. Muller, P. Schiffer, and D. G. Schlom. *Optical Band Gap and Magnetic Properties of Unstrained $EuTiO_3$ Films*. Applied Physics Letters **94**, 212509 (2009).

[153] J. H. Lee, L. Fang, E. Vlahos, X. Ke, Y. W. Jung, L. F. Kourkoutis, J.-W. Kim, P. J. Ryan, T. Heeg, M. Roeckerath, V. Goian, M. Bernhagen, R. Uecker, P. C. Hammel, K. M. Rabe, S. Kamba, J. Schubert, J. W. Freeland, D. A. Muller, C. J. Fennie, P. Schiffer, V. Gopalan, E. Johnston-Halperin, and D. G. Schlom. *A Strong Ferroelectric Ferromagnet Created by Means of Spin-Lattice Coupling*. Nature **466**, 954–958 (2010).

[154] P. Moetakef, D. G. Ouellette, J. Y. Zhang, T. A. Cain, S. J. Allen, and S. Stemmer. *Growth and Properties of $GdTiO_3$ Films Prepared by Hybrid Molecular Beam Epitaxy*. Journal of Crystal Growth **355**, 166 –170 (2012).

[155] A. Ohtomo, D. A. Muller, J. L. Grazul, and H. Y. Hwang. *Epitaxial Growth and Electronic Structure of $LaTiO_x$ Films*. Applied Physics Letters **80**, 3922–3924 (2002).

[156] R. F. Need, B. J. Isaac, B. J. Kirby, J. A. Borchers, S. Stemmer, and S. D. Wilson. *Octahedral Tilt Independent Magnetism in Confined $GdTiO_3$ Films*. Applied Physics Letters **112**, 132407 (2018).

[157] H. D. Zhou and J. B. Goodenough. *Localized or Itinerant TiO_3 Electrons in $RTiO_3$ Perovskites*. Journal of Physics: Condensed Matter **17**, 7395 (2005).

[158] A. C. Komarek, H. Roth, M. Cwik, W.-D. Stein, J. Baier, M. Kriener, F. Bourée, T. Lorenz, and M. Braden. *Magnetoelastic Coupling in $RTiO_3$ (R =La, Nd, Sm, Gd, Y) Investigated with Diffraction Techniques and Thermal Expansion Measurements*. Phys. Rev. B **75**, 224402 (2007).

[159] M. Cwik, T. Lorenz, J. Baier, R. Müller, G. André, F. Bourée, F. Lichtenberg, A. Freimuth, R. Schmitz, E. Müller-Hartmann, and M. Braden. *Crystal and Magnetic Structure of $LaTiO_3$: Evidence for Nondegenerate t_{2g} Orbitals*. Phys. Rev. B **68**, 060401 (2003).

[160] J. Goral and J. Greedan. *The Magnetic Structures of $LaTiO_3$ and $CeTiO_3$*. Journal of Magnetism and Magnetic Materials **37**, 315 –321 (1983).

[161] G. I. Meijer, W. Henggeler, J. Brown, O.-S. Becker, J. G. Bednorz, C. Rossel, and P. Wachter. *Reduction of Ordered Moment in Strongly Correlated $LaTiO_{3+\delta}$ upon Band Filling*. Phys. Rev. B **59**, 11832–11836 (1999).

[162] F. J. Wong, S.-H. Baek, R. V. Chopdekar, V. V. Mehta, H.-W. Jang, C.-B. Eom, and Y. Suzuki. *Metallicity in $LaTiO_3$ Thin Films Induced by Lattice Deformation*. Phys. Rev. B **81**, 161101 (2010).

[163] R. Ohtsuka, M. Matvejeff, K. Nishio, R. Takahashi, and M. Lippmaa. *Transport Properties of $LaTiO_3$/$SrTiO_3$ Heterostructures*. Applied Physics Letters **96**, 192111 (2010).

[164] J. H. You and J. H. Lee. *Critical Thickness for the Two-Dimensional Electron Gas in $LaTiO_3$/$SrTiO_3$ Superlattices*. Phys. Rev. B **88**, 155111 (2013).

[165] B. Vilquin, T. Kanki, T. Yanagida, H. Tanaka, and T. Kawai. *Effect of Sr Doping on $LaTiO_3$ Thin Films*. Applied Surface Science **244**, 12th International Conference on Solid Films and Surfaces, 494 –497 (2005).

[166] Y. Tokura, Y. Taguchi, Y. Okada, Y. Fujishima, T. Arima, K. Kumagai, and Y. Iye. *Filling Dependence of Electronic Properties on the Verge of Metal–Mott-Insulator Transition in $Sr_{1-x}La_xTiO_3$*. Phys. Rev. Lett. **70**, 2126–2129 (1993).

[167] C. C. Hays, J.-S. Zhou, J. T. Markert, and J. B. Goodenough. *Electronic Transition in $La_{1-x}Sr_xTiO_3$*. Phys. Rev. B **60**, 10367–10373 (1999).

[168] S. Gariglio, J. W. Seo, J. Fompeyrine, J.-P. Locquet, and J.-M. Triscone. *Transport Properties in Doped Mott Insulator Epitaxial $La_{1-y}TiO_{3+\delta}$ Thin Films*. Phys. Rev. B **63**, 161103 (2001).

[169] J. Biscaras, N. Bergeal, S. Hurand, C. Feuillet-Palma, A. Rastogi, R. C. Budhani, M. Grilli, S. Caprara, and J. Lesueur. *Multiple Quantum Criticality in a Two-Dimensional Superconductor*. Nature Materials **12**, 542 (2013).

[170] M. J. Veit, R. Arras, B. J. Ramshaw, R. Pentcheva, and Y. Suzuki. *Nonzero Berry Phase in Quantum Oscillations from Giant Rashba-Type Spin Splitting in $LaTiO_3$/$SrTiO_3$ Heterostructures*. Nature Communications **9**, 1458 (2018).

[171] C. W. Turner and J. Greedan. *Ferrimagnetism in the Rare Earth Titanium (III) Oxides, $RTiO_3$; R = Gd, Tb, Dy, Ho, Er, Tm*. Journal of Solid State Chemistry **34**, 207 –213 (1980).

[172] P. Moetakef, J. Y. Zhang, A. Kozhanov, B. Jalan, R. Seshadri, S. J. Allen, and S. Stemmer. *Transport in Ferromagnetic $GdTiO_3$/$SrTiO_3$ Heterostructures*. Applied Physics Letters **98**, 112110 (2011).

[173] C. A. Jackson and S. Stemmer. *Interface-Induced Magnetism in Perovskite Quantum Wells*. Phys. Rev. B **88**, 180403 (2013).

[174] P. Moetakef, J. R. Williams, D. G. Ouellette, A. P. Kajdos, D. Goldhaber-Gordon, S. J. Allen, and S. Stemmer. *Carrier-Controlled Ferromagnetism in $SrTiO_3$*. Phys. Rev. X **2**, 021014 (2012).

[175] C.-L. Chien, S. DeBenedetti, and F. D. S. Barros. *Magnetic Properties of $EuTiO_3$, Eu_2TiO_4, and $Eu_3Ti_2O_7$*. Phys. Rev. B **10**, 3913–3922 (1974).

[176] T. R. McGuire, M. W. Shafer, R. J. Joenk, H. A. Alperin, and S. J. Pickart. *Magnetic Structure of $EuTiO_3$*. Journal of Applied Physics **37**, 981–982 (1966).

[177] J. Schiemer, L. J. Spalek, S. S. Saxena, C. Panagopoulos, T. Katsufuji, A. Bussmann-Holder, J. Köhler, and M. A. Carpenter. *Magnetic Field and in situ Stress Dependence of Elastic Behavior in $EuTiO_3$ from Resonant Ultrasound Spectroscopy*. Phys. Rev. B **93**, 054108 (2016).

[178] A. Bussmann-Holder, J. Köhler, R. K. Kremer, and J. M. Law. *Relation Between Structural Instabilities in $EuTiO_3$ and $SrTiO_3$*. Phys. Rev. B **83**, 212102 (2011).

[179] D. Bessas, K. Z. Rushchanskii, M. Kachlik, S. Disch, O. Gourdon, J. Bednarcik, K. Maca, I. Sergueev, S. Kamba, M. Ležaić, and R. P. Hermann. *Lattice Instabilities in Bulk $EuTiO_3$*. Phys. Rev. B **88**, 144308 (2013).

[180] D. S. Ellis, H. Uchiyama, S. Tsutsui, K. Sugimoto, K. Kato, D. Ishikawa, and A. Q. R. Baron. *Phonon Softening and Dispersion in $EuTiO_3$*. Phys. Rev. B **86**, 220301 (2012).

[181] T. Katsufuji and H. Takagi. *Coupling between Magnetism and Dielectric Properties in Quantum Paraelectric $EuTiO_3$*. Phys. Rev. B **64**, 054415 (2001).

[182] P. G. Reuvekamp, R. K. Kremer, J. Köhler, and A. Bussmann-Holder. *Evidence for the First-Order Nature of the Structural Instability in $EuTiO_3$ from Thermal Expansion Measurements*. Phys. Rev. B **90**, 104105 (2014).

[183] L. J. Spalek, S. S. Saxena, C. Panagopoulos, T. Katsufuji, J. A. Schiemer, and M. A. Carpenter. *Elastic and Anelastic Relaxations Associated with Phase Transitions in $EuTiO_3$*. Phys. Rev. B **90**, 054119 (2014).

[184] V. Goian, S. Kamba, O. Pacherová, J. Drahokoupil, L. Palatinus, M. Dušek, J. Rohlíček, M. Savinov, F. Laufek, W. Schranz, A. Fuith, M. Kachlík, K. Maca, A. Shkabko, L. Sagarna, A. Weidenkaff, and A. A. Belik. *Antiferrodistortive Phase Transition in $EuTiO_3$*. Phys. Rev. B **86**, 054112 (2012).

[185] M. Allieta, M. Scavini, L. J. Spalek, V. Scagnoli, H. C. Walker, C. Panagopoulos, S. S. Saxena, T. Katsufuji, and C. Mazzoli. *Role of Intrinsic Disorder in the Structural Phase Transition of Magnetoelectric $EuTiO_3$*. Phys. Rev. B **85**, 184107 (2012).

[186] Z. Guguchia, Z. Salman, H. Keller, K. Roleder, J. Köhler, and A. Bussmann-Holder. *Complexity in the Structural and Magnetic Properties of Almost Multiferroic $EuTiO_3$*. Phys. Rev. B **94**, 220406 (2016).

[187] C. J. Fennie and K. M. Rabe. *Magnetic and Electric Phase Control in Epitaxial $EuTiO_3$ from First Principles*. Phys. Rev. Lett. **97**, 267602 (2006).

[188] P. J. Ryan, J.-W. Kim, T. Birol, P. Thompson, J.-H. Lee, X. Ke, P. S. Normile, E. Karapetrova, P. Schiffer, S. D. Brown, C. J. Fennie, and D. G. Schlom. *Reversible Control of Magnetic Interactions by Electric Field in a Single-Phase Material*. Nature Communications **4**, 1334 (2013).

[189] K. Kugimiya, K. Fujita, K. Tanaka, and K. Hirao. *Preparation and Magnetic Properties of Oxygen Deficient $EuTiO_{3-\delta}$ Thin Films*. Journal of Magnetism and Magnetic Materials **310**, Proceedings of the 17th International Conference on Magnetism, 2268 –2270 (2007).

[190] H. Akamatsu, K. Fujita, Y. Zong, N. Takemoto, S. Murai, and K. Tanaka. *Impact of Amorphization on the Magnetic Properties of EuO-TiO_2 system*. Phys. Rev. B **82**, 224403 (2010).

[191] D. Stornaiuolo, B. Jouault, E. Di Gennaro, A. Sambri, M. D'Antuono, D. Massarotti, F. M. Granozio, R. Di Capua, G. M. De Luca, G. P. Pepe, F. Tafuri, and M. Salluzzo. *Interplay between Spin-Orbit Coupling and Ferromagnetism in Magnetotransport Properties of a Spin-Polarized Oxide Two-Dimensional Electron System*. Phys. Rev. B **98**, 075409 (2018).

[192] T. Katsufuji and Y. Tokura. *Transport and Magnetic Properties of a Ferromagnetic Metal: $Eu_{1-x}R_xTiO_3$*. Phys. Rev. B **60**, R15021–R15023 (1999).

[193] K. Ahadi, Z. Gui, Z. Porter, J. W. Lynn, Z. Xu, S. D. Wilson, A. Janotti, and S. Stemmer. *Carrier Density Control of Magnetism and Berry Phases in Doped $EuTiO_3$*. APL Materials **6**, 056105 (2018).

[194] K. Ahadi, L. Galletti, and S. Stemmer. *Evidence of a Topological Hall Effect in $Eu_{1-x}Sm_xTiO_3$*. Applied Physics Letters **111**, 172403 (2017).

[195] G. Koster, B. L. Kropman, G. J. H. M. Rijnders, D. H. A. Blank, and H. Rogalla. *Quasi-Ideal Strontium Titanate Crystal Surfaces through Formation of Strontium Hydroxide*. Applied Physics Letters **73**, 2920–2922 (1998).

[196] M. Kawasaki, K. Takahashi, T. Maeda, R. Tsuchiya, M. Shinohara, O. Ishiyama, T. Yonezawa, M. Yoshimoto, and H. Koinuma. *Atomic Control of the $SrTiO_3$ Crystal Surface*. Science **266**, 1540–1542 (1994).

[197] D. H. Lowndes, D. B. Geohegan, A. A. Puretzky, D. P. Norton, and C. M. Rouleau. *Synthesis of Novel Thin-Film Materials by Pulsed Laser Deposition*. Science **273**, 898–903 (1996).

[198] P. R. Willmott and J. R. Huber. *Pulsed Laser Vaporization and Deposition*. Rev. Mod. Phys. **72**, 315–328 (2000).

[199] D. A. Glocker and S. Shah, eds. *Handbook of Thin Film Process Technology*. Vol. 1 (IOP Publishing, 2002).

[200] L. J. van der Pauw. *A Method of Measuring Specific Resistivity and Hall Effect of Discs of Arbitrary Shapes*. Philips Res. Repts. **13**, 1–9 (1958).

[201] L. J. van der Pauw. *A Method of Measuring the Resistivity and Hall Coefficient on Lamellae of Arbitrary Shape*. Philips Res. Repts. **20**, 220–224 (1958).

[202] Y. Wang, R. Ramaswamy, M. Motapothula, K. Narayanapillai, D. Zhu, J. Yu, T. Venkatesan, and H. Yang. *Room-Temperature Giant Charge-to-Spin Conversion at the $SrTiO_3-LaAlO_3$ Oxide Interface*. Nano Letters **17**, 7659–7664 (2017).

[203] D. Maryenko, A. S. Mishchenko, M. S. Bahramy, A. Ernst, J. Falson, Y. Kozuka, A. Tsukazaki, N. Nagaosa, and M. Kawasaki. *Observation of Anomalous Hall Effect in a Non-Magnetic Two-Dimensional Electron System*. Nature Communications **8**, 14777 (2017).

[204] P. Moetakef, T. A. Cain, D. G. Ouellette, J. Y. Zhang, D. O. Klenov, A. Janotti, C. G. Van de Walle, S. Rajan, S. J. Allen, and S. Stemmer. *Electrostatic Carrier Doping of $GdTiO_3$/$SrTiO_3$ Interfaces*. Applied Physics Letters **99**, 232116 (2011).

[205] M. N. Grisolia, J. Varignon, G. Sanchez-Santolino, A. Arora, S. Valencia, M. Varela, R. Abrudan, E. Weschke, E. Schierle, J. E. Rault, J.-P. Rueff, A. Barthélémy, J. Santamaria, and M. Bibes. *Hybridization-Controlled Charge Transfer and Induced Magnetism at Correlated Oxide Interfaces*. Nature Physics **12**, 484 (2016).

[206] T. Fix, F. Schoofs, J. L. MacManus-Driscoll, and M. G. Blamire. *Influence of Doping at the Nanoscale at $LaAlO_3$/$SrTiO_3$ Interfaces*. Applied Physics Letters **97**, 072110 (2010).

[207] S. Das, A. Rastogi, L. Wu, J.-C. Zheng, Z. Hossain, Y. Zhu, and R. C. Budhani. *Kondo Scattering in δ-doped $LaTiO_3$/$SrTiO_3$ Interfaces: Renormalization by Spin-Orbit Interactions*. Phys. Rev. B **90**, 081107 (2014).

[208] Y. C. Liao, T. Kopp, C. Richter, A. Rosch, and J. Mannhart. *Metal-Insulator Transition of the $LaAlO_3$-$SrTiO_3$ Interface Electron System*. Phys. Rev. B **83**, 075402 (2011).

[209] P. Reith, X. Renshaw Wang, and H. Hilgenkamp. *Analysing Magnetism Using Scanning SQUID Microscopy*. Review of Scientific Instruments **88**, 123706 (2017).

[210] B. Kalisky, J. A. Bert, B. B. Klopfer, C. Bell, H. K. Sato, M. Hosoda, Y. Hikita, H. Y. Hwang, and K. A. Moler. *Critical Thickness for Ferromagnetism in $LaAlO_3$/$SrTiO_3$ Heterostructures*. Nature Communications **3**, 922 (2012).

[211] B. Kalisky, J. A. Bert, C. Bell, Y. Xie, H. K. Sato, M. Hosoda, Y. Hikita, H. Y. Hwang, and K. A. Moler. *Scanning Probe Manipulation of Magnetism at the $LaAlO_3$/$SrTiO_3$ Heterointerface*. Nano Letters **12**, 4055–4059 (2012).

[212] J. Cumings, L. S. Moore, H. T. Chou, K. C. Ku, G. Xiang, S. A. Crooker, N. Samarth, and D. Goldhaber-Gordon. *Tunable Anomalous Hall Effect in a Nonferromagnetic System*. Phys. Rev. Lett. **96**, 196404 (2006).

[213] D. Culcer, A. Sekine, and A. H. MacDonald. *Interband Coherence Response to Electric Fields in Crystals: Berry-Phase Contributions and Disorder Effects*. Phys. Rev. B **96**, 035106 (2017).

[214] A. Fert and A. Friederich. *Skew Scattering by Rare-Earth Impurities in Silver, Gold, and Aluminum*. Phys. Rev. B **13**, 397–411 (1976).

[215] J. N. Chazalviel and I. Solomon. *Experimental Evidence of the Anomalous Hall Effect in a Nonmagnetic Semiconductor*. Phys. Rev. Lett. **29**, 1676–1679 (1972).

[216] S. R. Shinde, S. B. Ogale, J. S. Higgins, H. Zheng, A. J. Millis, V. N. Kulkarni, R. Ramesh, R. L. Greene, and T. Venkatesan. *Co-occurrence of Superparamagnetism and Anomalous Hall Effect in Highly Reduced Cobalt-Doped Rutile $TiO_{2-\delta}$ Films*. Phys. Rev. Lett. **92**, 166601 (2004).

[217] A. Yang, K. Zhang, S. Yan, S. Kang, Y. Qin, J. Pei, L. He, H. Li, Y. Dai, S. Xiao, and Y. Tian. *Superparamagnetism, Magnetoresistance and Anomalous Hall Effect in Amorphous Mn_xSi_{1-x} Semiconductor Films*. Journal of Alloys and Compounds **623**, 438 –441 (2015).

[218] S. X. Zhang, W. Yu, S. B. Ogale, S. R. Shinde, D. C. Kundaliya, W.-K. Tse, S. Y. Young, J. S. Higgins, L. G. Salamanca-Riba, M. Herrera, L. F. Fu, N. D. Browning, R. L. Greene, and T. Venkatesan. *Magnetism and Anomalous Hall Effect in Co–(La,Sr)TiO_3*. Phys. Rev. B **76**, 085323 (2007).

[219] S. Nakatsuji, N. Kiyohara, and T. Higo. *Large anomalous Hall effect in a non-collinear antiferromagnet at room temperature*. Nature **527**, 212 (2015).

[220] H. Chen, Q. Niu, and A. H. MacDonald. *Anomalous Hall Effect Arising from Noncollinear Antiferromagnetism*. Phys. Rev. Lett. **112**, 017205 (2014).

[221] P. Seiler, J. Zabaleta, R. Wanke, J. Mannhart, T. Kopp, and D. Braak. *Antilocalization at an Oxide Interface*. Phys. Rev. B **97**, 075136 (2018).

[222] N. Bovenzi and M. Diez. *Semiclassical Theory of Anisotropic Transport at $LaAlO_3/SrTiO_3$ Interfaces under an In-Plane Magnetic Field*. Phys. Rev. B **95**, 205430 (2017).

[223] M. Basletic, J.-L. Maurice, C. Carrétéro, G. Herranz, O. Copie, M. Bibes, É. Jacquet, K. Bouzehouane, S. Fusil, and A. Barthélémy. *Mapping the Spatial Distribution of Charge Carriers in $LaAlO_3/SrTiO_3$ Heterostructures*. Nature Materials **7**, 621 (2008).

[224] B. I. Edmondson, S. Liu, S. Lu, H. Wu, A. Posadas, D. J. Smith, X. P. A. Gao, A. A. Demkov, and J. G. Ekerdt. *Effect of $SrTiO_3$ Oxygen Vacancies on the Conductivity of $LaTiO_3$/$SrTiO_3$ Heterostructures*. Journal of Applied Physics **124**, 185303 (2018).

[225] S. W. Lee, Y. Liu, J. Heo, and R. G. Gordon. *Creation and Control of Two-Dimensional Electron Gas Using Al-Based Amorphous Oxides/$SrTiO_3$ Heterostructures Grown by Atomic Layer Deposition*. Nano Letters **12**, 4775–4783 (2012).

[226] D. Fuchs, R. Schäfer, A. Sleem, R. Schneider, R. Thelen, and H. von Löhneysen. *Two-Dimensional Superconductivity between $SrTiO_3$ and Amorphous Al_2O_3*. Applied Physics Letters **105**, 092602 (2014).

[227] P. Kumar, A. Dogra, and V. Toutam. *Pinhole Mediated Electrical Transport across $LaTiO_3$/$SrTiO_3$ and $LaAlO_3$/$SrTiO_3$ Oxide Hetero-structures*. Applied Physics Letters **103**, 211601 (2013).

[228] E. Flekser, M. Ben Shalom, M. Kim, C. Bell, Y. Hikita, H. Y. Hwang, and Y. Dagan. *Magnetotransport Effects in Polar Versus Non-polar $SrTiO_3$ Based Heterostructures*. Phys. Rev. B **86**, 121104 (2012).

[229] N. J. Goble, R. Akrobetu, H. Zaid, S. Sucharitakul, M.-H. Berger, A. Sehirlioglu, and X. P. A. Gao. *Anisotropic Electrical Resistance in Mesoscopic $LaAlO_3$/$SrTiO_3$ Devices with Individual Domain Walls*. Scientific Reports **7**, 44361 (2017).

[230] R. Vaglio, C. Attanasio, L. Maritato, and A. Ruosi. *Explanation of the Resistance-Peak Anomaly in Nonhomogeneous Superconductors*. Phys. Rev. B **47**, 15302–15303 (1993).

[231] X. Wang, W. M. Lü, A. Annadi, Z. Q. Liu, K. Gopinadhan, S. Dhar, T. Venkatesan, and Ariando. *Magnetoresistance of Two-dimensional and Three-dimensional Electron Gas in $LaAlO_3$/$SrTiO_3$ Heterostructures: Influence of Magnetic Ordering, Interface Scattering, and Dimensionality*. Phys. Rev. B **84**, 075312 (2011).

[232] M. M. Parish and P. B. Littlewood. *Non-saturating Magnetoresistance in Heavily Disordered Semiconductors*. Nature **426**, 162–165 (2003).

[233] T. Khouri, U. Zeitler, C. Reichl, W. Wegscheider, N. E. Hussey, S. Wiedmann, and J. C. Maan. *Linear Magnetoresistance in a Quasifree Two-Dimensional Electron Gas in an Ultrahigh Mobility GaAs Quantum Well*. Phys. Rev. Lett. **117**, 256601 (2016).

[234] J. Hu, M. M. Parish, and T. F. Rosenbaum. *Nonsaturating Magnetoresistance of Inhomogeneous Conductors: Comparison of Experiment and Simulation*. Phys. Rev. B **75**, 214203 (2007).

[235] F. Kisslinger, C. Ott, and H. B. Weber. *Origin of Nonsaturating Linear Magnetoresistivity*. Phys. Rev. B **95**, 024204 (2017).

[236] N. Ramakrishnan, Y. T. Lai, S. Lara, M. M. Parish, and S. Adam. *Equivalence of Effective Medium and Random Resistor Network Models for Disorder-Induced Unsaturating Linear Magnetoresistance*. Phys. Rev. B **96**, 224203 (2017).

[237] T. Schumann, M. Goyal, D. A. Kealhofer, and S. Stemmer. *Negative Magnetoresistance due to Conductivity Fluctuations in Films of the Topological Semimetal Cd_3As_2*. Phys. Rev. B **95**, 241113 (2017).

[238] J. Xu, M. K. Ma, M. Sultanov, Z.-L. Xiao, Y.-L. Wang, D. Jin, Y.-Y. Lyu, W. Zhang, L. N. Pfeiffer, K. W. West, K. W. Baldwin, M. Shayegan, and W.-K. Kwok. *Negative Longitudinal Magnetoresistance in Gallium Arsenide Quantum Wells*. Nature Communications **10**, 287 (2019).

[239] G. N. Daptary, S. Kumar, P. Kumar, A. Dogra, N. Mohanta, A. Taraphder, and A. Bid. *Correlated non-Gaussian Phase Fluctuations in $LaAlO_3$/$SrTiO_3$ Heterointerfaces*. Phys. Rev. B **94**, 085104 (2016).

[240] H. Thierschmann, E. Mulazimoglu, N. Manca, S. Goswami, T. M. Klapwijk, and A. D. Caviglia. *Transport Regimes of a Split Gate Superconducting Quantum Point Contact in the Two-Dimensional $LaAlO_3$/$SrTiO_3$ Superfluid*. Nature Communications **9**, 2276 (2018).

[241] S. Hurand, A. Jouan, E. Lesne, G. Singh, C. Feuillet-Palma, M. Bibes, A. Barthélémy, J. Lesueur, and N. Bergeal. *Josephson-like Dynamics of the Superconducting $LaAlO_3$/$SrTiO_3$ Interface*. Phys. Rev. B **99**, 104515 (2019).

[242] Y. Frenkel, N. Haham, Y. Shperber, C. Bell, Y. Xie, Z. Chen, Y. Hikita, H. Y. Hwang, E. K. H. Salje, and B. Kalisky. *Imaging and Tuning Polarity at $SrTiO_3$ Domain Walls*. Nature Materials **16**, 1203 (2017).

[243] Y.-Y. Pai, H. Lee, J.-W. Lee, A. Annadi, G. Cheng, S. Lu, M. Tomczyk, M. Huang, C.-B. Eom, P. Irvin, and J. Levy. *One-Dimensional Nature of Superconductivity at the $LaAlO_3$/$SrTiO_3$ Interface*. Phys. Rev. Lett. **120**, 147001 (2018).

[244] R. V. Vovk, G. Y. Khadzhai, I. L. Goulatis, S. N. Kamchatnaya, and A. Chroneos. *Diffusion of the Superconducting Transition in HTSC*. Journal of Materials Science: Materials in Electronics **28**, 10862–10865 (2017).

[245] H. S. Gamchi, G. J. Russell, and K. N. R. Taylor. *Resistive Transition for $YBa_2Cu_3O_{7-\delta}$-Y_2BaCuO_5 Composites: Influence of a Magnetic Field*. Phys. Rev. B **50**, 12950–12958 (1994).

[246] I. Felner, E. Galstyan, B. Lorenz, D. Cao, Y. S. Wang, Y. Y. Xue, and C. W. Chu. *Magnetoresistance Hysteresis and Critical Current Density in Granular $RuSr_2Gd_{2-x}Ce_xCu_2O_{10-\delta}$*. Phys. Rev. B **67**, 134506 (2003).

[247] M. Sandim and R. Jardim. *Intergranular Transport Properties of Polycrystalline $Sm_{1.82}Ce_{0.18}CuO_{4-y}$ under Low Applied Magnetic Fields*. Physica C: Superconductivity **328**, 246 –256 (1999).

[248] S. A. Wolf, D. U. Gubser, W. W. Fuller, J. C. Garland, and R. S. Newrock. *Two-Dimensional Phase Transition in Granular NbN Films*. Phys. Rev. Lett. **47**, 1071–1074 (1981).

[249] D. J. Resnick, J. C. Garland, J. T. Boyd, S. Shoemaker, and R. S. Newrock. *Kosterlitz-Thouless Transition in Proximity-Coupled Superconducting Arrays*. Phys. Rev. Lett. **47**, 1542–1545 (1981).

[250] D. W. Abraham, C. J. Lobb, M. Tinkham, and T. M. Klapwijk. *Resistive Transition in Two-Dimensional Arrays of Superconducting Weak Links*. Phys. Rev. B **26**, 5268–5271 (1982).

[251] Y. J. Qian, Z. M. Tang, K. Y. Chen, B. Zhou, J. W. Qiu, B. C. Miao, and Y. M. Cai. *Transport Hysteresis of the Oxide Superconductor $Y_1Ba_2Cu_3O_{7-x}$ in Applied Fields*. Phys. Rev. B **39**, 4701–4703 (1989).

[252] Y. V. Kopelevich, V. V. Lemanov, and V. V. Makarov. *Influence of Weak Bonds on Electrical Properties of $YBa_2Cu_3O_{69}$ Ceramics*. **32**, 3613–3617 (1990).

[253] K. Kwasnitza and C. Widmer. *Hysteretic Effects in the Flux-Flow State of Granular High-Tc Superconductors*. Physica C: Superconductivity **171**, 211 –215 (1990).

[254] C. dos Santos, M. da Luz, B. Ferreira, and A. Machado. *On the Transport Properties in Granular or Weakly Coupled Superconductors*. Physica C: Superconductivity **391**, 345 –349 (2003).

[255] P Muné, F. Fonseca, R Muccillo, and R. Jardim. *Magnetic Hysteresis of the Magnetoresistance and the Critical Current Density in Polycrystalline $YBa_2Cu_3O_{7-\delta}$–Ag Superconductors*. Physica C: Superconductivity **390**, 363 –373 (2003).

[256] D. A. Balaev, D. M. Gokhfeld, A. A. Dubrovskiĭ, S. I. Popkov, K. A. Shaikhutdinov, and M. I. Petrov. *Magnetoresistance Hysteresis in Granular HTSCs as a Manifestation of the Magnetic Flux Trapped by Superconducting Grains in YBCO + CuO Composites*. Journal of Experimental and Theoretical Physics **105**, 1174–1183 (2007).

[257] J. Evetts and B. Glowacki. *Relation of Critical Current Irreversibility to Trapped Flux and Microstructure in Polycrystalline $YBa_2Cu_3O_7$*. Cryogenics **28**, 641 –649 (1988).

[258] G. N. Daptary, S. Kumar, A. Bid, P. Kumar, A. Dogra, R. C. Budhani, D. Kumar, N. Mohanta, and A. Taraphder. *Observation of Transient Superconductivity at the $LaAlO_3/SrTiO_3$ Interface*. Phys. Rev. B **95**, 174502 (2017).

[259] M. E. McHenry, M. P. Maley, and J. O. Willis. *Systematics of Transport Critical-Current-Density Hysteresis in Polycrystalline Y-Ba-Cu-O*. Phys. Rev. B **40**, 2666–2669 (1989).

[260] L. Ji, M. S. Rzchowski, N. Anand, and M. Tinkham. *Magnetic-Field-Dependent Surface Resistance and Two-Level Critical-State Model for Granular Superconductors*. Phys. Rev. B **47**, 470–483 (1993).

[261] K. A. Delin, T. P. Orlando, E. J. McNiff, S. Foner, R. B. van Dover, L. F. Schneemeyer, and J. V. Waszczak. *High-Field Magnetization Scaling Relations for Pure and Ni-Substituted Single-Crystal $YBa_2Cu_3O_7$*. Phys. Rev. B **46**, 11092–11101 (1992).

[262] Půst, L. and Kadlecová, J. and Jirsa, M. and Durčok, S. *Correlation between Magnetic Hysteresis and Magnetic Relaxation in YBaCuO Single Crystals*. Journal of Low Temperature Physics **78**, 179–186 (1990).

[263] M Požek, I Ukrainczyk, B Rakvin, and A Dulčić. *Dynamic Measurements of Flux Creep and Flow in $YBa_2Cu_3O_{7-\delta}$ Single Crystals*. Europhysics Letters (EPL) **16**, 683–688 (1991).

[264] M. Jirsa, L. Pust, H. Schnack, and R. Griessen. *Extension of the Time Window for Investigation of Relaxation Effects in High-Tc Superconductors*. Physica C: Superconductivity **207**, 85 –96 (1993).

[265] G. Venditti, J. Biscaras, S. Hurand, N. Bergeal, J. Lesueur, A. Dogra, R. C. Budhani, M. Mondal, J. Jesudasan, P. Raychaudhuri, S. Caprara, and L. Benfatto. *Nonlinear $I-V$ Characteristics of Two-Dimensional Superconductors: Berezinskii-Kosterlitz-Thouless Physics versus Inhomogeneity*. Phys. Rev. B **100**, 064506 (2019).

[266] Y. Liu, D. B. Haviland, B. Nease, and A. M. Goldman. *Insulator-to-Superconductor Transition in Ultrathin Films*. Phys. Rev. B **47**, 5931–5946 (1993).

[267] B. Shklovskii and A. Efros. *Electronic Properties of Doped Semiconductors*. Springer Series in Solid-State Sciences (Springer Berlin Heidelberg, 1984).

[268] D. Mandrus, L. Forro, C. Kendziora, and L. Mihaly. *Two-dimensional Electron Localization in Bulk Single Crystals of $Bi_2Sr_2Y_xCa_{1-x}Cu_2O_8$*. Phys. Rev. B **44**, 2418–2421 (1991).

[269] D. B. Haviland, H. M. Jaeger, B. G. Orr, and A. M. Goldman. *Local Superconducting Coupling in the Strong-Localization Limit of Ultrathin Granular Metal Films*. Phys. Rev. B **40**, 719–722 (1989).

[270] C. G. L. Bøttcher, F. Nichele, M. Kjaergaard, H. J. Suominen, J. Shabani, C. J. Palmstrøm, and C. M. Marcus. *Superconducting, Insulating and Anomalous Metallic Regimes in a Gated Two-Dimensional Semiconductor-Superconductor Array*. Nature Physics **14**, 1138–1144 (2018).

[271] Z. Ye, I. F. Lyuksyutov, W. Wu, and D. G. Naugle. *Strongly Anisotropic Flux Pinning in Superconducting $Pb_{82}Bi_{18}$ Thin Films Covered by Periodic Ferromagnet Stripes*. Superconductor Science and Technology **24**, 024011 (2011).

[272] K. Tanaka, K. Fujita, Y. Maruyama, Y. Kususe, H. Murakami, H. Akamatsu, Y. Zong, and S. Murai. *Ferromagnetism Induced by Lattice Volume Expansion and Amorphization in $EuTiO_3$ Thin Films*. Journal of Materials Research **28**, 1031–1041 (2013).

[273] S. C. Chae, Y. J. Chang, D.-W. Kim, B. W. Lee, I. Choi, and C. U. Jung. *Magnetic Properties of Insulating $RTiO_3$ Thin Films*. Journal of Electroceramics **22**, 216–220 (2009).

[274] K. Hatabayashi, T. Hitosugi, Y. Hirose, X. Cheng, T. Shimada, and T. Hasegawa. *Fabrication of $EuTiO_3$ Epitaxial Thin Films by Pulsed Laser Deposition*. Japanese Journal of Applied Physics **48**, 100208 (2009).

[275] K. Jiang, R. Zhao, P. Zhang, Q. Deng, J. Zhang, W. Li, Z. Hu, H. Yang, and J. Chu. *Strain and Temperature Dependent Absorption Spectra Studies for Identifying the Phase Structure and Band Gap of $EuTiO_3$ Perovskite Films*. Phys. Chem. Chem. Phys. **17**, 31618–31623 (2015).

[276] F Trier, D. V. Christensen, and N Pryds. *Electron Mobility in Oxide Heterostructures*. Journal of Physics D: Applied Physics **51**, 293002 (2018).

[277] E. Mikheev, B. Himmetoglu, A. P. Kajdos, P. Moetakef, T. A. Cain, C. G. Van de Walle, and S. Stemmer. *Limitations to the room Temperature Mobility of Two- and Three-Dimensional Electron Liquids in $SrTiO_3$*. Applied Physics Letters **106**, 062102 (2015).

[278] A. Fête, S. Gariglio, A. D. Caviglia, J.-M. Triscone, and M. Gabay. *Rashba Induced Magnetoconductance Oscillations in the $LaAlO_3$-$SrTiO_3$ Heterostructure*. Phys. Rev. B **86**, 201105 (2012).

[279] K. Bethe. *Über Das Mikrowellenverhalten Nichtlinearer Dielektrika*. Philips Res. Repts Suppl. **№ 2** (1970).

[280] O. G. Vendik, E. K. Hollmann, A. B. Kozyrev, and A. M. Prudan. *Ferroelectric Tuning of Planar and Bulk Microwave Devices*. Journal of Superconductivity **12**, 325–338 (1999).

[281] R. C. Neville, B. Hoeneisen, and C. A. Mead. *Permittivity of Strontium Titanate*. Journal of Applied Physics **43**, 2124–2131 (1972).

Summary

Under particular circumstances, interfaces between two insulating oxide materials can become metallic. The ensuing two-dimensional electron system forms an intriguing object for research. This work focuses on the magnetotransport properties of conducting interfaces formed by a single crystalline, insulating and non-magnetic substrate, $SrTiO_3$ (STO), on which another insulating oxide with a similar crystal structure is deposited in the form of a thin film. This second material will in general contain magnetic ions. A special property of STO is that its large dielectric constant allows the substrate to be used as a back gate, allowing an electric field to vary and control the amount of charge carriers at the interface. The thin-film building blocks which were studied are similar to STO, also perovskites, namely the canonical material $LaAlO_3$(LAO) (insulating and non-magnetic) and the rare earth titanates $GdTiO_3$(GTO), $Eu_{1-x}La_xTiO_3$ (x=0 and 0.1), and $LaTiO_3$(LTO), all of which are magnetic. The main question I wanted to answer was whether the conduction electrons at the interface can become magnetic, that is spin-polarized, due to the use of the magnetic ions in the thin films. Moreover, several of the studied interfaces show superconductivity at low temperatures, which could also be investigated.

The thin film deposition was performed by Pulsed Laser Deposition (PLD). Not all materials are easy to grow in a reproducible manner in this way, but despite that, a wide range of phenomena such as the Anomalous Hall effect (AHE) (which is connected to the occurrence of magnetism), anomalous behavior of the magnetoresistance, non-uniform superconductivity, magnetic hysteresis, and signatures of the Kondo effect (yielding a minimum in the resistance when the temperature is decreased from room temperature) could be successfully studied. In the following, new insights deriving from this thesis are enumerated. Generically, all observations report that the conductance of the interface can be either due to one type (band) of carriers, or to two types or bands. The gate voltage tunes the Fermi energy and can bring the system from a one-band to a two-band regime, by injecting charge carriers and populating or depopulating the second band. The voltage at which the second band it switched on is called the Lifshitz point.

The Anomalous Hall Effect in magnetically doped oxide interfaces

Various perovskite oxide interfaces display the Anomalous Hall Effect. Its importance is that it is usually understood as a signature of the presence of ferromagnetism (long range magnetic order). Different mechanisms have been proposed to generate AHE, and there is a tendency to ascribe its observation to a one-ingredient mechanism despite the fact that, by its nature, it is the result of a complex interplay of different effects. To study the AHE, we chose delta-doped LAO/X/STO, with X being a few-atomic-layer thin magnetic oxide, either GTO or $Eu_{1-x}La_xTiO_3$(x=0, 0.1). It was experimentally difficult to grow GTO layers. LAO/GTO/STO was found to be severely intermixed and become $La_{1-x}Gd_xAlO_3/Gd_{1-y}La_yTi_{1-z}Al_zO_3$/STO (LGAO/GLTAO/STO), although still preserving crystallinity. As demonstrated in chapter 3, these samples exhibit an AHE which is tunable by the gate voltage and occurs at low temperatures in the two-band regime, close to the Lifshitz point. Two methods were utilized for the analysis, one which was proposed earlier in the literature, and one which was adapted from more conventional AHE analysis. They yielded similar results and indicated that the vicinity of the Lifshitz point and the ensuing strong spin-orbit coupling are important for observing the AHE. An important and unexpected result is that we did not find indications of ferromagnetism, which was probed directly via scanning SQUID microscopy. This implies that the system is rather superparamagnetic or paramagnetic rather than ferromagnetic. A follow-up study of AHE in LAO/$EuTiO_3$/STO (LAO/ETO/STO), LAO/$Eu_{0.9}La_{0.1}TiO_3$/STO (LAO/ELTO/STO), and LAO/STO heterostructures is presented in chapter 6. There, we did not observe AHE in the non-delta-doped sample, whereas the strength of AHE increases with increasing concentration of Eu. Although some authors argue that external magnetic doping need not be part of the mechanism of the AHE, here we see that magnetic doping is important for the AHE in LAO/ETO/STO structures. Intriguingly, a scaling analysis did not show the behavior expected for so-called skew-scattering, which is taken as the the main mechanism for AHE in most structures.

A percolative superconducting transition at the interface between an amorphous LTO film and a STO substrate

The interfaces that are discussed in this thesis are formed by perovkite titanates, deposited on STO. $LaTiO_3$is the compound which does not contain a magnetic Rare Earth ion, and therefore serves a reference system. The samples we grew show the LTO layer to be amorphous, not crystalline, which makes for an interesting interface system in itself, despite the somewhat uncontrolled nature of the amorphization process. This system exhibits the usual and typical properties of these oxide interfaces, namely two-band behavior and a Lifshitz point. In that

sense, the amorphous system does not appear to be different from a crystalline one. However, a large linear magnetoresistance (MR) and a percolative superconducting transition indicate large inhomogeneities formed at the interface. To describe the superconducting transition, we used a resistor model, which describes the observations quite well. The (unevenly distributed) oxygen stoichiometry is argued to be a reason for the formation of large-scale inhomogeneities.

The coexistence of superconductivity and magnetism at oxide interfaces

The coexistence of superconductivity and magnetism at the conducting oxide interface is still a hotly debated topic. Initial reports on the signatures of magnetism in the superconducting state were met with excitement. Early studies on the magnetoresistance of such superconducting interfaces described hysteresis observed below the superconducting transition temperatures and discussed the possible role of magnetism. The non-trivial behavior, which could not be easily ascribed to ferromagnetic magnetization dynamics alone, was explained through a complicated picture of a superconductor in proximity to a complex magnetic texture. Other studies argued that the dependence of the MR effects on the sweep rate of the magnetic field indicate magnetocaloric effects rather than magnetic effects in the sample. Although such effects can indeed play a role, we find that magnetic hysteresis in the oxide interfaces can also be the sign of an inhomogeneous superconducting state. In chapter 5, two oxide systems with different types of disorder were studied. One system is the interface between amorphous LTO and crystalline STO, known from chapter 4; the other is the crystalline but strongly intermixed LGAO/GLTAO/STO system from chapter 3. The first one has disorder due to a nonuniform oxygen content, whereas the second has magnetic atoms that suppress superconductivity and create weak links between superconducting regions in the system. The amorphous system shows signatures of large-scale inhomogeneities, whereas a two-level model can describe LGAO/GLTAO/STO. Despite some differences, both systems exhibit magnetic hysteresis at low temperatures, which can be understood through the models for non-uniform superconductors without including ferromagnetism.

A Kondo-effect in the conductivity of oxide interfaces

In conducting oxide interfaces, a minimum in the temperature dependence of the sheet resistance, is often observed. For a long time it was considered as strong evidence of a Kondo effect, in which magnetic moments present at the interfaces were shielded by conduction electrons. Switching between a regime showing the AHE (and so ferromagnetism) and this regime was usually considered to be further

evidence of the Kondo picture. Early pressure experiments proposed an alternative explanation which was overlooked in subsequent research. However, detailed experimental and theoretical studies of the temperature and gate dependence of the magnetoresistance showed the Kondo-picture to disagree with experiments. The current work also addresses this question and concentrates on the temperature dependence of the sheet resistance. As shown in chapter 6, a gate-tunable minimum in the temperature dependence of the sheet resistance was observed in all systems studied here. Through a detailed study of magnetotransport properties we show that the minimum turns out to be relatively insensitive to magnetic doping, which is not expected for the magnetic Kondo picture, whereas we do observe the apparent effects on the AHE that were mentioned earlier. As it turns out, other mechanisms such as the temperature and electric field dependence of the STO permittivity, charge trapping at the interface, the behavior of the carrier concentrations and mobilities of both conduction bands, and spinless scattering mechanisms are sufficient to describe the observed minimum. Even if the Kondo effect cannot be ruled out entirely, it most likely is masked by the effects mentioned above. This observation may shine new light on the sometimes confusing behavior of the magnetoelectric transport properties of oxide interfaces.

Samenvatting

Onder bepaalde omstandigheden kan het grensvlak tussen twee isolerende oxides zelf metallisch worden. Het electronensysteem is dan tweedimensionaal, en vormt een intrigerende onderzoeksobject. De studie in dit proefschrift richt zich op de magnetotransport eigenschappen van grensvlakken gevormd tussen een één-kristallijn, isolerend, en niet-magnetisch substraat, $SrTiO_3$ (STO), en een ander isolerend oxide, met een soortgelijke kristalstructuur, dat in de vorm van een dunne film op het substraat gedeponeerd wordt. Dat tweede materiaal bevat bijna steeds magnetische ionen. Een bijzondere eigenschap van STO is dat de grote diëlectrische constante het materiaal zeer geschikt maakt om als 'backgate' te dienen, waardoor met een electrische spanning het aantal ladingsdragers aan het grensvlak gecontroleerd veranderd kan worden.
De dunne films die als bouwblok voor het grensvlak dienen waren perovskiet materialen, gelijkend op STO, namelijk het kanonieke materiaal $LaAlO_3$ (LAO) (isolerend en niet magnetisch), en de zeldzame-aard titanaten $GdTiO_3$ (GTO), $Eu_{1-x}La_xTiO_3$ (x = 0 en 0.1), en $LaTiO_3$, die allemaal magnetisch zijn. De belangrijkste vraag die dit proefschrift wilde beantwoorden is of de geleidingselectronen aan het grensvlak magnetisch kunnen worden, dat wil zeggen spin-gepolariseerd, door het gebruik van magnetische ionen in de dunne films. Bovendien treedt in verschillende van de bestudeerde grensvlakken bij lage temperaturen supergeleiding op, en ook dat fenomeen kon bestudeerd worden.

De depositie van de dunne films werd gedaan met 'pulsed laser depositie' (PLD). Niet alle materialen zijn hiermee gemakkelijk reproduceerbaar te groeien, maar desondanks, kon een reeks van verschijnselen succesvol bestudeerd worden. Daaronder waren het anomale Hall effect (AHE), dat iets zegt over de aanwezigheid van magnetisme, anomaal gedrag van de magnetoweerstand, niet-uniforme supergeleiding, magnetische hysterese, en aanwijzingen voor het Kondo effect, gekenmerkt door een weerstandsminimum bij lage temperaturen). Hieronder worden de nieuw verkregen inzichten op een rijtje gezet, Het generieke referentiekader voor alle waarnemingen is dat de grensvlakgeleiding door één dan wel door twee electronenbanden tot stand komt. De gate-spanning bepaalt de positie van de Fermi energie in de banden, en kan in het bijzonder het systeem van

het één-band naar het twee-banden regime brengen, door extra ladingsdragers naar het grensvlak te trekken. De spanning waarbij de tweede band aangeschakeld wordt heet het Lifshitz-punt.

Het Anomale Hall Effect in magnetisch gedoopte oxide grensvlakken

Het optreden van het AHE is in verschillende perovskiet-oxide gebaseerde grensvlakken waargenomen. Het belang van het effect is dat het over het algemeen gezien wordt als de handtekening van de aanwezigheid van ferromagnetisme (lange-afstand magnetische ordening). Er zijn verschillende mechanismes voorgesteld die tot een AHE kunnen leiden, en de neiging bestaat om een bepaalde waarneming aan één mechanisme in het bijzonder te verbinden, ondanks het feit dat het effect onder alle omstandigheden een complex samenspel van factoren is.
Om het AHE te bestuderen kozen we voor een 'delta-doping' systeem van de vorm LAO/X/STO waarbij X een magnetisch oxide is van maar een paar atoomlagen dik, hetzij GTO of $Eu_{1-x}La_xTiO_3$ met x = 0 of 0.1. Het bleek moeilijk te zijn de GTO lagen te groeien. We vonden sterke vermenging in LAO/GTO/STO, waardoor het eerder $La_{1-x}Gd_xAlO_3/Gd_{1-y}La_yTi_{1-z}Al_zO_3$/STO werd (LGAO/GLTAO/STO), hoewel de laag nog steed kristallijn was. Zoals besproken in hoofdstuk 3, vertonen deze preparaten een AHE, afhankelijk van de aangelegde gate spanning, en wel alleen in het twee-banden regime net voorbij het Lifshitz punt, en bij lage temperaturen. Er werden twee methodes gebruikt voor de data analyse. De eerste was al in eerdere studies van oxide grensvlakken gebruikt, de tweede was een aanpassing aan AHE analyse in standaardsituaties. Ze geven vergelijkbare resultaten, en laten zien dat de nabijheid van het Lifshitz punt belangrijk is, waarschijnlijk doordat de spin baan koppeling daar sterk is. Een belangrijk en onverwacht resultaat is dat we geen indicaties van ferromagnetisme vonden. Het impliceert dat het systeem eerder superparamagnetisch of para-magnetisch is.
Een vervolgstudie van het AHE in LAO/$EuTiO_3$/STO (LAO/ETO/STO), LAO/$Eu_{0.9}La_{0.1}TiO_3$/STO (LAO/ELTO/STO), en LAO/STO structuren wordt beschreven in hoofdstuk 6. We vonden geen AHE in samples waar delta-doping afwezig was, en een sterker AHE met toenemende Eu concentratie. Hoewel sommige studies argumenteren dat externe magnetische doping geen onderdeel van het mechanisme voor het AHE is, vinden wij die doping wel van belang in LAO/ETO/STO. Een intrigerende observatie is dat schalingsanalyse van de geleiding en de Hall geleiding niet wijst in de richting van zogenaamde skew-scattering, wat juist vaak aangenomen wordt het belangrijkste mechanisme te zijn in de meeste structuren.

Een percolatie-gedomineerde supergeleidende overgang op het grensvlak tussen een amorfe LTO film en een STO substraat

De belangrijkste grensvlakken in dit proefschrift zijn die van diverse perovskiet titanaten, gedeponeerd op STO. $LaTiO_3$ is de verbinding die geen magnetische xeldzame aard ionen bevat, en dient daarom als niet-magnetisch referentiesysteem. De LTO lagen die we groeiden bleken amorf te zijn, niet kristallijn, en dat levert ook interessante grensvlak systemen voor onderzoek, ondanks het ietwat ongecontroleerde amorfizatie proces. Het systeem vertoont de gebruikelijke en typerende eigenschappen van deze oxide grensvlakken, namelijk tweebanden gedrag en de aanwezigheid van een Lifshitz punt. Wat dat betreft lijkt het amorfe systeem niet verschillend te zijn van een kristallijn systeem. Het vertoont echter een sterk lineaire magnetoweerstand en een percolatie-gedomineerde supergeleidende overgang, die op een sterk inhomogeen grensvlak wijzen. Om dat te beschrijven wordt een weerstandsmodel gebruikt, waarmee de waarnemingen goed beschreven kunnen worden. Het vermoeden is dat variaties in de zuurstof stoichiometrie de reden zijn voor de gevonden inhomogeniteiten.

De co-existentie van supergeleiding en magnetisme op oxide grensvlakken

De mogelijke co-existentie van supergeleiding en magnetisme in geleidende oxide grensvlakken is nog steeds onderwerp van heftige discussie. De eerste waarnemingen van de aanwezigheid van magnetisme in de supergeleidende toestand wekten grote interesse. In de magnetoweerstand werd hysterese gezien bij temperaturen beneden die van de supergeleidende overgang, wat besproken werd in termen van magnetisme. Het niet-triviale gedrag, wat niet eenvoudigweg kon worden toegeschreven aan magnetizatie-dynamica van de ferromagneet, werd verklaard met een ingewikkeld model van een supergeleider in aanraking met complexe magnetische textuur. Latere studies beargumenteerden dat het feit dat de magnetoweerstand afhankelijk is van de snelheid waarmee het magneetveld verandert (de 'sweep rate'), eerder op magnetocalorische dan op magnetische effecten wijst. Hoewel zo'n effect zeker een rol kan spelen, vinden we in deze studie dat de magnetische hysterese ook een teken van een inhomogene supergeleidende toestand kan zijn. In hoofdstuk 5 worden twee grensvlak systemen met verschillende types wanorde bestudeerd. Het ene is het grensvlak tussen amorf LTO en kristallijn STO, bekend uit hoofdstuk 4. Het andere is het kristallijne maar sterk gemengde systeem LGAO/GLTAO/STO uit hoofdstuk 3. Het eerste systeem vertoont wanorde vanwege niet-uniforme zuurstofinhoud; in het tweede wordt wanorde veroorzaakt door magnetische atomen die supergeleiding onderdrukken en daarmee zwakke schakels creëeren tussen supergeleidende gebieden. Het amorfe systeem vertoont inhomogeniteiten over grote lengteschalen; LGAO/GLTAO/STO kan beschreven

worden als een twee-niveau systeem. Er zijn verschillen, maar beide systemen vertonen magnetoweerstands hysterese bij lage temperaturen, die begrepen kan worden met modellen voor inhomogene supergeleiders zonder gebruik te maken van ferromagnetisme.

Een mogelijk Kondo effect in oxide grensvlakken

Vaak wordt in de temperatuurafhankelijkheid van de vierkantsweerstand van oxide grensvlakken een minimum waargenomen. Gedurende lange tijd werd dit opgevat als een sterke aanwijzing voor een Kondo effect, waarbij magnetische momenten die aanwezig zijn aan of in het grensvlak, afgeschermd worden door geleidingselectronen. Het kunnen veranderen van een regime met het AHE (en dus ferromagnetisme) naar dit regime werd beschouwd als een verdere aanwijzing voor een Kondo effect. Studies van de drukafhankelijkheid van het weerstandsgedrag leverden een andere interpetatie, maar werden over het hoofd gezien in later werk. Toch tonen gedetailleerde experimentele en theoretische studies van de temperatuur- en gate-afhankelijkheid van de magnetoweestand dat het Kondo beeld niet overeen stemt met de experimenten

De hier gepresenteerde studie gaat ook op die vraag in, en concentreert zich op de temperatuurafhankelijke vierkantsweerstand van het grensvlak. In hoofdstuk 6 laten we zien dat de verschillende grensvlak systemen een minimum laten zien dat afhangt van de aangelegde gate spanning. Uit een gedetailleerd onderzoek van de magnetotransport eigenschappen blijkt dat het weerstandsminimum ongevoelig is voor magnetische doping, wat niet verwacht wordt in het Kondo beeld. Wel wordt het AHE waargenomen, zoals eerder beschreven. Het blijkt dat andere mechanismes zoals de afhankelijkheid van de permittiviteit van STO van temperatuur en electrisch veld, ladingsvangst aan het grensvlak, het gedrag van de ladingsdichtheden en mobiliteiten, en spin-onafhankelijke verstrooiïngsmechanismes voldoende zijn om de waargenomen minima te verklaren. Het optreden van het Kondo effect is niet uitgesloten, maar dan wordt het gemaskeerd door deze andere effecten. Deze beschrijving werpt mogelijk nieuw licht op het soms verwarrende gedrag van de magneto-electrische transporteigenschappen van oxide grensvlakken.

List of Publications

Publications

- **N. Lebedev**, M. Stehno, A. Rana, P. Reith, N. Gauquelin, J. Verbeeck, H. Hilgenkamp, A. Brinkman, and J. Aarts. Gate-tuned Anomalous Hall Effect Driven by Rashba Splitting in Intermixed $LaAlO_3/GdTiO_3/SrTiO_3$, arxiv.org/abs/2002.11408, and *submitted to Physical Review Materials*.

- **N. Lebedev**, M. Stehno, A. Rana, N. Gauquelin, J. Verbeeck, A. Brinkman, and J. Aarts. Inhomogeneous superconductivity and quasilinear magnetoresistance at amorphous $LaTiO_3/SrTiO_3$ interfaces, arxiv.org/abs/2008.03224, and *accepted for publication in Journal of Physics: Condensed Matter*.

- **N. Lebedev**, M. Stehno, A. Rana, N. Gauquelin, J.Verbeeck, A. Brinkman, and J. Aarts, On the superconducting-insulator transition in disordered oxide interfaces, *in preparation for publication*.

- C. Yin, A. E. M. Smink, I. Leermakers, L. M. K. Tang, **N. Lebedev**, U. Zeitler, W. G. van der Wiel, H. Hilgenkamp, and J. Aarts. Electron Trapping Mechanism in $LaAlO_3/SrTiO_3$ Heterostructures, Phys. Rev. Lett. **124**, 017702 (2020).

- C. Yin, P. Seiler, L. M. K. Tang, I. Leermakers, **N. Lebedev**, U. Zeitler, and J. Aarts. Tuning Rashba spin-orbit coupling at $LaAlO_3/SrTiO_3$ interfaces by band filling, Phys. Rev. B **101**, 245114 (2020).

- H. Arjmandi-Tash, **N. Lebedev**, P. M. G. van Deursen, J. Aarts, and G. F. Schneider, Hybrid cold and hot-wall reaction chamber for the rapid synthesis of uniform graphene, Carbon **118**, 438 (2017).

Curriculum Vitae

I was born on the 4th of October 1990 in Kamensk-Uralsky, Russia. Before my school years, my family moved to Revda, where I attended school. In 2008, I was admitted to the Institute of Physics and Technology, Ural Federal University in Yekaterinburg. After completing the third academic year, I started an internship at the Institute of Metal Physics, Ural Branch of the Russian Academy of Sciences. Soon after, I was hired as a part-time research technician. Other internship projects and research work, including my Diploma project on giant magnetic resistance in metal multilayers, were also performed at the Institute of Metal Physics. I graduated from Ural Federal University in 2014. After graduation, I continued to work as a research technician at the Institute of Metal physics for some time. At the end of 2014, I started my Ph.D. on the growth and transport properties of $LaAlO_3/SrTiO_3$ interfaces in the group of Prof. Dr. Jan Aarts in Leiden.

Acknowledgements

The research described in this thesis would not have been possible without the direct and indirect support of many people. I am afraid that I may unintentionally miss many names in this part and would like to ask you to forgive me for that. I would like to start by expressing my deepest appreciation for my promoter, Jan Aarts, for the opportunity to work on this project. I am grateful for your supervision and inspiration as well as the research freedom, which I was able to enjoy.

I was lucky to have the opportunity to collaborate with many people inside and outside Leiden University. I would like to express my gratitude to Martin Stehno for performing low-temperature experiments, assistance with the Pulsed Laser Deposition (PLD) setup, and sharing his knowledge with me. I am grateful to Abhimanyu Singh Rana for PLD sample preparation, first transport measurements, and sharing his knowledge about the oxide growth with me. I would like to thank Pim Reith for performing Scanning SQUID microscopy experiments. I am thankful to Nicolas Gauquelin for Scanning Transmission Electron Microscopy and Electron Energy Loss Spectroscopy measurements. Special thanks go to Yingkai Huang for preapration of $EuTiO_3$ and $Eu_{1-x}La_xTiO_3$ PLD target. Frank Roesthuis's help with PLD and other experiments at Twente University was crucial.
I owe a very important debt to Alexander Brinkman and Hans Hilgenkamp for the valuable feedback and trust they put in allowing me to use the PLD system at the University of Twente on my own. I am grateful to Marcel Hesselberth, Douwe Scholma, Thomas Mechielsen, and Daan Boltje for technical support with various experiments and keeping my experiments within the safe zone for both equipment and people. I would like to express my gratitude to Federica Galli for help with AFM experiments and I would like to offer my special thanks to Christiaan Pen and Peter van Veldhuizen for help with various experiments and, in particular, with building the setup for the gating experiments. I would also like to express my gratitude to the other members of the Fine Mechanical and Electronic Departments, especially to Ruud van Egmond, Ko Koning, and Raymond Koehler, for their assistance with technical work.

I appreciated working with Alexander van der Torren and Chunhai Yin on oxides at Leiden University. Technical assistance and warm encouragement by Stefano Voltan, Amrita Singh, and Kaveh Lahabi were invaluable. I had the good op-

portunity to work within the DESCO project, making it possible to discuss my research with many people and receive valuable feedback. I am grateful for all people participating in DESCO, especially Gertjan Koster, Andrea Caviglia, Mark Golden, George Arazi Kanoutas, and Sander Smink.
My thanks also go to Wilfred van der Geest for always having a bit of extra liquid helium when "it was really needed." I would like to say thank you to Daniëlle Duijn-ter Veer, Ellie van Rijsewijk, and Annette Bor, who helped me with bureaucratic procedures to allow me to concentrate on research.
I have greatly benefited from work with my former students Yorick Bleiji, Jessika Piñeiros Bastidas, Daniel Opdam. Special thanks go to Lucia Bossoni and Hadi Arjmandi-Tash for the opportunity to contribute to their research. I would further like to thank Johannes Jobst for sharing his knowledge on Linear Magnetoresistance. I would like to acknowledge Anne France Beker, Carlos Sabater, Irene Battisti, Thomas Ruytenberg, Remko Fermin, Aymen Ben Hamida, Junxiang Yao, Iacopo Bertelli, Kumar Prateek, Chris Smiet, Daniël Geelen, Aniket Thete, Flavio Mariani, Sander Blok, Tobias de Jong, Gesa Welker, Martin de Wit, Maarten Leeuwenhoek, Jaap Kautz, Tjerk Benschop, Koen Bastiaans, Sumit Tewari, and Sasha Vrbica for creating an amazing work environment.

Many of my colleagues have become my friends and have already been mentioned. However, still, I would like to mention people who cheered my PhD life: Pedro Salas, Pablo Castellanos Nash, Sayan Seal, Francesco Nattino, Kimberly Emig, James Pearson, Heather Andrews, Jorge Andres, Marta Artola, Davide Lionetti, Cláudio Rebelo de Sá, Paula Andrea, Matthieu Arierep, Maren, Vicente Atal, Sayan Seal, Emanuele Di Gloria, Manuela Mandrone, Maren, Santiago Torres, Javiera Paz Figueroa, Davide Stefani, Elena Yakunina, Marina Makarova, Aleksei Kondratov, Afanasiy Belyushin, Alexander Gomzikov, Evgeniy Shlychkin, Viacheslav Ostroukh, Nikolay Gnezdilov.

I would like to express my love and gratitude to Tahani. In the end, I would like to thank my family, especially my aunt and uncle, Larissa Ivanova and Leonid Ivanov, my cousins Eugenia and Elizaveta, my grandparents, Galina Novikova and Anatoly Novikov, my brother Artem, and my parents, Oleg and Natalia, who always support me in my path.